Investigation of Wake Redirection Techniques for Wind Farms

Kayla Surujhlal

(Student number: 2143969)

School of Mechanical, Industrial and Aeronautical Engineering

University of the Witwatersrand

Johannesburg, South Africa.

Supervisor: Prof. Wei Hua Ho

Co-supervisor: Mr. Ayodimeji Biobaku

A Dissertation submitted to the Faculty of Engineering and the Built Environment, University of the Witwatersrand, in fulfilment of the requirements for the degree of Master of Science in Engineering.

16/05/2025

DECLARATION

I declare that this dissertation is my own, unaided work, except where otherwise acknowledged. It is being submitted for the degree of Master of Science in Mechanical Engineering at the University of the Witwatersrand, Johannesburg. It has not been submitted before for any degree or examination at any other university.

Signed May 16, 2025:

Kayla Surujhlal

PUBLICATIONS ARISING FROM THIS RESEARCH

- K. Surujhlal, W.H. Ho, et. al, "Some observations on wake redirection techniques of tandem wind turbines", *Physics of Fluids*, 37, 2025, doi: 10.1063/5.0255621.
- K. Surujhlal, W.H. Ho, et. al, "Wake Redirection Prediction for Wind Farms", *South African Conference on Computational and Applied Mechanics*, Johannesburg, South Africa, 2025.
- K. Surujhlal, W.H. Ho, et. al, "Wake Redirection Techniques for Wind Farms", *South African Conference on Computational and Applied Mechanics*, Stellenbosch, South Africa, 2024.
- K. Surujhlal, A. Biobaku, "Surrogate modelling of wakes in wind farms in wake steering conditions", *Proceedings of the Annual National Research Data Workshop*, 2023, (pp. 31).

ABSTRACT

A world-wide increase in wind energy has seen an increase in the need for optimisation of wind farms. In a wind farm, an upstream turbine has several negative effects on the downstream turbine. The upstream turbine extracts a lot of the energy from the freestream, leaving little energy remaining in the wake to be extracted by the downstream turbine. There is also a significantly higher turbulence intensity in the wake leading to uneven loads being exerted. This all results in reduced power outputs of the wind farm as a whole. Wake redirection techniques, and specifically yaw misalignment, could reduce these negative effects and improve the overall power output of a wind farm.

The first aim of this study is to investigate the ability of a surrogate model to predict the flow field when the upstream turbine is at different yaw angles. This could assist with real-time wake analysis and optimisation of a wind farm, without the need for running high-fidelity simulations to predict the wake when the yaw angle of the turbine is changed. The second aim is to investigate the physical effect of the upstream turbine yaw on the wake, as well as the interaction between the wake and the downstream turbine.

A surrogate model is a combination of a Reduced Order Model (ROM) and a Machine Learning (ML) algorithm. A ROM was created using an existing, open-source dataset that conducted Large Eddy Simulations (LES) on a two-turbine array using the Simulator for Wind Farm Applications (SOWFA) software. The Dynamic Mode Decomposition (DMD) modes generated during this process were grouped according to the physical property of the wake that they represent. These modes were used to train the ML model to predict the development of individual modes at different yaw angles, which were then reconstructed in groups or combinations of groups to predict the entire flow field at the different yaw angles. It was found that the mode group related to the mean flow is essential to reconstruction and it alone results in the most accurate reconstructions with an average error of 7% and a reduction in computational resources by a factor of approximately 300 compared to LES.

Smoke visualisation, hot-wire measurements and force tests were conducted to further investigate the physical properties of the wake. A difference of 8.1% was recorded between the experimentally measured maximum angle of deflection and the maximum generated from the surrogate model. It was found that the larger the yaw angle of the upstream turbine, the greater the wake deflection. This relationship is hypothesised to be linear until the tested yaw angle of 45°, however it is expected to plateau after it reaches its stall condition. As yaw increases, both the force in the horizontal direction (Fy) and the side toppling moment (Mx) decrease linearly with the yaw angle, suggesting that a larger yaw angle also helps reduce the structural loads on the downstream turbine.

ACKNOWLEDGEMENTS

I would like to thank Professor Wei Hua Ho and Mr. Ayodimeji Biobaku for all the guidance and support they have given me during my Masters. I truly appreciate the time they made to have weekly meetings and for their important advice. I gratefully acknowledge Mr. Ayodimeji Biobaku for his valuable assistance with the modelling.

I would especially like to thank Prof. Ho for always pointing me in the right direction and for his mentorship throughout my Masters – both with research and in the creation of opportunities. This will always be greatly valued.

Many thanks to Mr Shaun Riekert and all the technicians from the Wits Workshop for their expertise in the manufacturing of the different components used in the experimental measurements and for always getting it done so timeously. Thank you also to Mr. Andrew Heydenrych for making it easy to get all the equipment used for testing and for troubleshooting of the 3D printers at any time.

My gratitude is also extended to Prof. KB Lua from the National Yang Ming Chiao Tung University in Taiwan for allowing me to use his design of the force sensor.

I would also like to thank Dr Nick Zang and Dr. Xiao Liu from the University of Bristol for their assistance in the experimental setup and operation of the wind tunnel at the university. I would also like to thank Mr Ricky Billingham and the technicians from the University of Bristol for their kind hospitality in the lab and their time given to manufacture the additional components needed during testing.

I will always be grateful for the constant support from my family and their confidence in me.

TABLE OF CONTENTS

DECLARATION i

PUBLICATIONS ARISING FROM THIS RESEARCH ii

ABSTRACT iii

ACKNOWLEDGEMENTS iv

1 INTRODUCTION 1

1.1 Background 1

1.2 Literature Review 3

1.2.1 Redirection technique, loads exerted and wake characteristics 3

1.2.2 Modelling 7

1.3 Purpose of the Study 8

1.4 Identified Gaps 8

1.5 Scope 8

1.6 Assumptions and limitations 8

2 RESEARCH QUESTION, AIMS AND OBJECTIVES 9

2.1 Research Questions 9

2.2 Research Aims 9

2.3 Research Objectives 9

3 Description of the dataset 10

4 Methods 12

4.1 Experimental Methods 12

4.1.1 Wind Tunnel at the University of the Witwatersrand 12

4.1.2 Wind Tunnel at the University of Bristol 13

4.1.3 Wind Turbine Model 13

4.1.4 Balancing Rig 19

4.1.5 Yaw Control of the Wind Turbine Model 20

4.1.6 General Setup used for Experimental Testing 23

4.1.7 Smoke Visualisation 24

4.1.8 Hot-Wire Anemometer 31

4.1.9 Force Tests 38
4.2 Surrogate Model Methods 42
4.2.1. Reduced Order Model Method 42
4.2.2 Modal Information 47
4.2.3 Identification and Grouping of Modes 48
4.2.4 Machine Learning Algorithms for Prediction 56
5 RESULTS 65
5.1 Comparison between the LES Model and the Hot-Wire Anemometer Measurements 65
5.2 Smoke Visualisation Measurements 70
5.3 Hot-Wire Measurements 76
5.4 Combination of Experimental Results 80
5.5 Validation of the Machine Learning Model by Comparison to the Original LES data 86
5.6 LES-Trained Machine Learning Predictions 88
5.7 DMD-Trained Model 92
5.8 DMD-Trained (Reconstruct Before) 101
6 CONCLUSION 105
7 RECCOMENDATIONS 106
8 REFERENCES 107
9 APPENDICES 115
9.1 Data Sheets 115
9.1.1 DC motor 115
9.1.3 Smoke Fluid 116
9.1.3 Strain Gauges 117
9.2 CAD Drawings of Manufactured Components 118
9.2.1 Rotor 118
9.2.2 Tower 119
9.2.3 Nacelle 121
9.2.4 Hub 122
9.2.5 Camera Mount 123

TABLE OF FIGURES

Figure 1. Main components of a horizontal axis wind turbine (left) and an example of aligned wind farm arrangement (right) 1
Figure 2. Illustration of yaw misalignment 2
Figure 3. Impingement of the wake of an upstream yawed turbine on a downstream yawed turbine 4
Figure 4. Wake characteristics of a wind turbine 5
Figure 5. Kidney-Shaped deflection of the wake of a yawed turbine 6
Figure 6. Yaw angle of the upstream and downstream turbines at different timesteps of the identification dataset 11
Figure 7. Wind tunnel at the University of the Witwatersrand 12
Figure 8. Wind tunnel at the University of Bristol 13
Figure 9. Surface finish of the test blade after 3D printing (a) and after it has been sanded down (b). 16
Figure 10. Test blade that was smoothed with ethyl acetate 16
Figure 11. Test blade that was coated with two layers of clear spray-paint 17
Figure 12. Test blade that was coated with epoxy (left) and then sanded down (right) 17
Figure 13. Final surface finish of the test blade 18
Figure 14. Nacelle, hub, motor and rotor connections of the wind turbine model 19
Figure 15. Balancing rig 20
Figure 16. Full wind turbine model 23
Figure 17. Experimental setup in the wind tunnel 23
Figure 18. Wind turbine array in the wind tunnel 24
Figure 19. Smoke generator 25
Figure 20. Comparison of the different cameras 27
Figure 21. Design of the camera mount (top) and the 3D-printed mount inside the wind tunnel (bottom) 28
Figure 22. Screenshot of smoke visualisation of the wake from a video recording 30
Figure 23. Edited image of the smoke visualisation, boundaries highlighted and the middle of wake identified 30
Figure 24. Centre of wake deflection quantified from the smoke visualisation image 30
Figure 25. Traverse system used for the hot-wire anemometer tests 31
Figure 26. Setup of the hot-wire probe inside the wind tunnel 32
Figure 27. Traversing directions of the hot-wire probe 32
Figure 28. Hot-wire probe calibrator 33
Figure 29. Example of hot-wire probe calibration curves and coefficients 34
Figure 30. Hot-wire calibration measurement locations from the front view of the wind tunnel 34
Figure 31. Hot-wire test locations from the front view (top) and the top view (bottom) 36

Figure 32. Setup for the hot-wire measurements in the wind tunnel ... 37
Figure 33. Positive directions of the forces and moments exerted on the downstream turbine ... 38
Figure 34. Force sensor design (top) and assembled (bottom) ... 39
Figure 35. Calibration setup of the strain gauges ... 40
Figure 36. Calibration curves for the eight strain gauge pairs ... 41
Figure 37. Post-processing curve of the force data ... 42
Figure 38. Processing steps of the LES dataset ... 43
Figure 39. VAF for 100 DMD modes for the identification and validation datasets for the upstream turbine (top) and the downstream turbine (bottom) ... 44
Figure 40. Locations of the different mode pairs on the complex plane ... 48
Figure 41. Top view and side view of one pair of modes from each group ... 49
Figure 42. Top view of four pairs of modes from Group 4 ... 50
Figure 43. Spread of different mode groups across the different ratios of frequency to energy ... 51
Figure 44. Example of a KNN algorithm ... 51
Figure 45. Confusion matrix for the KNN algorithm test ... 52
Figure 46. General structure of a neural network ... 53
Figure 47. Training input for the Deep Neural Network ... 53
Figure 48. Deep Neural Network training curve ... 53
Figure 49. Reconstructions of the flow field using individual mode groups ... 54
Figure 50. Comparison between the different groups and combination of groups used for reconstructions of the flow field ... 56
Figure 51. Example of the training input of the Time-Series Forecasting method ... 58
Figure 52. Comparison between two different instances of the flow field at 23.2° ... 59
Figure 53. Example of the training input of the Neural Network Fitting method ... 60
Figure 54. NNF model of LES-trained predictions using default settings ... 61
Figure 55. Network diagram for the Neural Network Fitting model ... 61
Figure 56. Preliminary predictions of the flow field with optimized NNF model settings ... 64
Figure 57. Top view of the velocity profile of the wake at different distances downstream of a propeller ... 66
Figure 58. Velocity curves representing the different components of the wake ... 67
Figure 59. Front view of the wake at x = 2.5D and x = 4D at 10° and 30° ... 68
Figure 60. Average deflection of the centre of the wake at different yaw angles of the upstream turbine ... 70
Figure 61. Collation of experimental results from previous studies measuring the deflection of the wake at x = 5D ... 71

Figure 62. Top view of the wake deflections as observed with the smoke measurements at different yaw angles of the upstream turbine 72
Figure 63. Front view of the wake deflections as observed with the smoke measurements at different yaw angles of the upstream turbine 73
Figure 64. Angle of deflection of the centreline of the wake at different yaw angles of the upstream turbine 74
Figure 65. Kidney-shaped deflection of the wake observed with the smoke visualisation at large yaw angles 75
Figure 66. Wake meandering in the spanwise direction – observed with smoke visualisation 75
Figure 67. Deflection of the wake at non-zero yaw angles – observed with smoke visualisation 75
Figure 68. Hot-wire measurements at x = 2.5D at different y-positions, comparing different yaw angles of the upstream turbine 77
Figure 69. Hot-wire measurements at x = 2.5D at different y-positions, comparing different yaw angles of the downstream turbine 78
Figure 70. Hot-wire measurements at x = 4D at different y-positions, comparing different yaw angles of the upstream turbine 79
Figure 71. Conventional directions used for force and moment measurements 81
Figure 72. Graph of Fy versus the yaw angle of the upstream turbine 81
Figure 73. Illustration of the different strengths of the wake and the impingement of the wake on the tower at the measurement location 82
Figure 74. Illustration of the change in the magnitude of Fy on the tower from a yaw angle of 0° (top) to 30° (bottom) 83
Figure 75. Graph of Mx versus the yaw angle of the upstream turbine 83
Figure 76. Moment arm of My at different yaw angles 84
Figure 77. Position of maximum velocity at different yaw angles 84
Figure 78. Graph of Mz versus the yaw angle of the upstream turbine 85
Figure 79. Top view prediction of the flow field at 10° and comparison to the original LES 87
Figure 80. Top view prediction of the flow field at 30° and comparison to the original LES 87
Figure 81. LES-trained model predictions at multiple yaw angles 89
Figure 82. Deflection of the wake at x = 5D (Using Velocity Matrix) 90
Figure 83. An example of pixels with the same grayscale intensity values with different RGB values 90
Figure 84. Threshold RGB value and the corresponding colour visualisation within the flow field 91
Figure 85. RGB limits of the threshold and their corresponding colour visualisations 91
Figure 86. Deflection of the wake from the centreline at a yaw angle of 15° 92
Figure 87. Illustration of the division of the LES dataset and grouping of the modes 93

Figure 88. A sample of four modes from Group 3 at 30° 96
Figure 89. ML output predictions when trained with all the modes of Group 4.................................. 97
Figure 90. Average error of the reconstructions using different mode group combinations 99
Figure 91. Reconstruction of the flow field using only Group 1 100
Figure 92. Comparison between the DMD-Trained model and the LES-Trained model at a sample of yaw angles.. 100
Figure 93. DMD-trained (reconstruct before) model predictions at different yaw angles.................. 102
Figure 94. Comparison between the DMD-trained (reconstruct before) model predictions and the LES-trained model predictions 103
Figure 95. Comparison of the angles of deflection between the smoke measurements and all three ML models 104

LIST OF TABLES

Table 1. Dimensions of the Components of the Wind Turbine Model ……………………………………… 15

Table 2. Evaluation of Different Design Options for Yaw Control ………………………………………… 21

Table 3. Comparison of Different Camera Options …………………………………………………….. 26

Table 4. Mode information of the first 6 modes ……………………………………………………… 47

Table 5. List of test cases and their corresponding groups or combinations of groups ………………..55

Table 6. Average error for different number of hidden layers used …………………………………63

Table 7. Average error for different training algorithms ……………………………………………..63

Table 8. Tracking of the wake from LES and Hot-Wire ……………………………………………..69

Table 9. Summary of the LES training data ……………………………………………………………88

Table 10. Summary of the physical property that each group is linked to ……………………………93

Table 11. Mode groupings at a yaw angle of 10° ……………………………………………………….94

Table 12. Mode groupings at a yaw angle of 30° ……………………………………………………….95

Table 13. Summary of the DMD training data …………………………………………………….....96

Table 14. Ranking of the modes within Group 2a and Group 2b ………………………………….....98

Table 15. Summary of the DMD training data for a single mode ……………………………………98

Table 16. Summary of the DMD training data (reconstruct before) …………………………………101

Table 17. Comparisons of Angles of Deflection for Different Methods ……………………………103

1 INTRODUCTION

1.1 Background

As the world aims to produce more energy from renewable sources, wind energy production continues to grow rapidly [1]. Wind turbines are used to harness the energy of the wind and use this energy to generate electrical power that can be supplied to power stations. There are two main types of wind turbines – vertical axis wind turbines (VAWTs) and horizontal axis wind turbines (HAWTs). With VAWTs, the axis of rotation is perpendicular to the ground, in the vertical direction [2]. Although they require less maintenance and have longer lifespans, VAWTs are not as scalable as HAWTs [3]. This means that they are more suited for smaller applications such as residential use and are not suitable for large-scale wind farms [3]. HAWTs are scalable, they can operate at higher wind speeds and have higher efficiencies [4]. This makes them more suitable for wind farm applications and therefore will be the focus of this study. When the wind flows over the rotor blades of the wind turbine, it exerts an aerodynamic force on the blades. This causes the air pressure on one side of the blade to decrease. The difference in pressure gradients between the two sides of the blade creates a lift and drag force on the blade [5]. The lift force is more dominant and this causes the rotor blade to rotate. The rotor is connected to a generator and as the rotor spins, electricity is generated according to Faraday's law [5]. The main components of a wind turbine are shown in Figure 1.

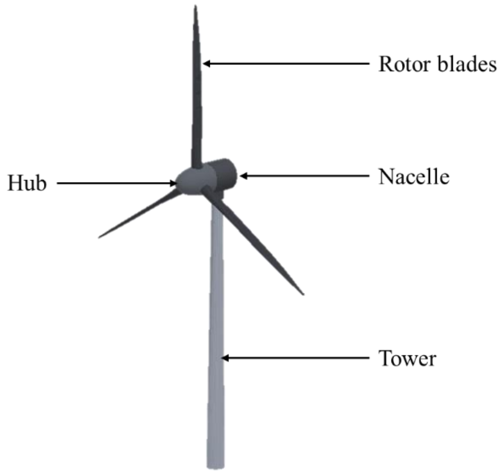

Figure 1. Main components of a horizontal axis wind turbine (left) and an example of aligned wind farm arrangement (right) [6]

To harness the full potential of the wind energy in a certain location and generate a large-scale amount of power, wind farms are set up. Wind farms are an array of wind turbines that are connected to each other via underground cables from where the electricity generated is then channelled into the electricity grid [7]. Most large wind farms have an aligned arrangement, such as the North Hoyle wind farm, the wind farm in Alberta, the London Array wind farm and the Horns Rev wind farm [8], [9], [10], [11]. Smaller wind farms such as the Wesley Ciskei wind farm [12] and the Oregon wind farm [13] do not have this arrangement because they have limited space and a fewer number of turbines which do not permit a completely aligned arrangement. Since the turbines are usually aligned behind one another, the wake of an upstream turbine has a significant effect on the performance of a downstream turbine.

The wake of an upstream turbine can have the following negative effects [14]:

1. After an upstream turbine extracts energy out of the wind, it leaves very little energy remaining in the wake which impinges on the downstream turbine. If a downstream turbine is completely in the wake of the upstream turbine, less energy can be extracted by the downstream turbine – leading to a lower power output by this turbine.
2. There is a significantly higher turbulence intensity of the air in the wake. This causes uneven loading on the downstream turbine which increases fatigue loads and leads to a reduced lifetime and generally more required maintenance.
3. Downstream turbines operating the wake of upstream turbines also produce more noise emission due to structural vibrations, which is a major social factor that often limits the establishment of wind farms.

Therefore, redirecting the wake of the upstream turbine away from the downstream turbine or redirecting the downstream turbine away from the upstream turbine's wake could avoid these negative effects and possibly improve the efficiency of the wind farm as a whole. The focus of this study is on the former.

There exist two main wake redirection techniques – tilt misalignment and yaw misalignment. Tilt misalignment is the rotation of the wind turbine rotor to face either upwards or downwards. Yaw misalignment is the rotation of the wind turbine rotor to the left or right of the freestream. Both of these techniques have been investigated. Both "steer" the wake away from the downstream turbine and there were contradicting results about which technique results in higher power outputs. Yaw misalignment forms the focus of this study because most installed turbines already have the ability to yaw but not tilt and it is also potentially simpler to implement. This is further motivated in section 1.2.1. Figure 2 is an illustration of yaw misalignment.

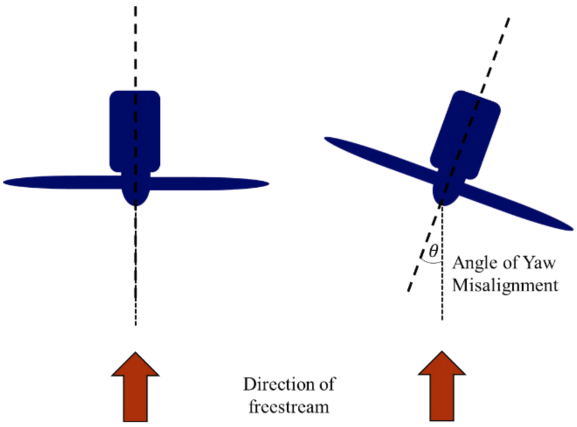

Figure 2. Illustration of yaw misalignment [15]

1.2 Literature Review

This section presents details and results from previous studies that investigated yaw misalignment. Specifically, reviews will be done on the comparison to tilt misalignment followed by the gains in power production, aerodynamic loadings, and wake characteristics.

1.2.1 Redirection technique, loads exerted and wake characteristics

Yaw versus Tilt Misalignment

Based on a comparison of previous yaw and tilt studies, it is noted that the total maximum percentage gain of power output for yaw is higher than that of tilt. A study concluded that a maximum power gain of 21.6% was achievable for a yaw angle of 30° [16] whereas another study concluded that a maximum power gain of 15% was achievable for a tilt angle of 30° downwards [17]. The percentage power gain refers to the increase in power output generated when an upstream turbine is yawed compared to when both turbines are not yawed. Analysis of different previous studies has shown that maximum percentage power gains for yaw misalignment range from 11% to 21.6% [17], [18], [19] and from 6% to 15% for tilt misalignment [20], [21], [22].

However, there is a contradiction in the research as to whether tilt or yaw misalignment leads to a greater percentage gain in power output because one study that tested both tilt and yaw misalignment found that tilt misalignment results in a 2% greater gain in power output [21]. However, the gain of 14.5% measured is still less than what was observed in a previous study as shown above [16].

Excluding power generation, previous studies show that tilt results in large uneven structural loads being exerted on the turbine tower and blades [18] and have an unacceptably high risk of tower strikes as the tip of the rotor is moved closer to the tower [20]. Also, most current turbines do not yet have the ability to tilt [22], whereas they do have the ability to yaw. Hence yaw misalignment is potentially simpler to implement and is chosen as the focus of this study.

Location in a wind farm

It has been noted, from a previous simulation study on the effect of yaw in the front row versus a deep row in a wind farm, that the net power gain is approximately three times greater for a yawed front row turbine compared to a yawed deep row turbine [23]. As the air moves through each consecutive turbine row, more energy is extracted and there is less energy in the air to be extracted by the following turbines. Therefore, in the deeper rows, the advantages of yaw misalignment are much smaller. Therefore, this study will focus on the first two rows of a wind farm arrangement with yaw being implemented in the first row.

Yaw Angles

In order to achieve these power gains discussed above, it has been found from previous studies that maximum power gains occur when the upstream turbine is at a yaw angle of 30° [16], [24], [25], [26]. Previous studies have also concluded that the larger the yaw angle of an upstream turbine, the greater the power output [16], [27]. This is because the larger the yaw angle of the upstream turbine, the further the wake is deflected away from the downstream turbine, thus the greater the entrainment of clean air with greater energy leading to larger power outputs. Based on the previous studies mentioned that investigated a yaw angle of 30° and found that this is where the greatest power gains are observed, this study will include 30° as part of the range of yaw angles tested.

Loads

When an upstream turbine is at a non-zero yaw angle, the downstream turbine is exposed to a strongly sheared inflow [28] because the inflow is partially from the wake and partially from clean, undisturbed air – both of which have different wind speeds. This causes large yaw moments and thus increased loads which is detrimental to the downstream wind turbine. However, it is expected that also controlling the yaw angle of the downstream turbine to be angled in the opposite direction can counteract the loads exerted by the sheared inflow and reduce the yaw moment. However, the loads on a downstream turbine have not been fully investigated experimentally and quantified. Figure 3 shows how a yawed upstream turbine redirects the wake impinging on a downstream turbine. It is speculated that maximising the yaw angle of the upstream turbine (30°) to direct the wake away from the downstream turbine and maximising the angle that the downstream turbine faces away from the impinging wake (-15° to -30°) would result in the best strategy to reduce sheared inflow loads and yaw moments. This would also increase the flow of clean, undisturbed air onto the rotor-swept area of the downstream turbine and thus potentially increase the power output. This gap in knowledge and the strong possibility of an effect of yaw misalignment on the loads experienced is the motivation for the investigation of the loads experienced by the downstream turbine.

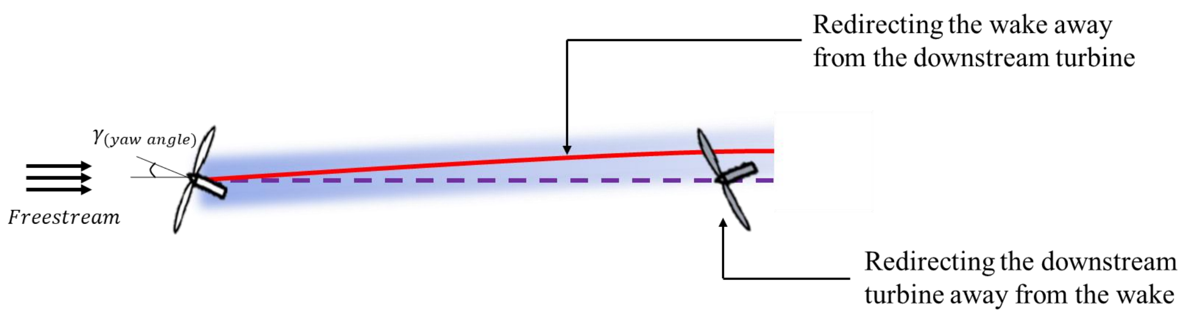

Figure 3. Impingement of the wake of an upstream yawed turbine on a downstream yawed turbine (adapted from Howland et. al [29])

Wake Characteristics

One simulation study showed that partial impingement of the upstream wake on the downstream turbine resulted in reduced loads and slightly increased power gains of 5% [28]. Although two turbines were investigated in this study with both turbines at non-zero yaw angles, only the power output was measured. The behaviour and characteristics of the wake were not analysed and therefore no evidence-based explanation could be given for the power increase and reduced loads.

There is a need to analyse the wake characteristics and behaviour to determine how effective certain combinations of yaw angles are and understand why they are effective or ineffective. There are different characteristics that can be observed in the wake of a wind turbine that affect the interaction of the wake with the downstream turbine. These include tip vortices, hub vortices and the shape and deflection of the wake.

Tip vortices

Tip vortices originate from the tip of the blades and develop into tightly wound helical vortices, as seen in Figure 4. These vortices originate due to the difference in pressure between the two surfaces of the aerofoil [1]. Tip vortices can reduce the flow entrainment in the near wake by separating this region from the outer flow [1]. Energy is entrained from the clean air above the wind turbine to replenish the wake and thus allow for greater power output from the turbine further downstream [30]. Therefore, a reduction in entrainment is undesirable and a faster breakdown of the vortices is beneficial. It is expected that when the upstream turbine is at a non-zero yaw angle, the tip vortices will break down faster and lead to increased flow entrainment and thus greater power output.

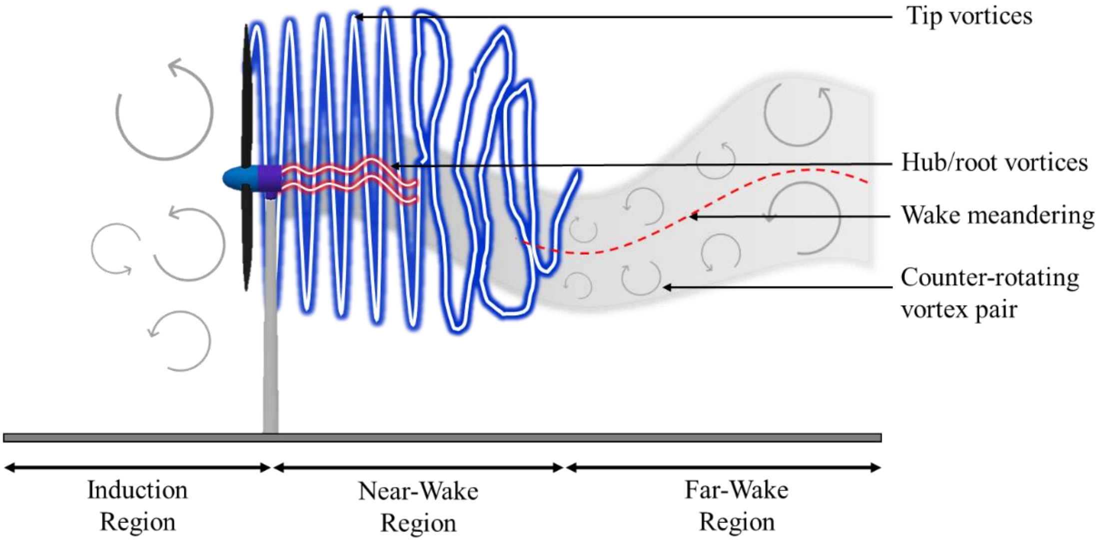

Figure 4. Wake characteristics of a wind turbine (adapted from Porté-Agel et. al [1])

Hub vortices

Hub (or root vortices) are vortical structures that originate from the hub and are located at the centre of the near-wake region and are elongated in the streamwise direction [1], as seen in Figure 4. Studies show that the hub vortex is characterised by a single-helix counter-winding instability which interacts with the tip vortices [1]. This helix vortex structure has been shown to induce periodic motions in the central part of the near-wake [1]. These vortices could possibly be another source that reduces the flow entrainment, similar to the tip vortices, except these occur periodically. Since these vortices remain fairly close to the hub, it is predicted that these vortices would not have a significant effect on the flow entrainment. However, it is still expected that having the upstream turbine at a maximum yaw angle away from the downstream turbine and minimising the wake impingement on the downstream turbine will increase flow entrainment and thus the power output.

Kidney-Shaped Deflection

Studies have shown that during yaw misalignment, the circular shape of the wake is deformed into a curled kidney shape [24], [25], [27], as shown in Figure 5. This unique shape of the wake is attributed to the formation of a counter-rotating vortex pair that forms when the tip vortices break down [24], as seen in Figure 4. Its interaction between the ground and the rotation of the wake [31] causes high lateral velocities that deflect the wake sideways [24]. The results of one experimental study showed that there was a skewness angle of ±3.6° for yaw angles of ±30° for a rotor diameter of 0.580 m [25]. When both turbines are yawed, it is expected that the wake will have a larger deflection because it is expected that the tip vortices will break down sooner. This would result in the counter-rotating vortex pair to form sooner. More energy will be entrained from the air causing a higher lateral velocity and thus a larger lateral deflection. Information about these wake characteristics will inform the methodology to assist in capturing the behaviour of these characteristics.

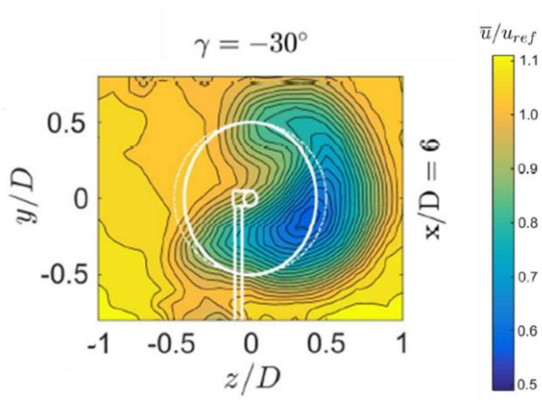

Figure 5. Kidney-Shaped deflection of the wake of a yawed turbine (taken directly from Bartl et.al) [23]

1.2.2 Modelling

A Reduced Order Model (ROM) is a simplification of a complex model. It is most commonly created from high-fidelity datasets and it is used to capture and analyse the dominant dynamic behaviour of the original complex model while using less computational resources [32]. This can lead to shorter design cycles as models can be run in a shorter time without sacrificing significant accuracy [33]. ROMs have been found to be very effective in modelling wind turbine dynamics. Various reduced order models exist, such as proper orthogonal decomposition (POD), dynamic mode decomposition (DMD) and input-output dynamic mode decomposition (IODMD) [34]. A study conducted by Cassamo used an extended IODMD method and showed that a ROM was able to reproduce the downstream turbine generator power with a 74% fit and reconstruct upstream turbine's wake with a normalised root mean square error (NRMSE) of 3.56% [34]. However, this study where only the upstream turbine is yawed, primarily focuses on the power output and not the wake characteristics. This further indicates a gap in knowledge which informs the decision to investigate two aligned, yawed turbines and the wake characteristics associated with this configuration.

Combining a ROM with a machine learning (ML) algorithm is referred to as a surrogate model. Surrogate models have recently been used to improve the predictive capability and accuracy of ROMs. Once the ROM is created, a ML algorithm can be used to predict certain quantities of the flow field dynamics given certain input parameters [35]. Previous studies have shown that surrogate modelling is able to accurately predict the wake of a turbine, the power output, velocity distributions and turbulence intensities [36], [37], [38]. These studies all show that surrogate models are capable of producing more accurate data and a more detailed flow field compared to traditional analytical wake methods. Traditional methods are usually less detailed because they do not consider effects such as turbulence as this requires extensive computational resources and greatly increases the run-time of simulations. However, surrogate models reduce the complexity and required computational resources by capturing only the necessary dynamics of a system which allows for a more detailed flow field. Previous research also shows that predictions can be made for both the near-wake and far-wake, for both streamwise and spanwise velocity components, and for different inflow conditions [37]. This indicates the viability of the surrogate model method and gives confidence to its applicability to the current scenario.

There are different ML algorithms that can be used for wind turbine wake prediction. Different neural network types are most commonly used, such as artificial neural networks (ANNs) [36], [39] and variations of convolutional neural networks (CNNs) [37], [38]. Other algorithms such as long short-term memory (LSTM) are also used to predict the wake using video input of the wake behaviour [38]. These algorithms are discussed further in section 4.2.4. Neural networks are most commonly created using TensorFlow and the other algorithms are usually created using Python [39].

1.3 Purpose of the Study

The purpose of this study is to understand the effect that two aligned turbines at non-zero yaw angles have on the wake characteristics of the upstream turbine and the loads exerted on the downstream turbine. The purpose of this study is also to investigate the ability of a surrogate model to predict the wake of an upstream turbine that is at a non-zero yaw angle. The experimental data collected will also be used for insight into the wake and validation of the surrogate model predictions.

1.4 Identified Gaps

Currently no study has been conducted on the wake characteristics and loads exerted in a two-turbine aligned array where both turbines are at non-zero yaw angles. Although there are studies which investigated scenarios where only one turbine is yawed, there was no elucidation of the measured loads. As discussed above in section 1.2.1, no evidence-based reason could be given for the power increases observed in previous studies and this is why a better understanding of the loads exerted and wake characteristics is required. Currently no study has been conducted on using a surrogate model to predict the wake of a turbine that is at a non-zero yaw angle although this could assist with real-time wake analysis and optimization at a wind farm.

1.5 Scope

1. This study will be confined to the application of wind farms where the turbines are aligned (one behind the other in rows and columns) because, as mentioned above, most wind farms have this arrangement.
2. This study will also only be analysing the first and second row of turbines in a wind farm arrangement. This means that a freestream will enter the upstream turbine (first row) and the wake of this turbine will interact with the downstream turbine (second row). It is predicted that this is where the redirection technique will be most effective.

1.6 Assumptions and limitations

There are two main assumptions applied to this study. Firstly, the wake of a turbine only has a significant effect on the immediate downstream turbine. This assumption stems from the distance between wind turbine installations [33]. This limits the applicability of the results to wind farms with the more common aligned arrangement. The second assumption refers to the accuracy of the dataset. The dataset is from an LES CFD simulation. This work has been published and is assumed to be sufficiently accurate for the purpose of this study.

2 RESEARCH QUESTION, AIMS AND OBJECTIVES

2.1 Research Questions

There are two research questions that this project aims to address:

1. How does wake redirection affect the performance of an individual wind turbine and the overall performance of multiple wind turbines in a wind farm?
2. How effective is a surrogate model in predicting the wake of a two-turbine array when the upstream turbine is at non-zero yaw angles?

2.2 Research Aims

To answer the two research questions, the following specific research aims need to be addressed:

1. How different combinations of yaw angles of upstream and downstream turbines affect the wake characteristics.
2. How different combinations of yaw angles of upstream and downstream turbine affect the loads exerted on the downstream turbine.
3. The effectiveness of a surrogate model in accurately predicting the wake of a yawed turbine.

Aims 1 and 2 answer the first research question and aim 3 answers the second question.

2.3 Research Objectives

To address each of these research aims, the following research objectives will need to be achieved:

1. To design, fabricate and test a model of two wind turbines at different yaw angles to gather force data, flow visualisation data and velocity field data that can be used to analyse additional wake characteristics and to validate the surrogate model. This is necessary to fulfil aims 1 and 2.
2. To successfully train and test a selected surrogate model that can accurately predict the wake of two yawed turbines. This is necessary to fulfil all three aims.

3 DESCRIPTION OF THE DATASET

The key requirement underpinning this work is the availability of an appropriate dataset of wind turbine wake measurements that will be used to create the surrogate model. The identified dataset is an open-source dataset containing LES of a two-turbine array and it was generated using SOWFA. The model contains an upstream turbine and a downstream turbine that are placed five diameters (5D) apart. The wind turbines that are modelled are horizontal axis, DTU 10MW wind turbines that each have three blades. This wind turbine has a hub height of 115 m, a hub diameter of 5.6 m, a blade diameter of 178 m and a rated tip-speed ratio of 7.5. Additional characteristics of the turbine modelled can be found in Bak et. al [40]. The model is set up such that there is a uniform inflow condition, with no boundary layer or ground effects.

The domain size of the original LES simulations is 1.71 km in the x-direction, 343 m in the y-direction and 300 m in the z-direction. The original data generated from the LES simulations consisted of approximately 6 million spatial points. However, to reduce the computational resources required, pre-processing was performed (by Cassamo) to take only every fourth point [41]. This resulted in a much smaller dataset of 96 600 spatial points, which is the dataset that was available online and therefore used in this research. The original data also recorded readings every 0.2 seconds, but after pre-processing, the dataset available for use only has readings every 2 seconds, resulting in a total of 1818 timesteps (909 timesteps in the identification dataset and 909 timesteps in the validation dataset). The upstream turbine is yawed between 10° and 30° periodically for a total of 33 minutes and 20 seconds, whereas the downstream turbine remains constant at 0°. An illustration of how the yaw angle of the upstream and downstream turbine change in the identification dataset of the LES data is shown in Figure 6. In both datasets, the upstream turbine cycles through intermediate angles between 10° and 30°, but only remains at each of these intermediate angles for two seconds. As can be seen in Figure 6, it remains at 10° and 30° for much longer in each period.

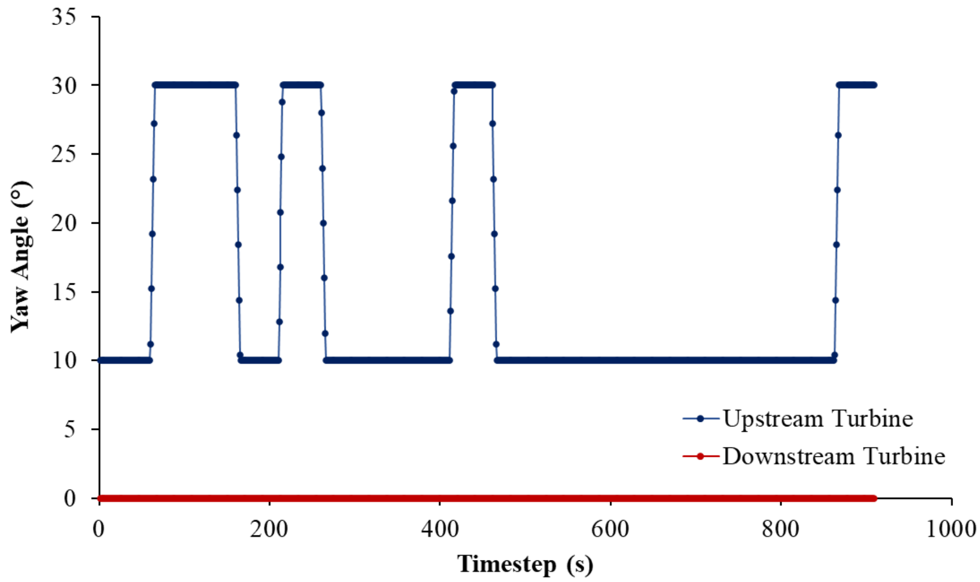

Figure 6. Yaw angle of the upstream and downstream turbines at different timesteps of the identification dataset

As mentioned above, the intended use for this dataset is to use it to create a surrogate model that could reduce the computational resources required to run analyses of the wake when certain parameters are changed (instead of re-running an entirely new LES simulation), as well as to understand the behaviour of the wake as the upstream turbine is yawed. However, since the dataset has limited data points at intermediate angles and has information of the fully developed flow field at only two yaw angles (10° and 30°), additional methods will be required to fully understand the wake behaviour and determine the effect of an upstream turbine yaw on a downstream turbine. Experimental research will be conducted with the intention to fill in the gaps in the present in the dataset and to extend understanding of the wake dynamics, forces and deflection due to the wake redirection technique.

4 METHODS

4.1 Experimental Methods

To fully understand the wake dynamics, three sets of experimental measurements were conducted, namely smoke visualisation tests, hot-wire anemometer tests and force tests. Smoke visualisation was used to physically view the wake development and quantitatively map out the deflection of the wake and was conducted at the University of the Witwatersrand (Wits). Hot-wire tests were conducted to quantitatively map out the wake development and were conducted at the University of Bristol (UoB). Force tests were conducted at Wits to analyse the effect of the wake on the downstream turbine. Each of these three sets of experiments were conducted in wind tunnels and the setup and methods for each is outlined below.

4.1.1 Wind Tunnel at the University of the Witwatersrand

The wind tunnel at the University of the Witwatersrand is a draw-down wind tunnel with a cross-section of 1.5 m x 1.5 m, a test-section that is 7.89 m long and it can achieve wind speeds of up to 16 m/s. It is the largest wind tunnel at the university and it allows for a bigger model which makes it easier to achieve the required scaling relationships.

Figure 7. Wind tunnel at the University of the Witwatersrand

4.1.2 Wind Tunnel at the University of Bristol

The wind tunnel at the University of Bristol is a boundary layer wind tunnel with a cross-section of 2 m (width) x 1 m (height), a test-section that is 18 m long and can achieve wind speeds up to 35 m/s.

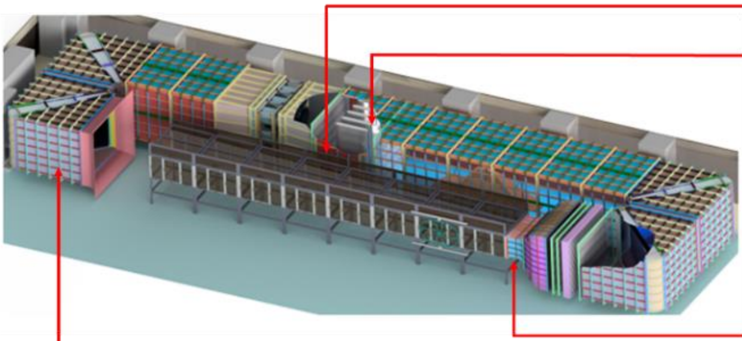

Figure 8. Wind tunnel at the University of Bristol

4.1.3 Wind Turbine Model

Scaling of the Wind Turbine Model

Two scaled models of the DTU 10 MW wind turbine were designed and fabricated for the experiments as it was the turbine modelled in the dataset. It is an upwind, horizontal axis wind turbine with three blades. The blades are FFA-W3-241 aerofoils. It has a rated tip speed of 90 m/s and the diameter of the rotor is 178.3 m [40]. Scaling of the turbine is required for wind tunnel testing. Although it would be ideal to achieve dynamic similarity through Reynolds number matching, this is usually not viable for wind turbine models because in order to scale down the Reynolds number the wind tunnel speed will need to be unrealistically high [14]. Previous studies have shown that in order to have a model that is able to rotate solely from the wind tunnel airspeed, in-depth blade and turbine design is required which is unique to the specific wind tunnel [42]. Also, rotating the model with only the wind speed does not mean that the wake dynamics will be similar to the full-scale wind turbine because there is a correlation between the achievable power coefficient, the tip-speed ratio and the ratios between the of coefficient of lift to coefficient of drag [42]. An iterative design and testing process is required to design a turbine model that can either match the power output or match the wake dynamics, not both. This was outside the scope of this research and since the primary use for the model is for integration with an LES simulation, the dynamics of the wake was of most importance to this study and the power output was not required. Therefore, the following scaling relations listed below were applied as recommended [14].

1. Maintain geometric similarity as far as possible
2. Maintain the same tip-speed ratios
3. Keep the number of blades and blade profile constant

To maintain geometric similarity and ensure the same tip-speed ratios are tested, a DC motor was used to rotate the blades. The datasheet for the specific motor used is given in Appendix 9.1.1. The following equations were used to establish a relationship between the scale of the wind turbine model, the tip-speed ratio, the required motor RPM and the blockage percentage.

For the different tip-speed ratios required, the required tip speed of the rotor can be calculated using the following equation:

$$V = \lambda \times U \tag{1}$$

where V is the tip speed of the rotor (m/s), λ is the tip-speed ratio and U is the freestream wind speed (m/s).

The motor RPM speed required is then calculated using the equation below:

$$RPM = \frac{60V}{2\pi r} \tag{2}$$

where r is the radius of the rotor blade (m).

The blockage ratio of the model can be calculated using the following equation:

$$R = \frac{A_{model}}{A_{wind\ tunnel}} \tag{3}$$

where R is the blockage ratio, A_{model} is the area of the model (m^2) and $A_{wind\ tunnel}$ is the cross-sectional area of the wind tunnel (m^2).

Blockage ratio defines what percentage of the wind tunnel cross-section the model blocks [43]. In this study, the wake behind the turbine is of particular interest and it is important to ensure that when the wake expands behind a turbine it is not affected by the wall conditions. Therefore, blockage effects need to be minimised. A maximum blockage ratio of 16% is required to avoid substantial blockage effects [44]. Previous experimental wind turbine wake studies were conducted at blockage ratios of 0.7% [27], 1.2% [18], 6.5% [16] and 12% [24], with no reported effects. Therefore, for the experiments in this study, the blockage ratio will be limited to a maximum of 16%.

To achieve geometric similarity, have an operating tip-speed ratio of 7.5, and be within a maximum blockage percentage of 16%, Equations 1, 2 and 3 were used to calculate the scale factors. A scale factor of 1:380 was used for all the components except for the nacelle. Using this scale results in a nacelle diameter that is much smaller than the physical size of a motor required and available. Therefore, the size of the nacelle needed to be increased to a scale of 1:242. A previous study that investigated the effect of the nacelle on the turbine wake concluded that the ratio of the nacelle to the diameter of the rotor is not significant and that a larger nacelle does not impact the flow significantly [45].

Table 1. Dimensions of the Components of the Wind Turbine Model

Component of the Model	**Dimension**	**Value (mm)**
Tower	Length	305.7
	Diameter at the floor	21.8
	Diameter at the nacelle	14.7
Rotor	Diameter	454.4
Nacelle	Diameter	40.0
	Length	38.4
Hub	Diameter	40.0

With these dimensions, the blockage ratio in the wind tunnel at Wits was 7.3% and at UoB it was 8.2%.

Wind Turbine Model Blades

Previous experimental studies mostly used 3D printed blades [14], [16], [20], [27], whereas one study used aluminium [24]. Although aluminium blades could possibly have been more robust, it would have required complex manufacturing methods and a much longer downtime if the blades got damaged. 3D printing allows for shorter manufacturing times of complex parts that do not require workshop time, and lighter blades require a lower torque allowing for a smaller motor that could fit inside the scaled nacelle. Given the small size of the model and the small amount of material required, 3D printing with Polylactic Acid (PLA) was chosen to be the most suitable method for the blades. The turbine was rotated at its maximum speed and at a wind speed much higher than the testing speed and no visible deflections of the 3D-printed blades were observed. The CAD drawing of the rotor is provided in Appendix 9.2.1.

To 3D print the rotor blades, the finest quality (0.12 mm) was used to get a thin a layer as possible with as smooth a finish as possible since the surface finish of the blades are very important to the aerodynamics of the blade and thus the wake it produces. PLA filament was used because it achieves a smoother surface finish compared to Acrylonitrile Butadiene Styrene (ABS) [46]. It is also less likely to warp when cooled [46], which is important since deformation of the blade is undesirable. PLA can also print sharper corners and finer details [46], which is important since the blades come to a point and have a very thin edge on one side. An attempt was made to print just the shell (with minimal internal supports) to match full-scale turbines, but given the small size and the complex shape, the supports inside were not sufficient and the print quality was not adequate. A 100% infill was used to increase the stability of the uniquely-shaped blades which would be very fragile otherwise. The rotor was printed as one piece to ensure accurate placement of the blades and to reduce the risk of a blade detaching from the rotor during operation.

Once the rotor blades were 3D printed, the finish on the blades was rough to the touch with the layers of filament creating a stepped effect due to the complex curvature of the blades, despite the finest quality being used. Figure 9(a) shows the surface finish of the blades directly after 3D-printing.

Therefore, post-processing of the blades was done to achieve the smoothest finish possible. Several different post-processing methods were tested to determine which method or combination of methods result in the smoothest finish of the rotor blades. These methods are outlined below.

<u>Sanding down of the blades with water paper</u>

This process involves sanding down every surface of the blade evenly, starting with a low grit water sandpaper and working upwards towards the highest grit. Water sandpaper was used to achieve as smooth a surface finish as possible on the blades. A test blade that was sanded down is shown in Figure 9(b).

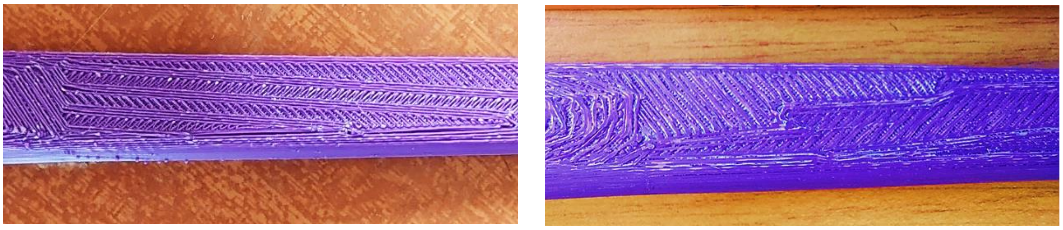

(a) (b)

Figure 9. Surface finish of the test blade after 3D printing (a) and after it has been sanded down (b)

<u>Using a solvent to dissolve and smooth the top layer of the blade</u>

The most commonly used solvent used to smooth 3D printed parts is acetone. However, since PLA is more resistant to acetone smoothing compared to other materials, a stronger solvent such as tetrahydrofuran, dichloromethane or chloroform could be used [47]. However, the use of these would have required additional safety requirements which was not practical. Therefore, ethyl acetate was used. A cloth was soaked in the solvent and then rubbed onto the blade to slowly dissolve the top layer of filament until a smoother surface was evident. It was difficult to get a uniform smoothness along the print and it did not work for rougher surfaces because using too much of the solvent caused the strands of filament to come apart, as seen in Figure 10.

Figure 10. Test blade that was smoothed with ethyl acetate

Coating the blade with spray paint

This method involves coating the blade evenly in spray paint and leaving it to drip-dry so that the spray paint does not dry thicker in certain places and thus lead to an unbalanced rotor. This method allows for an even coat to be applied, and for more coats to be applied as necessary. However, even after three coats of spray paint, the crevices did not get filled and therefore this method is not useful for smoothing rougher surfaces. A test blade that was coated with two layers of spray paint is shown in Figure 11.

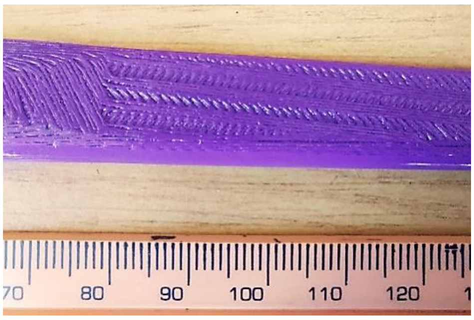

Figure 11. Test blade that was coated with two layers of clear spray-paint

Coating the blades with epoxy resin

For this method, the blade was first sanded down so that the epoxy could adhere well to the surface and it was then coated evenly in a two-part epoxy resin. A small amount of acetone was mixed into the two-part epoxy resin to thin the mixture. This allowed for a more even layer to be applied to the blade. Due to the high viscosity of the resin (even after the acetone was mixed into it), the resin added to the mass of the blade. It was also not as easy to apply the resin evenly compared to the spray paint and some bumps were left on the surface. However, the resin was able to fill in larger crevices and cover rougher areas. Additional post-processing such as sanding was required after this step. A test blade that was sanded down and coated with the epoxy resin (left) and the blade after it was sanded down, coated with epoxy and sanded down again (right) is shown in Figure 12.

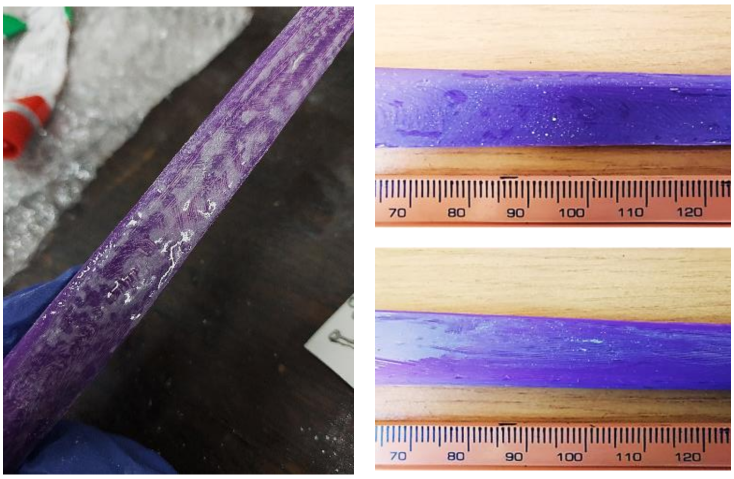

Figure 12. Test blade that was coated with epoxy (left) and then sanded down (right)

Vapor smoothing

Vapor smoothing is also a common method used for smoothing 3D prints. This is a technique that exposes the 3D print to a vaporized chemical, such as acetone or MEK, inside a smoothing chamber [48]. Inside the smoothing chamber the temperature, pressure and concentration of the solvent is managed such that the outer layer of the print is melted and partially dissolved, resulting in a smoother, glossier finish [48]. However, access to this technology was not possible.

Using a heat gun to melt the top layer of the blade

Since a heat gun is able to output a uniform layer of controlled heat, it was speculated that this could melt the top layer of the print, giving it a smoother finish. However, through testing it was discovered that the heat gun was too hot and uncontrolled for the blade due to its thin edges.

Final processing method used

After testing each of the methods available above, the following final method was used to give the best finish on the blades:

1. Sand the blade down with water paper. A maximum grit of 1200 was used.
2. Mix the epoxy resin with acetone and apply as evenly as possible onto the blade.
3. Sand down the blade coated with the set epoxy. Maximum grit of 1200 was used. This results in a very smooth finish with no rough areas.
4. Apply a thin layer of spray paint to the blade to give it an even smoother finish and provide a layer of protection against the smoke used for the smoke tests. The epoxy resin reacts to the smoke and causes it to start peeling if not protected against.

Figure 13 shows a test blade that has had the above post-processing methods applied to it to result in the best surface finish.

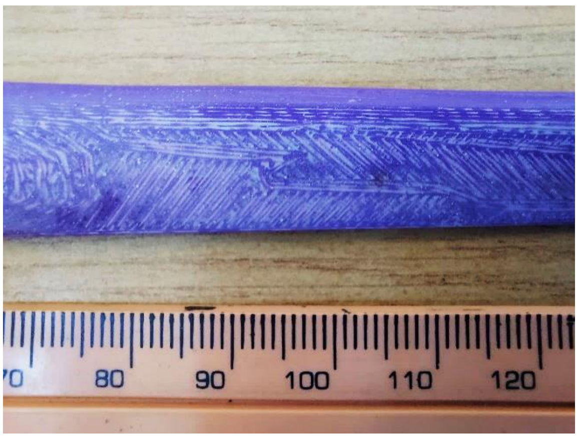

Figure 13. Final surface finish of the test blade

Wind Turbine Model Tower

Although a previous experimental study has been conducted on just the rotors of wind turbines [49], it has been shown that the tower has a large impact on the flow properties [50] and therefore the model in this study includes the tower. The tower needed to be strong enough to support the nacelle with the motor inside, as well as a moving rotor. It was also required to be hollow so that the cables connecting the motor to the power source and control could run through the tower and not on the outside which would affect the flow. It was decided to construct the tower with aluminium through the process of rolling so that it would provide the stability required. The CAD drawing of the tower and the sheet metal drawing used to roll the tower is given in Appendix 9.2.2.

Wind Turbine Model Nacelle and Hub

The nacelle and hub were 3D-printed due to their complex shape. The hub was not 3D-printed as one part with the rotor because the rotor needed to be fastened onto the motor shaft securely with a hub screw to prevent it flying off, as shown in Figure 14. The hub was 3D-printed in two halves that were glued together once the rotor was fastened onto the motor shaft. The CAD drawings of the nacelle and hub are given in Appendix 9.2.3 and 9.2.4 respectively.

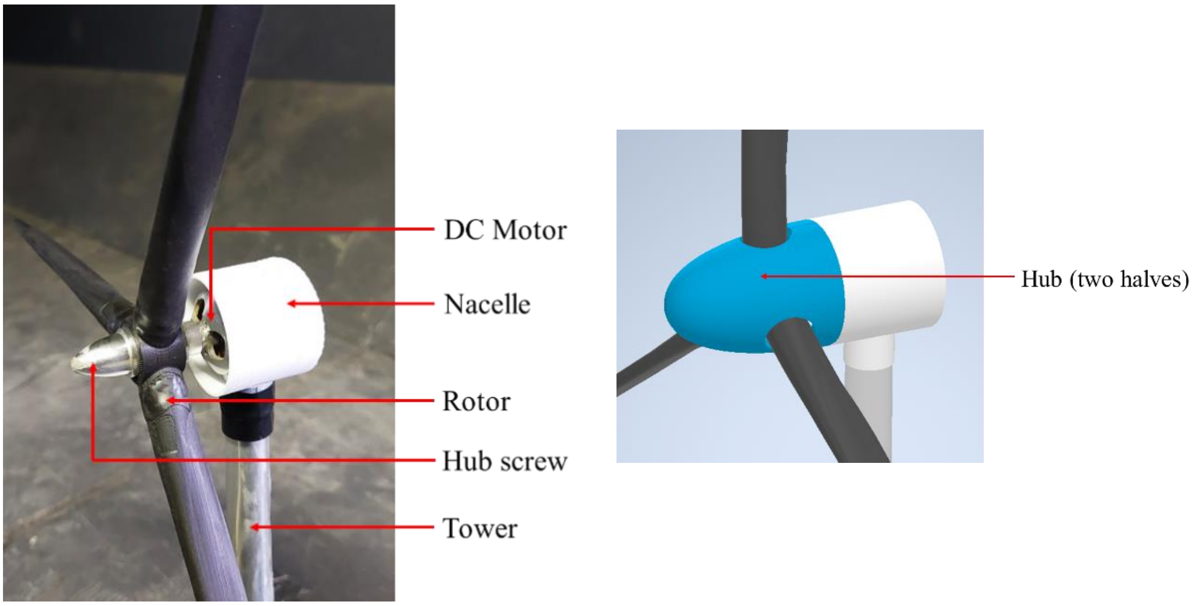

Figure 14. Nacelle, hub, motor and rotor connections of the wind turbine model

4.1.4 Balancing Apparatus

Balancing of the blades ensures that all the blades have the same mass and centre of gravity to prevent unwanted eccentricity and vibration. This is especially important as the blades have each been post-processed individually to make them smoother and it is important to ensure that any minor change in the mass or centre of gravity of the blades due to post-processing is accounted for. It is important to ensure that there are no vibrations during rotation [51] that can cause fatigue of the components and possibly structural failures, as well as possibly affect the measurements.

In order to balance the blades, a propeller balancing apparatus was used. The rotor was suspended on the balancing apparatus and allowed to rotate freely. The rotation of the suspended rotor blades indicates which blades are heavier and which are lighter. Mass can either be removed from the heavier blades by sanding them down or mass can be added to the lighter blades by sticking small pieces of tape on them. A balancing rig was built for the purpose of this research is shown in Figure 15. Two wooden legs were constructed and these were mounted next to each other on a wooden platform. The legs were spaced such that the rotor fit tightly between them and two indents were made to hold the propeller balancer in place. The rotor was suspended on the propeller balancer that allows it to spin freely. The heavier blades were sanded down until all blades were balanced.

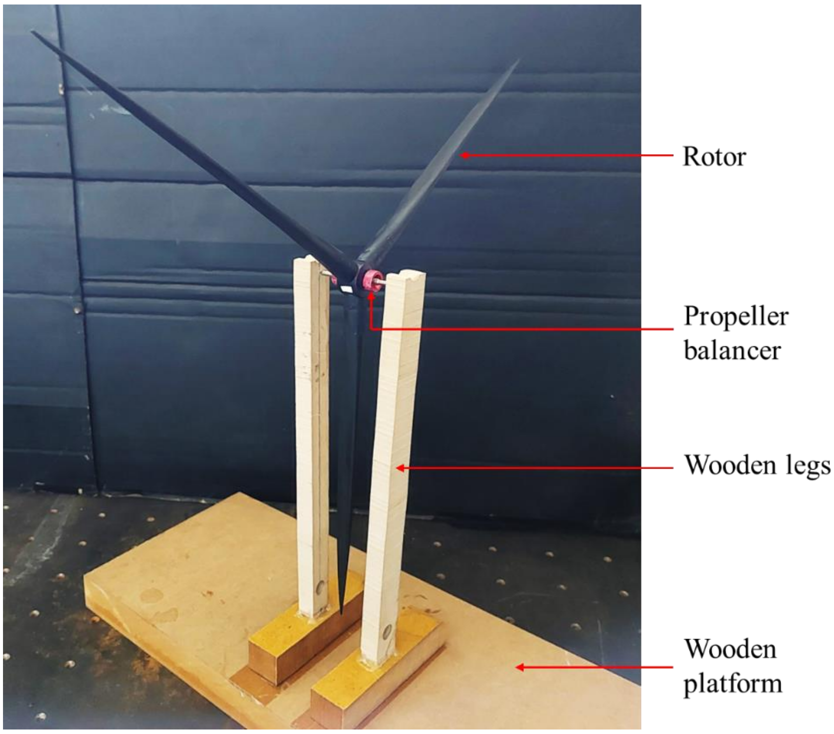

Figure 15. Balancing rig

4.1.5 Yaw Control of the Wind Turbine Model

Four design options were researched to control the yaw angle of the turbines. Since the turbine tower is cylindrical, either the entire tower can be rotated or just the rotor and nacelle itself can be rotated to get the correct yaw angle of the rotor blades with respect to the freestream.

Table 2. Evaluation of Different Design Options for Yaw Control

Design and Working	**Benefits and Drawbacks**
1. Turntable Mount the base of the wind turbine tower to the centre of a turntable in the wind tunnel. An illustration of the idea is shown below [52]. 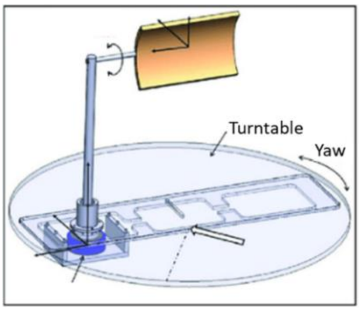 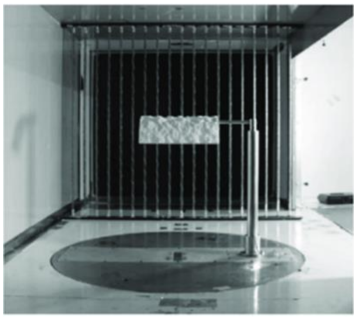	Benefit: • Most commonly used method for rotating objects in the wind tunnel. Drawbacks: • Existing cutout does not coincide with the placement of the turbines. • Turntable and rotation mechanics would need to be designed and fabricated. • Requires two large permanent cutouts in the wind tunnel.
2. Planetary Gear An outer ring gear would be attached to the top of the tower and the inner "gear" with one tooth would be attached to the inside of the nacelle. Rotation of the nacelle would allow different yaw angles. An illustration is shown below [53]. 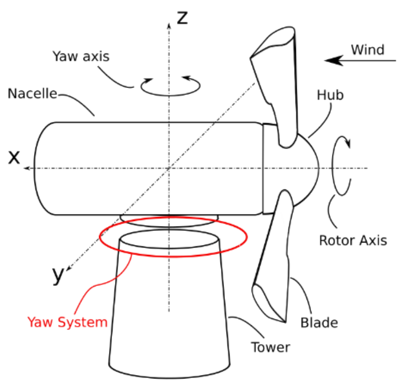	Benefits: • The nacelle can be held stable at different yaw angles. • No change to the wind tunnel is required. Drawbacks: • Gear teeth would need to be very small to facilitate multiple yaw angles. • The connection diameter (in red) is very small (14.7 mm) and fabrication of the meshing gear teeth would be challenging.

<table>
<tr><th>Design and Working</th><th>Benefits and Drawbacks</th></tr>
<tr><td>3. <u>Stepper Motor</u>
The base of the tower would be connected to a stepper motor, which controls the yaw angle of the turbine.
An illustration (adapted from Howland et. al) [54] is shown below.
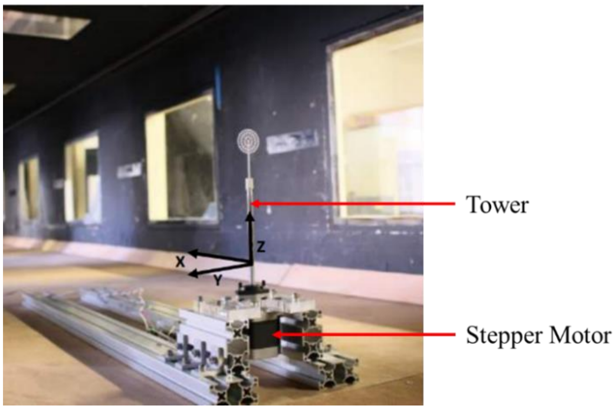
</td><td>Benefit:
Automatic control of the yaw angle.
Drawbacks:
Complication with the wires used to control the rotor that run through the bottom of the tower.
The tower has to be open at the bottom, making connection to the motor complicated.
Slippage of the motor.</td></tr>
<tr><td>4. <u>Tripod Stand</u>
The base of the tower would be connected to a tripod stand, allowing the turbine all the degrees of motion as the tripod stand.

</td><td>Benefits:
Multiple degrees of motion.
Relative ease in control of yaw angle.
Manual locking in place.
Firm support of the turbine.
Drawback:
Manual rotation to set different yaw angles.</td></tr>
</table>

It was chosen to implement design option 4 (tripod stand) for the reasons tabulated above and since it was the most practical method to implement and use. Although this design required manual rotation to different yaw angles, the front of the tower was marked and a compass stuck to the floor (seen in Figure 18) was used to consistently position the turbine at the correct yaw angle.

A tripod mount was used to mount the tower of the wind turbine to the tripod stand. It was designed so that the tower could be press-fitted into a hole in the tripod mount to keep it stable without requiring a permanent fixture. This was important for easy connection and disconnection between the turbine (inside the wind tunnel) to the tripod stand (underneath the wind tunnel). The tripod mount was also designed such that the cables running through the tower could run out of the tripod mount for connection to the power source and control devices. A threaded hole and additional side cutouts were applied to screw the mount tightly onto the tripod stand. See Figure 16 for an illustration of the tripod mount in use and the complete wind turbine model.

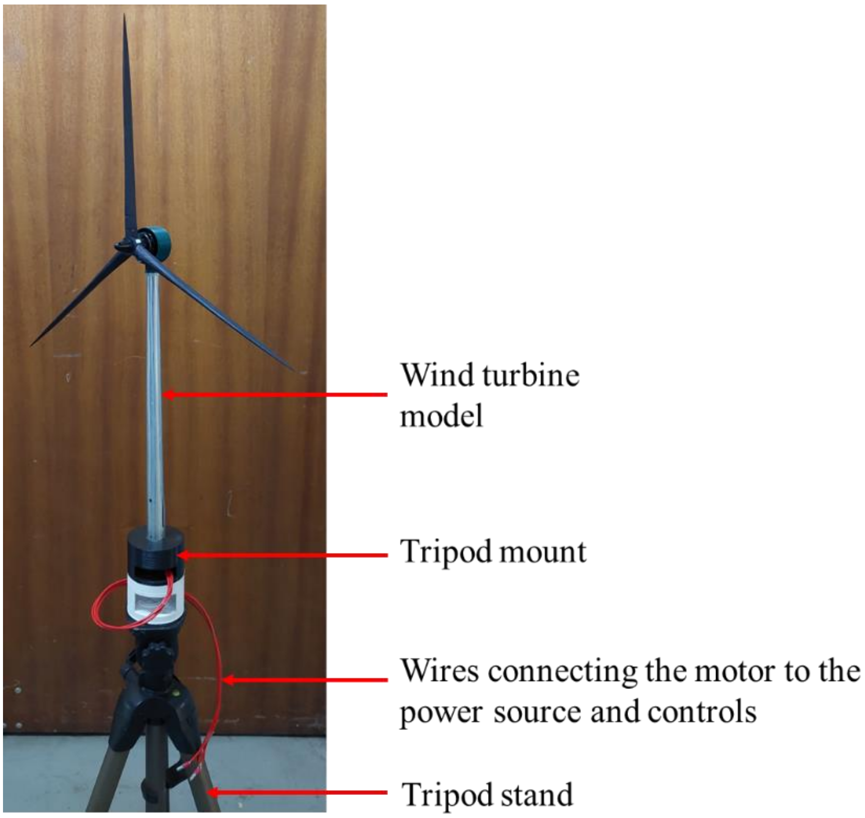

Figure 16. Full wind turbine model

4.1.6 General Setup used for Experimental Testing

The experimental setup used in the wind tunnels at both universities had the following characteristics. The wind turbines were aligned one behind another, five diameters (5D) apart as in the LES model. See Figure 17 for a schematic (not drawn to scale) of the setup of the turbines in the wind tunnel. Tests were conducted at a tip-speed ratio of 7.5, as in the LES model. An image of the wind turbine models in the wind tunnel is shown in Figure 18.

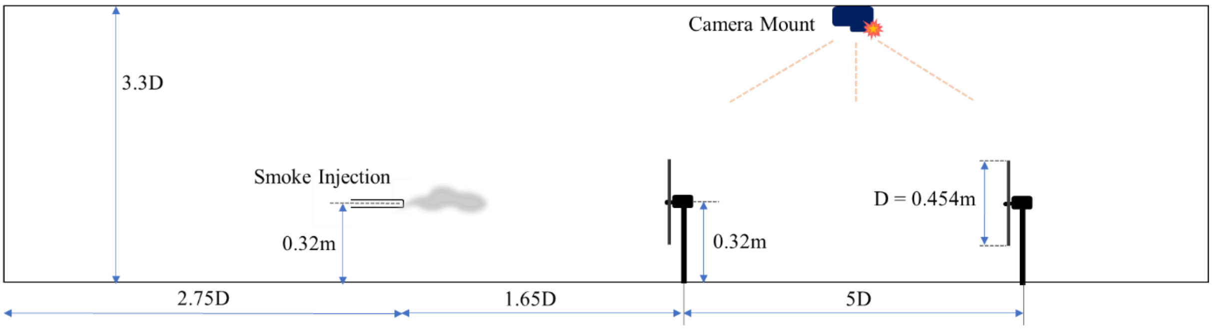

Figure 17. Experimental setup in the wind tunnel

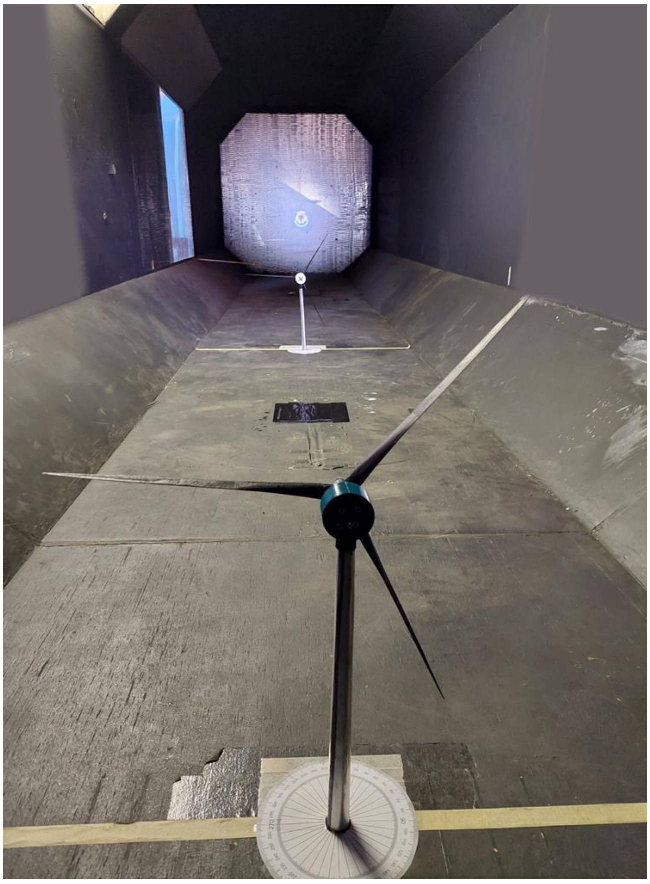

Figure 18. Wind turbine array in the wind tunnel

4.1.7 Smoke Visualisation

Smoke Machine and Liquid

To visualise the wake development, smoke was injected into the freestream in front of the upstream turbine and the smoke (and thus the flow) was tracked throughout the flow field until its impingement on the downstream turbine. The smoke machine used was the Safex Nebelgerat fog generator F2004 seen in Figure 19. The two liquid compounds available were the Safex Normal Power Mix and the Safex “D” Spezial. Both fluids were classified as very dense and long-lasting, but based on the datasheet (given in Appendix 9.1.2), the Normal Power Mix is more appropriately used for technical applications whereas the “D” Spezial fluid is used for photography purposes and disperses more rapidly, which is undesirable [55]. Both liquids were tested in the wind tunnel and it was found that the Normal Power Mix was much more visible and dispersed slower which allowed the flow to be visualised much further downstream. This smoke reached just beyond the downstream turbine and therefore was used.

Smoke Injection Method

Smoke was released from the smoke machine through a 2 mm hole encased in a 50 mm pipe. To visualise the flow as best as possible, different injection positions, orientations of the smoke and sizes of injection tubes were tested.

It was initially attempted to inject the smoke perpendicular to the freestream. Most commonly, the smoke is allowed to follow the natural path of the freestream. However, the push-button release does not allow control of the intensity of the smoke injection and perpendicular injection projects the smoke past the upstream turbine. Therefore, parallel injection was chosen.

To reduce disturbance, the smoke needed to be injected as far upstream as possible. However, this was limited by the dispersion rate of the smoke. Through testing it was determined that the optimal injection point was 1.65D upstream of the upstream turbine, as seen in Figure 17. The smoke was injected at the centre of the rotor, as opposed to either edge, as the centre-line is of most interest. This also accounts for the downstream expansion of the wake. As the wake expands in a canonical form, it is expected to reach the edges of the rotor. Therefore, injecting the smoke at the centre will allow for the majority of the rotor area flow to be captured.

Different sizes and materials of piping were tested for injecting the smoke to minimise the condensation of the smoke and optimize the velocity of the smoke exiting the pipe. Though the temperature was not measured, the liquid was heated significantly above the vaporisation temperature. An elbow pipe was required to direct the smoke parallel to the flow. A 50 mm diameter plastic elbow pipe and a 27 mm diameter metal pipe were tested. The final setup used was a 6 mm diameter rubber pipe pushed through a 9.5 mm diameter metal elbow pipe. Condensation of the smoke was minimised with the rubber pipe, which delayed dispersion, and the metal pipe allowed for suspension and correct orientation in the wind tunnel. The small diameter was also beneficial to reduce the disturbance of the flow before it reached the upstream turbine. Figure 19 shows the smoke generator used.

Figure 19. Smoke generator

Cameras Used for Flow Visualisation

To map out the deflection of the wake, the top view of the wind turbine array needs to be captured and to observe the kidney-shaped deflection that is expected, the back view is required. Each view needs to be captured in its entirety as combining snapshots will not work given the transient nature of the flow. To capture the full flow field from the upstream turbine to the downstream turbine, three possible camera options were evaluated, namely a GoPro camera (Hero 10), a Digital Single-Lens Reflex (DSLR) camera (D7200), and a phone camera (Samsung Galaxy A52s) based on availability.

Table 3. Comparison of Different Camera Options

Feature	**GoPro Camera**	**DSLR Camera**	**Phone Camera**
Video quality	4k at 120 fps 5.3k at 60 fps	1080p	4k at 30fps 1080p at 60fps
Weight	158 g	676 g	187 g
Size and Shape	71 mm x 56 mm x 33 mm	135 mm x 76 mm x 107 mm • Lens protrudes from the body making mounting more difficult and creating greater disturbance	160 mm x 75 mm x 8.5 mm
User interface	User-friendly • Settings are easily accessible and well documented • Easy to choose appropriate combination of settings	Less user-friendly in comparison • There are an extensive number of combinations of settings [56]	User-friendly • Fewer settings, but less optimization can be done to capture the best footage
Other	Designed with the priority of being able to capture high quality video, with image capturing being a secondary function [56]	Designed with the priority of capturing high quality still-images and video capture is a secondary function [56]	Less durable compared to the other options

All three cameras were tested with the setup in the wind tunnel to determine the span of the flow field that each can capture, the quality each can achieve in this application and the ease of use. Figure 20 shows the comparisons of the different video captured by each camera using one frame. It is observed that the GoPro captures the widest range and longest depth of field.

Figure 20. Comparison of the different cameras

The DSLR camera captures clear video, but it is not able to capture the entire flow field (a length of 2.27 m or 5D) unless it is placed 500 mm away from the window on the outside of the wind tunnel. The longer the focal length, the narrower the field of view [57] and a relatively long focal length and a very wide field of view is required – without any fisheye distortion. Placing the camera outside the window adds a complication because of the reflections of the window that obscure the video of the wake. It was not possible to make the surrounding in the lab completely dark because there are many windows and there is other equipment present in the lab being used by other people. Therefore, it was decided to create an enclosed space with black material for the camera to be placed under that blocked out most of the reflections. However, placing a camera further from the window also means that some of the flow field near the window cannot be captured.

The phone camera was able to capture the full flow field but its quality is inferior to other options.

The GoPro was also able to capture the entire flow field in good quality and due to the properties listed above, such as its high-quality video capture, small size and durability, the GoPro was chosen to be used to capture the smoke visualisation tests.

Camera Mount

Given that the top and back views needed to be captured, the cameras needed to be placed above and behind the flow field to prevent obstruction of the flow. The camera at the back was mounted to a tripod stand at hub height. For easier accessibility, a camera mount was designed to mount the camera to the ceiling of the inside of the wind tunnel to capture the top view. It was possible to place the GoPro inside the wind tunnel because it is small and would not obstruct the flow significantly.

The final design (image shown in Figure 21 and detailed drawings in Appendix 9.2.5) accounted for the following considerations:

- The mount needed to be secured firmly to the wind tunnel ceiling.
- Reflections from the camera screen in the glass panel of the test section needed to be blocked out.
- Ease and accuracy of mounting.
- Access to features such as the stop-start button and touch-screen interface on the GoPro.
- The GoPro needed to sit completely flat to avoid distortions.

The mount was 3D-printed taking these considerations into account. It was 3 mm thick to be sturdy enough to fasten the screws into without bending or warping as well as hold the weight of the camera. These design specifications, as well as the completed 3D-printed mount fastened to the wind tunnel ceiling, are illustrated in Figure 21.

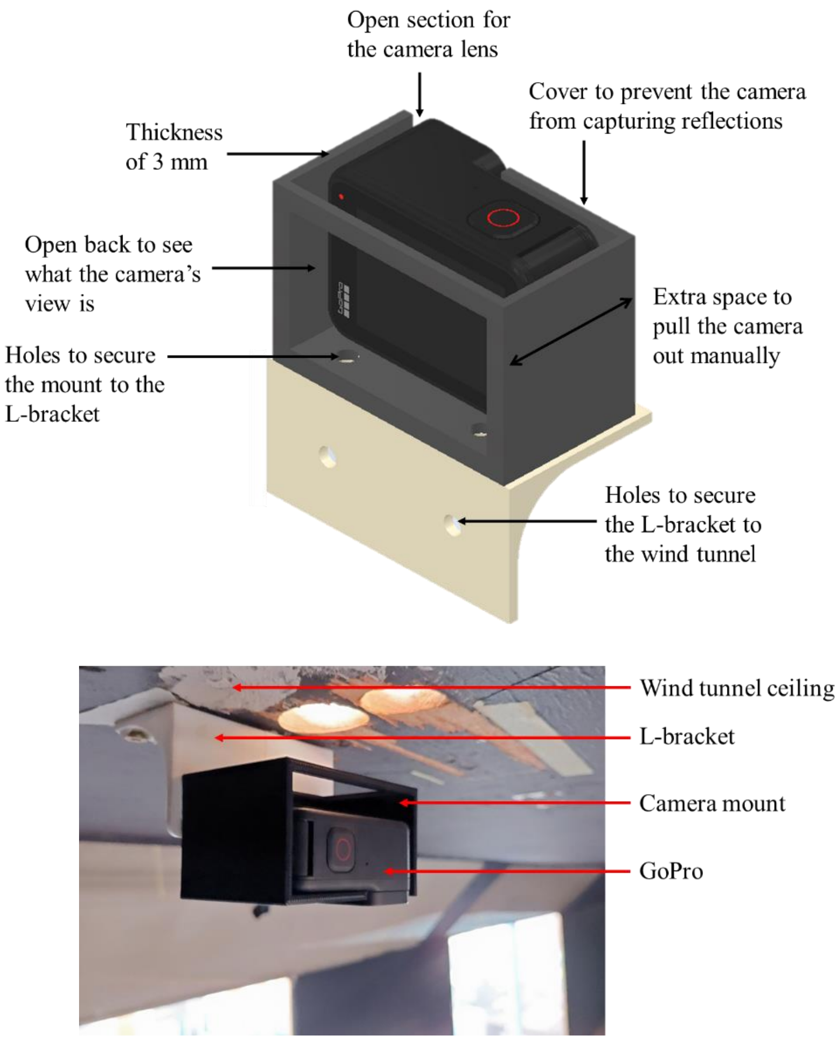

Figure 21. Design of the camera mount (top) [58] and the 3D-printed mount inside the wind tunnel (bottom)

Data Acquisition and Processing

Two cameras were used to capture the two different views of the wake at the same time. Both cameras were set to record linear video (with no distortion) with a resolution of 4k and 120 fps for the highest quality.

Running the motors for too long would cause them to heat up excessively since they are encased in the nacelle. Therefore, the tests needed to be conducted in as short a time as possible. The smoke was injected a few times in each run to get a variety of visualisations.

The raw data captured was video footage. From this, each frame of the video was analysed and screenshots of the video were captured at the moments where the entire flow field was most visible, as seen in Figure 22. To visualise the wake better, the images were edited to highlight the flow more clearly, especially near the downstream turbine where it was difficult to identify the edges of the wake. A highlight function in Microsoft PowerPoint[1] was applied and the brightness was increased by 60% and the contrast was increased by 70%. To map out the deflection of the wake, the edges of the wake were identified and red T-shaped borders were placed at these edges. To find where the middle of the wake impinges on the downstream turbine, a dark red line was drawn between the edges and the middle point of this line was identified, as seen in Figure 23. To assist with quantifying the wake deflection, markings were placed on the wind tunnel floor at each turbine that marked out the distance from the centre of the hub in increments of 0.1D. These lines were made more visible with the use of the yellow lines added during post-processing, as seen in Figure 24. An orange line was used to indicate the centreline of the turbine array. This process was repeated for ten images at each yaw angle. By comparing the impingement of the wake on the downstream turbine at the different yaw angles, observations can be made about how the wake is deflected as the upstream turbine is yawed.

[1] https://support.microsoft.com/en-us/office/edit-pictures-1d4bf84a-ab8b-4b3e-be78-78b0ed9f4ede

Figure 22. Screenshot of smoke visualisation of the wake from a video recording

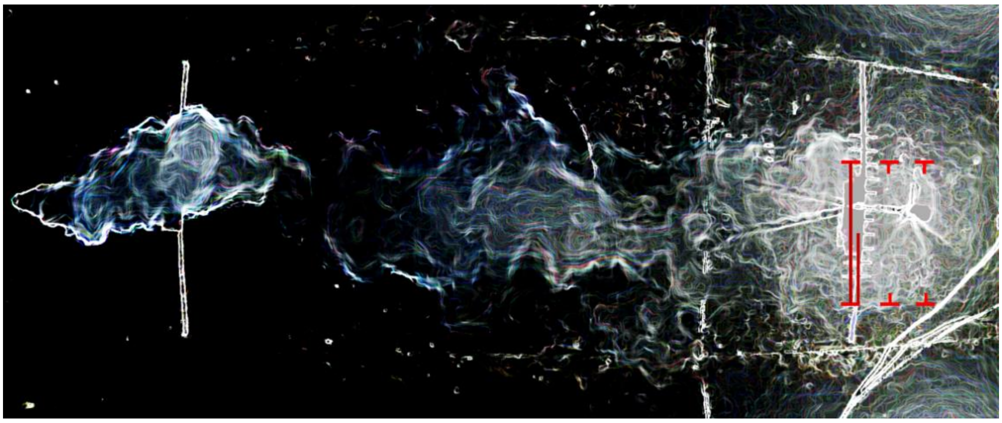

Figure 23. Edited image of the smoke visualisation, boundaries highlighted and the middle of wake identified

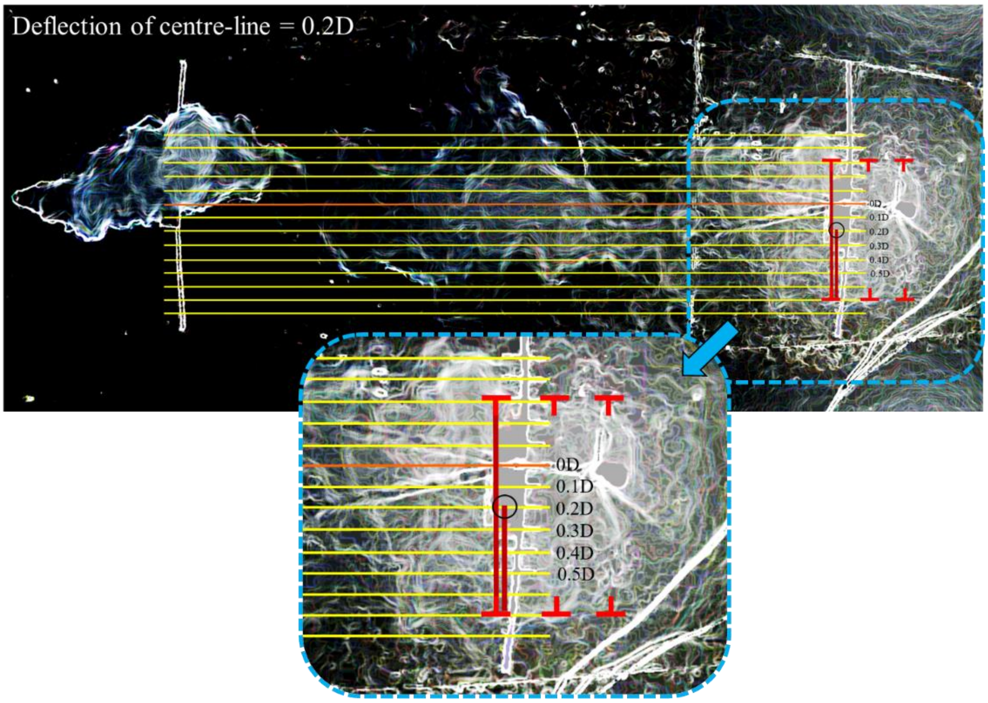

Figure 24. Centre of wake deflection quantified from the smoke visualisation image

4.1.8 Hot-Wire Anemometer

Hot-wire anemometry tests were conducted in the boundary layer wind tunnel at University of Bristol. Since the wind tunnel facility was new to the university, calibration of the wind tunnel was needed to be conducted first. This involved determining the height of the boundary layer as well the turbulence intensity that would be used for all future measurements. Calibration consisted of setting up the hot-wire anemometry traverse system, calibrating the hot-wire probe and taking velocity measurements at different positions of the wind.

Traverse system

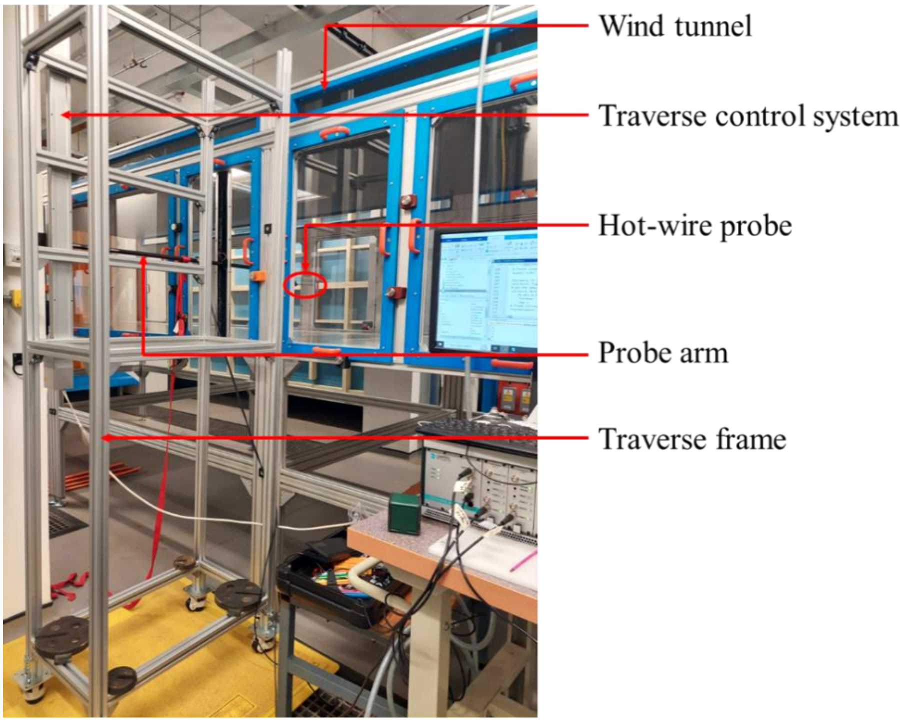

Figure 25. Traverse system used for the hot-wire anemometer tests

To more efficiently traverse through the positions within the test section for hot-wire measurements, a dedicated traverse system was assembled, as seen in Figure 25. The system consisted of an Aluminium support with rails onto which the linear stage actuator was mounted. The linear stage was controlled by a control module, which was connected to a workstation and the motion was managed by LabView software to achieve traverse motion at a fine resolution of 8 mm. At the other end of the linear stage, a probe arm was attached and extended from the outside of the wind tunnel into the test section, perpendicular to the freestream, via a cutout in a window (see Figure 26). The cutout in the wind tunnel window was covered with brushes to reduce its exposure to outside effects. The probe arm was made from steel to increase its rigidity and thus reduce its susceptibility to vibrations that would be falsely detected as turbulence. It had the shape of an aerofoil to reduce drag and to minimise disturbance to the flow in the test section, since it was placed directly in the freestream and very close to the measurement location. The hot-wire probe was clamped onto the end of this arm, parallel to the freestream and the wires of the probe were secured to the arm with tape as shown in Figure 26.

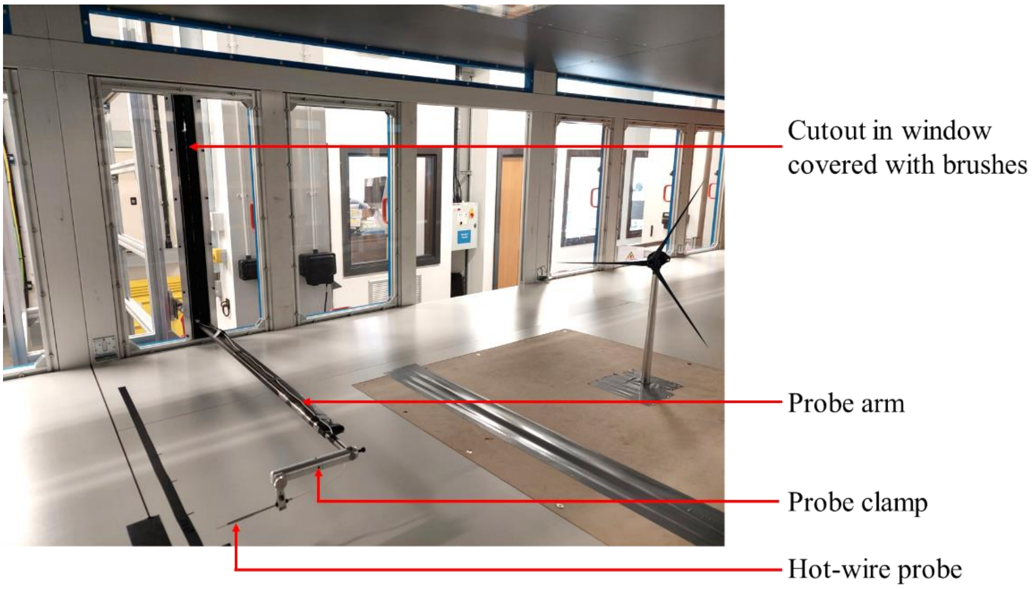

Figure 26. Setup of the hot-wire probe inside the wind tunnel

The purpose of the traverse system was to allow the hot-wire probe to move autonomously to take multiple readings. This particular traverse system allowed the probe to move in the vertical direction (z-direction) to capture multiple points along a single streamline. To capture different vertical streamlines at different spanwise (y-direction) and streamwise (x-direction) locations, the probe arm needed to be manually moved to another location on the traverse system frame. Figure 27 illustrates the directions of automatic and manual traversing.

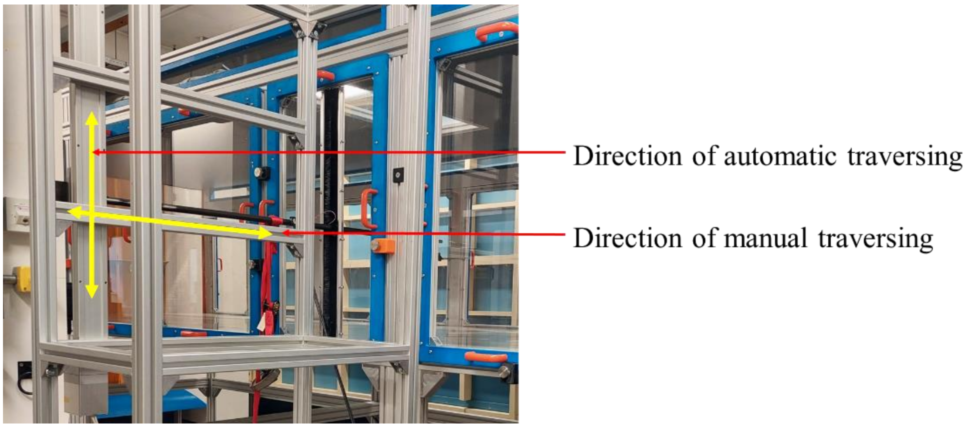

Figure 27. Traversing directions of the hot-wire probe

Probe Calibration

The aim of the probe calibration is to obtain the transfer function between the voltage registered from the acquisition system to the actual measured velocity. To calibrate the hot-wire probe, the probe was secured onto the probe calibrator seen in Figure 28. The calibration procedure is outlined below.

Setup:

- Pressurised air was supplied to the calibrator to produce a fixed, known flow rate that exits the calibrator nozzle.
- All the parameters such as probe resistance and overheat ratio were then adjusted in the StreamWare Pro software to account for the specific two-wire probe used (55P16 probe).
- The probe was operated to register the voltage reading corresponding to a known velocity.

Calibration:

- The control valve of the calibrator unit was turned to “high” (at 50.2 m/s).
- The probe was first rotated to an angle of -40° and left to stabilise for a few seconds, before the measurement was taken. This process was repeated in increments of 10° until an angle of +40°. An example of the resulting curve fit is shown in Figure 29.
- The same process was repeated when the air pressure was turned to low (at 1.54 m/s).

This process results in the generation of coefficients that are used in the process of converting the voltage readings into velocity measurements. This is carried out by a fourth-order polynomial fitting, similar to that documented in [59].

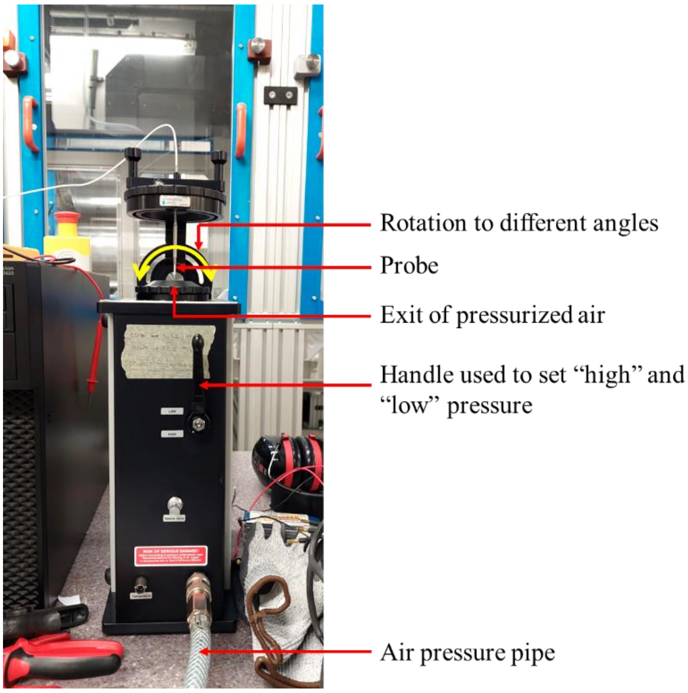

Figure 28. Hot-wire probe calibrator

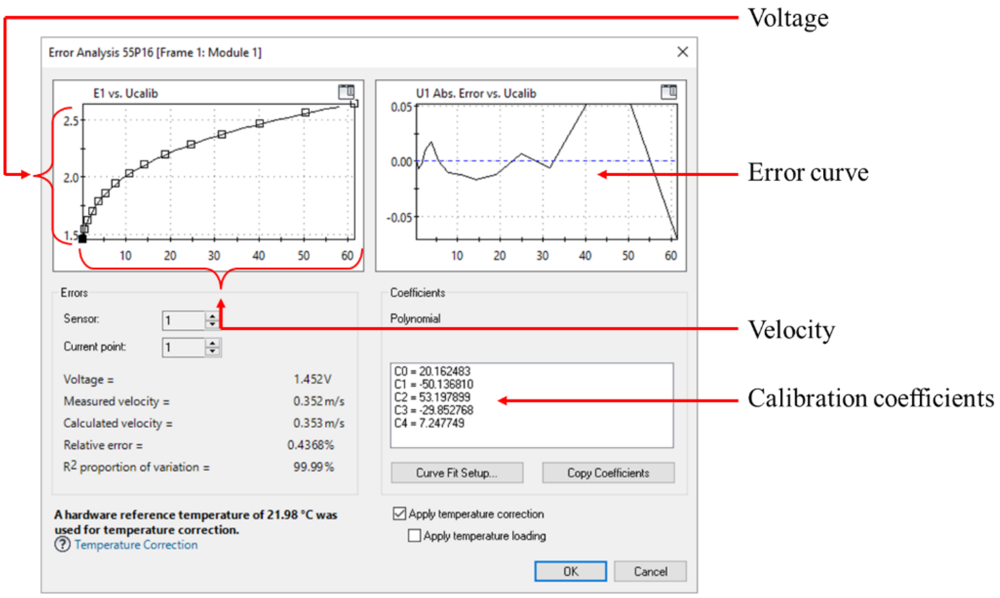

Figure 29. Example of hot-wire probe calibration curves and coefficients

The first set of calibration tests were conducted towards the end of the wind tunnel, 12 m downstream from the start of the test section, where the boundary layer was expected to be almost fully developed and where it was expected that most testing would take place. The hot-wire probe was initially placed in the centre of the cross-section at y = 0 mm and measurements were taken from z = 50 mm to z = 800 mm. This offset was accounted for since it was not possible to position the probe exactly on the floor (at z = 0 mm) given the fragility of the probe. Measurements were also taken at the spanwise locations of y = +400 mm and y = -400 mm to map the boundary layer and turbulence intensity across the span of the wind tunnel. The red dotted lines in Figure 30 illustrate the locations at which the calibration measurements were conducted.

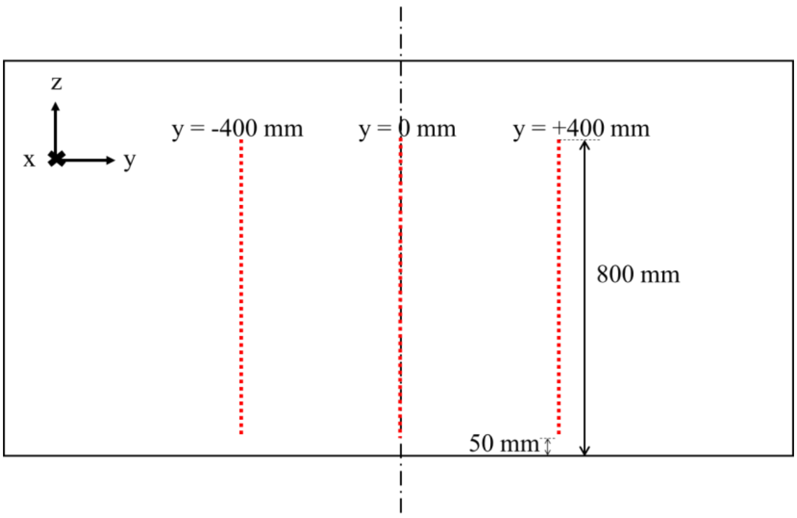

Figure 30. Hot-wire calibration measurement locations from the front view of the wind tunnel

The probe was moved vertically in intervals of 8 mm as this was the shortest distance that the traverse system could read. The motion was controlled using a LabView script that had been programmed for this specific traverse system. This software allows one to specify the acceleration of the probe during its translation to the next point of measurement, the location of the points where measurements should be taken, how long the probe should remain stationary at a point before measurements should be taken (to allow time for stabilisation to reduce noise and turbulence) and where the data recorded should be saved.

After the measurements were taken, the data was processed using MATLAB. The resistance readings were converted to velocity and this was used to plot the boundary layer development as well as the turbulence intensity.

Hot-wire tests

The setup above was also used to conduct the hot-wire tests for the wind turbine array. The turbines were placed in the same place where the calibration took place, a distance of 5D (2.27 m) behind one another. Tripod stands were used to control the yaw, as described in section 4.1.5. The wind tunnel was set to have a freestream wind speed of 2.2 m/s and the turbines were set to rotate at 700 RPM to ensure the same tip-speed ratio of 7.5 used in the other experimental tests conducted.

Two tachometers were set up on the opposite side of the wind tunnel. They were connected to pre-coded LabView software. This allowed them to control the motors directly, which allowed for accurate control of the speed of the turbines. To power and control the motors that drive the rotors, each motor was connected to a power source and an Electronic Speed Controller (ESC), which were both connected to a Data Acquisition (DAQ) system to allow for control and data capture through the LabView user interface.

As opposed to the calibration tests, these tests were conducted using a single-wire probe because only the velocity in the x-direction was of interest. Also, there was less risk in working with a single-wire probe as it could be easily closed when needed to prevent damage. The calibration process is similar to that outlined in section 4.1.8 - Probe Calibration.

As was done for the calibration tests, measurements were taken in vertical streamlines. A total of 32 points were measured in a single vertical streamline. Each point had a sampling duration of 18 seconds (5 seconds for stabilisation, 3 seconds for recording the data and 10 seconds to move to the next point) and a sampling frequency of 32 768 Hz. The motors were switched off for 5 minutes after each vertical streamline to allow for cooling. Due to the time constraints given to conduct testing, five spanwise locations and two streamwise locations were tested. These locations are illustrated in Figure 31. These spanwise locations were tested to attempt to capture the deflection of the flow as the yaw angle was increased. At each vertical streamline, a total of 7 combinations of yaw angles were tested. Previous studies conducted at an upstream turbine yaw angle of 30° showed that the wake is typically deflected between y = 0.75D [24], [54] and y = 1D [54], with another study showing a deflection of 0.6D at a yaw angle of 25° [60]. Therefore, it was decided to measure at the spanwise locations of y = 0.5D, y =

0.75D and y = 1D on the side to which the wake would deflect. The centreline of the rotor and the right side of the rotor were also important to capture a cross-section of the wake. It was initially attempted to capture the flow at the streamwise locations of x = 2.5D and x = 5D to see how the wake develops at the midplane between the two turbines and then at the downstream turbine as this is of most importance. However, due to the length of the hot-wire probe, the length of the probe clamp and the position of the window that the probe can be passed through, the closest to the downstream turbine that the measurements could be taken was x = 4D. This was the maximum number of tests that could be conducted in the time that was available.

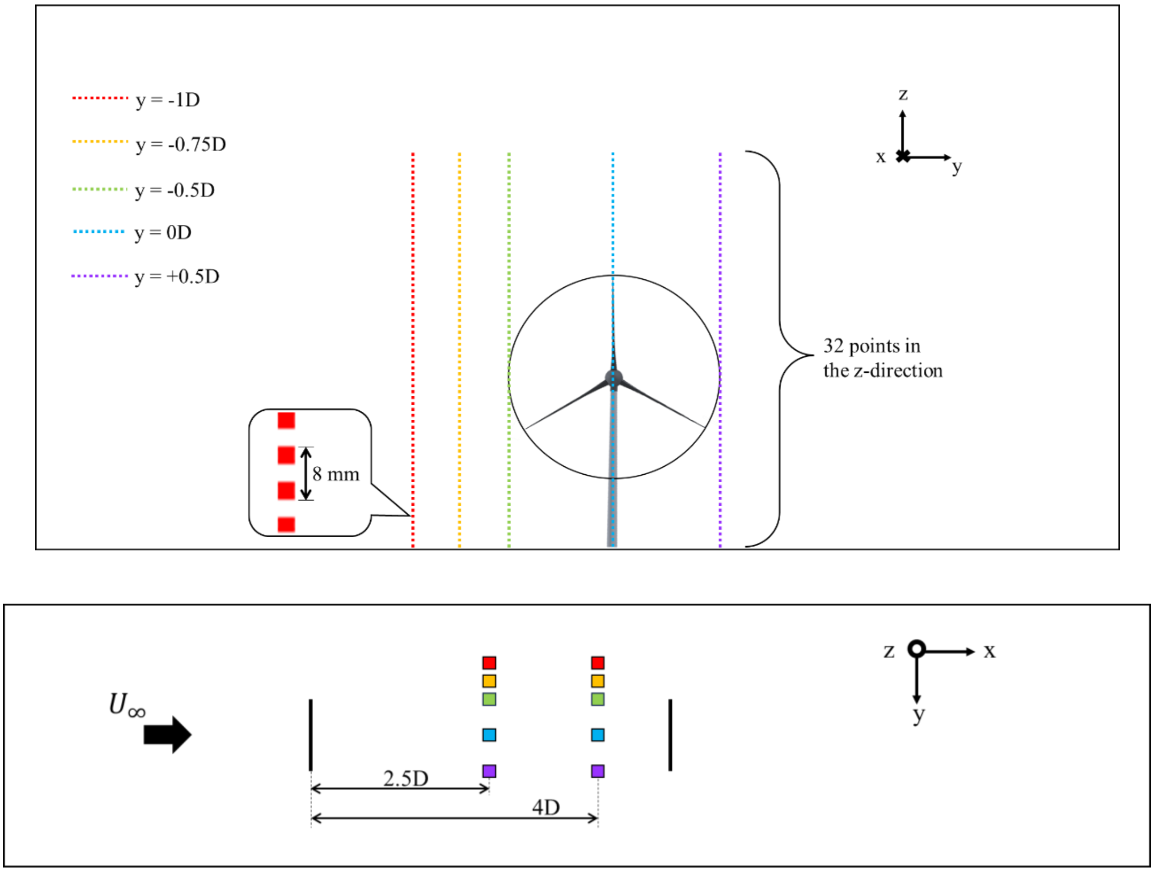

Figure 31. Hot-wire test locations from the front view (top) and the top view (bottom)

Figure 32 shows the experimental setup used to conduct the hot-wire tests on the wind turbine array.

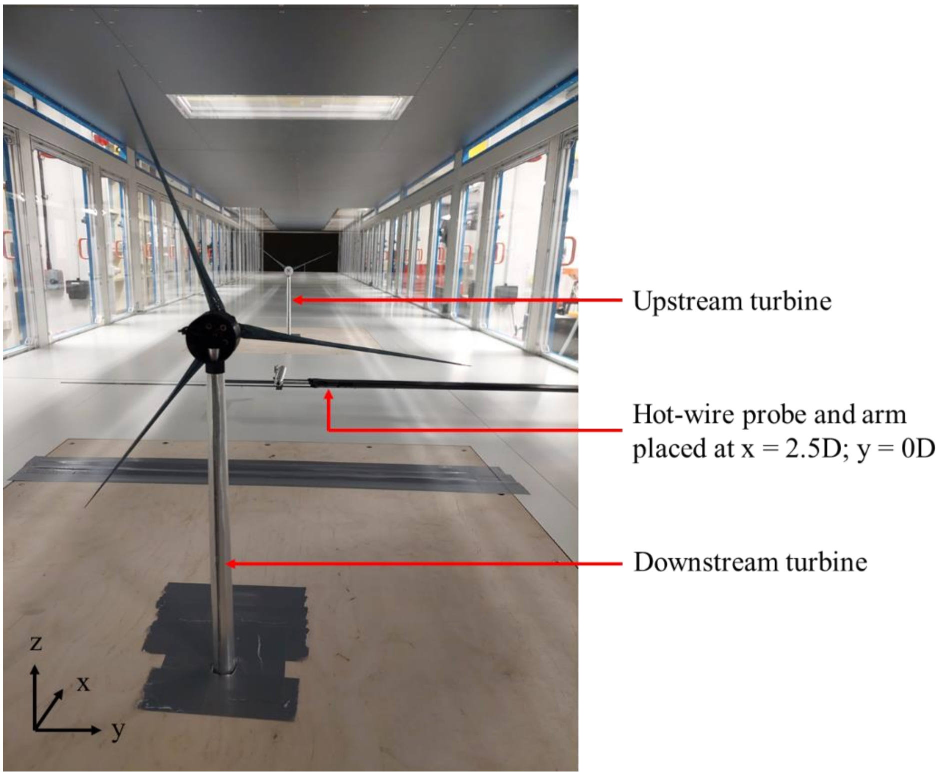

Figure 32. Setup for the hot-wire measurements in the wind tunnel

Data Acquisition and Processing

In order to ensure all the tests were conducted in the time allocated, the test needed to be conducted in the most efficient way. Given that it takes a much longer time to move the entire setup to different spanwise and streamwise locations compared to changing the yaw angles of the turbines, the traverse system was kept in one place for all combinations of yaw angles before being moved to the next location and testing all combinations of yaw angles.

The raw data output from the hot-wire measurements was tdms files. To read these files, the TDMS Reader in MATLAB was used to convert the readings to voltage values. These voltage values and the calibration coefficients generated during the calibration process were used to solve for the correct corresponding velocity values using King's Law. The equation for King's Law is given below.

$$Velocity = C_1 + C_2 v + C_3 v^2 + C_4 v^3 + C_5 v^4 \tag{4}$$

where $C_x$refers to the different calibration coefficients and v refers to the voltage output from the TDMS Reader.

This process was repeated for each of the 32 points measured in the vertical streamline and then for all the different streamlines in the spanwise and streamwise directions at all combinations of yaw angles.

4.1.9 Force Tests

To quantify and analyse the effect of yaw on the loads experienced by a downstream turbine, force measurements were conducted. A force sensor was modified and built to measure the loads exerted on the downstream turbine when the upstream turbine is yawed and when both turbines are yawed.

To analyse the full extent of the upstream turbine yaw on the downstream turbine, one force (Fy) and two moments (Mx and Mz) were measured. See Figure 33 for an illustration of these and the direction conventions used.

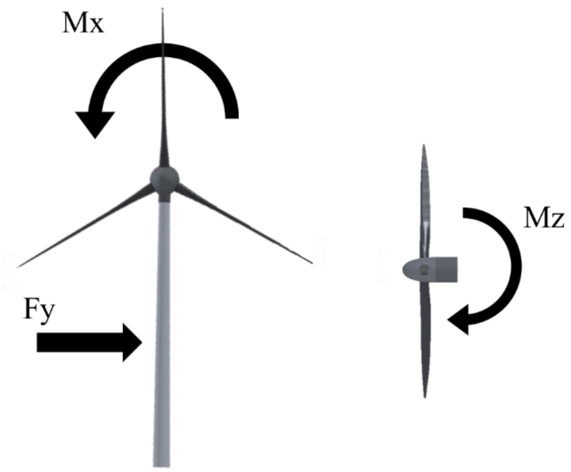

Figure 33. Positive directions of the forces and moments exerted on the downstream turbine

Force Sensor Design

The force sensor and operating details were originally designed by Prof. KB Lua from the National Yang Ming Chiao Tung University in Taiwan [61]. Due to the design being in the process of a patent (Taiwan Patent I866403), specific details of the force sensor were communicated privately and are excluded here. Further design alterations to the force sensor were required to be able to use it for the current setup, such as the integration with the tripod mount and accommodation of the wires from the strain gauges. The final force sensor design consists of 16 strain gauges that are connected in eight Wheatstone half-bridges. Each half-bridge was connected to a different channel on the DAQ system. Half-bridge configurations were used because it has a higher sensitivity compared to a quarter-bridge which is necessary to detect and measure the wake effects.

The general design of the force measurement system is shown in Figure 34. There are four rectangular bars and one strain gauge is mounted to each of the four faces of a rectangular bar. 350Ω linear strain gauges (details given in Appendix 9.1.3) were used instead of the 120 Ω strain gauges to prevent the strain gauges from burning out and to enhance the sensor response. For ease of mounting and based on availability, 5 mm Kyowa strain gauges were used.

As shown in Figure 34, the force sensor has a top plate on which the tower of the wind turbine is mounted to. As the wake impinges on the turbine the tower is deflected causing the top plate, and thus the bars, to bend. This results in readings from the strain gauges. The bars are positioned in this way such that a total of five different forces and moments can be measured – Fx, Fy, Mx, My and Mz. However, for the purpose of this study, only force Fy and moments My and Mz will be analysed. The individual force sensor components were manufactured by the lab workshop at Wits and was then assembled.

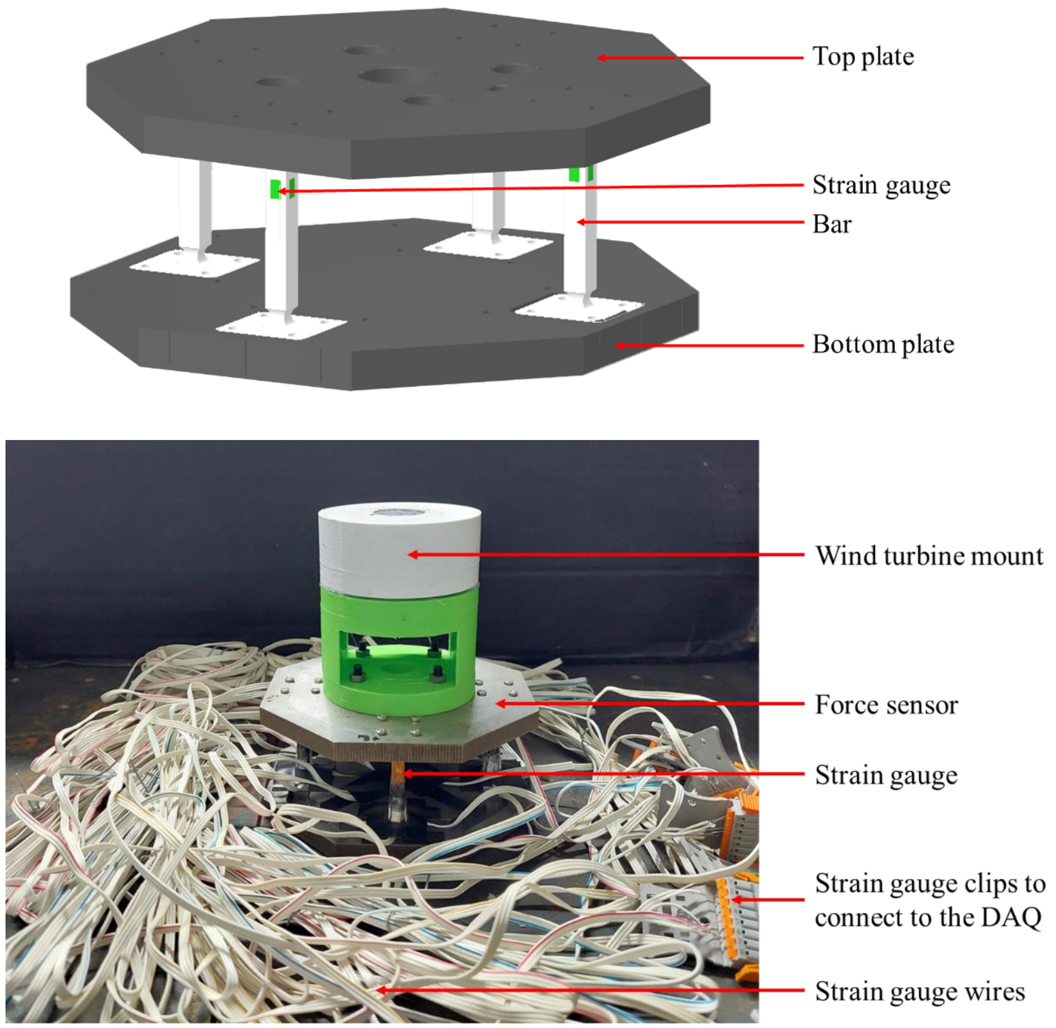

Figure 34. Force sensor design (top) and assembled (bottom)

Force Sensor Calibration

The force sensor was calibrated to determine the correlation between the magnitude of the force and the strain readings. Different forces were applied to pull the tower in the x and y directions. Different masses were attached to a string which was fed through a pulley to keep the force applied at the correct location, and the string was tied around the tower of the wind turbine at two locations – at the top of the tower under the nacelle (as seen in Figure 35) and at the middle of the tower, as these are the reference locations where the forces and moments will be measured about.

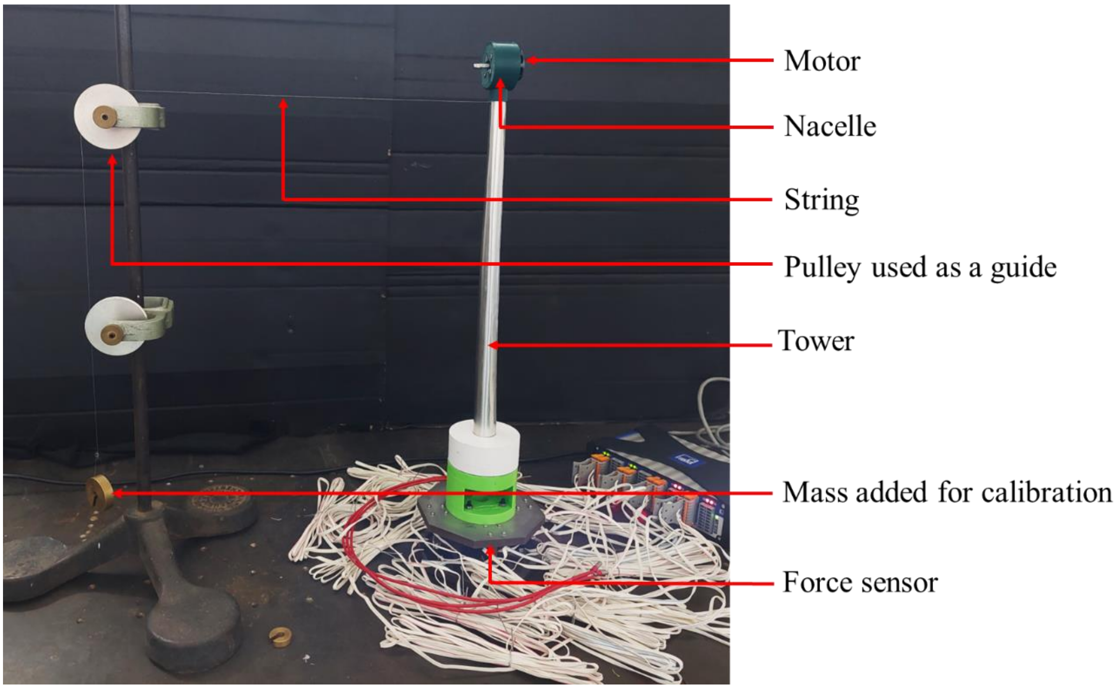

Figure 35. Calibration setup of the strain gauges

The masses were applied in increments of 10 g from 0 g to 100 g. Masses were added every 5 seconds to allow the strain gauge readings to stabilise once a new mass was added. Readings were sampled at a rate of 20 Hz. An average of the readings was taken for each mass and a mass versus strain curve was plotted for each of the eight strain gauge pairs (SGPs), as seen in Figure 36. An equation was generated from each curve that corelates the force measurement to the strain reading.

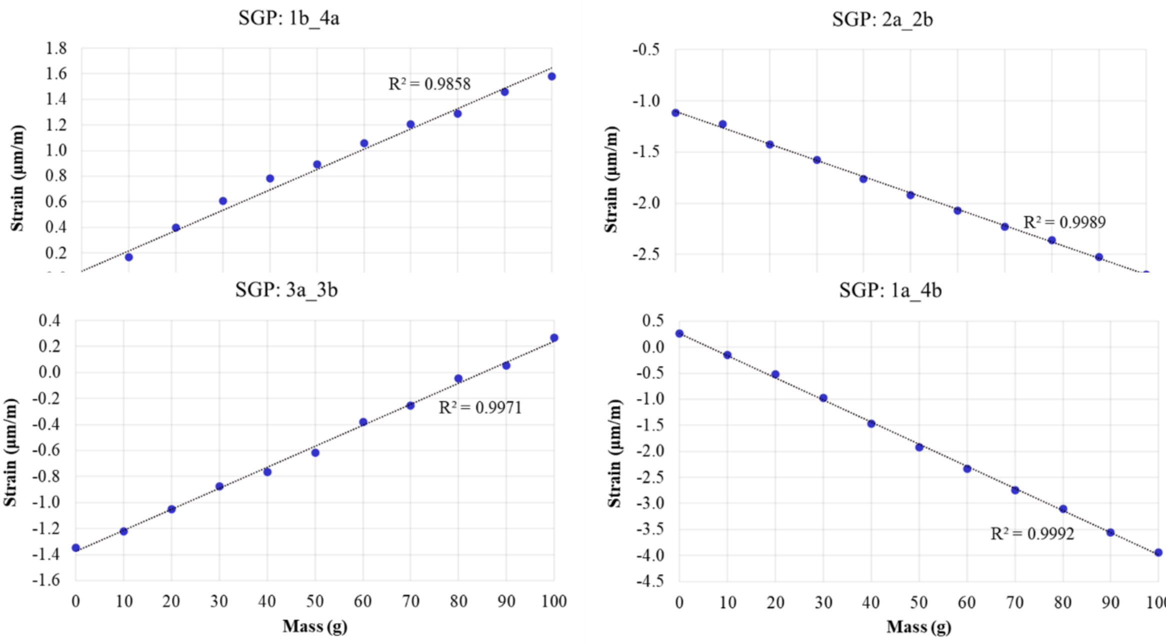

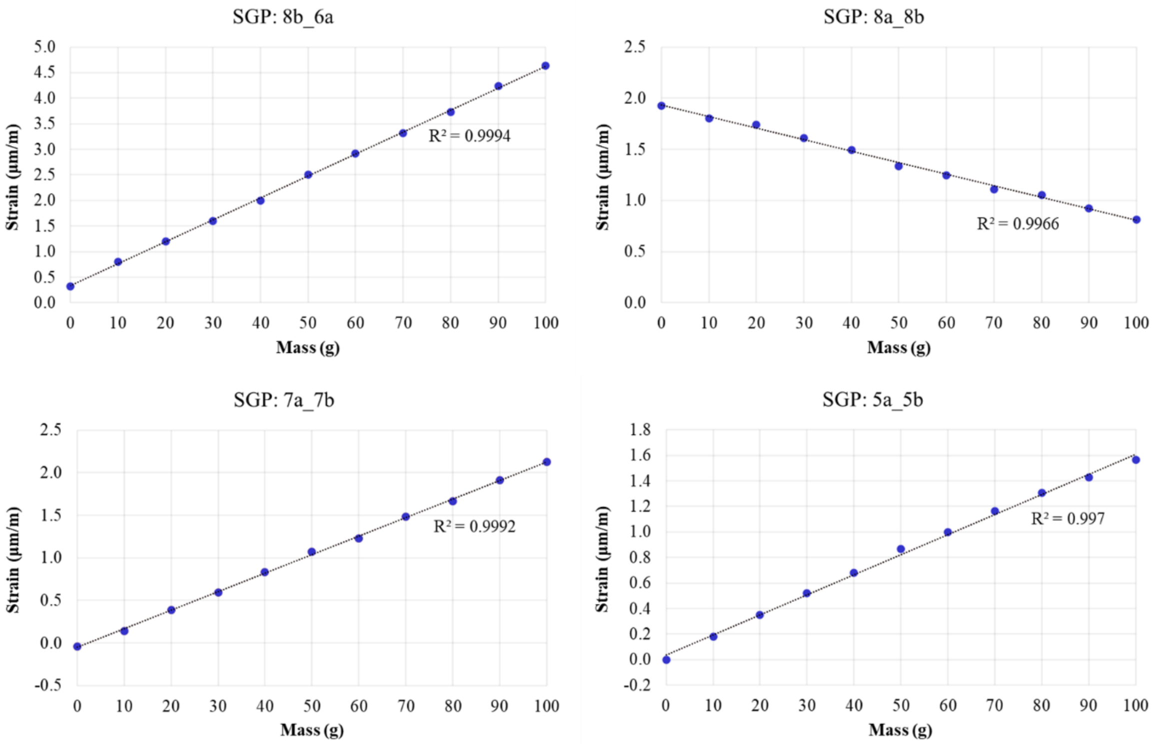

Figure 36. Calibration curves for the eight strain gauge pairs

Force Data Acquisition and Post-Processing

The process used for the force measurements was as follows. The wind tunnel was set to the required freestream speed of 1.9 m/s and left to run for approximately 15 minutes to get a true reading of the zero condition, which is just the freestream air impinging on the turbines when they are stationary. After each yaw angle was changed, the flow was left to stabilise for 10 seconds, the turbines were set to 600 RPM and the flow was left to stabilize for another 10 seconds. A DAQ was used to record the readings at a frequency of 20 Hz for approximately 5 seconds.

To determine if a time-average of the readings could be taken across the time that the data was recorded, a moving mean and a low-pass filter were applied to the original data and the standard deviation was calculated. An example of the curves plotted for the strain gauge pair 5a-5b is seen in Figure 37. The moving mean curve indicated that data points did not drift significantly from the mean. The low-pass filter indicated that the data points oscillate in a sinusoidal curve around the average and the standard deviation for this varied between 0.09 and 0.32. The sinusoidal curve can be attributed to the rotation of the blades. These two values indicated that a time-average of the data points could be taken. These time-averaged readings for each strain gauge were fed into the respective calibration curves to generate force outputs and these forces and moments were plotted.

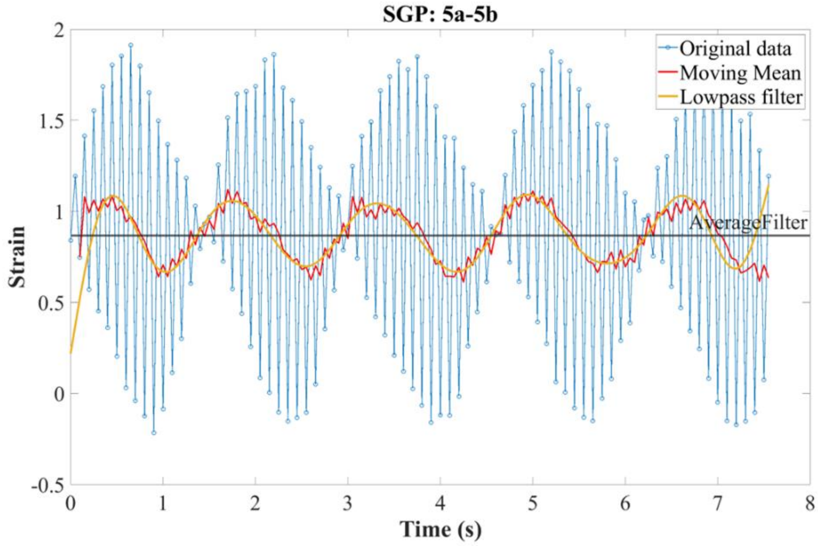

Figure 37. Post-processing curve of the force data

4.2 Surrogate Model Methods

4.2.1. Reduced Order Model Method

The first part of a surrogate model is to create a Reduced Order Model (ROM). There are two main decomposition algorithms that are most commonly used– namely Proper Orthogonal Decomposition (POD) and Dynamic Mode Decomposition (DMD).

POD is a modal decomposition technique. Modes are extracted based on optimizing the mean square of the field variable being examined. In this scenario the field variable would be the velocity. POD is most commonly used to extract patterns in turbulent flows [62]. In complex spatio-temporal flow fields such as the dataset in this study, POD would extract patterns in space and time [62]. Modes are ranked according to their energy and the most energetic modes are related to large coherent structures that characterise the flow [41], [63]. Coherent structures are dominant features and trends in the original data that exist in a repetitive pattern in the flow field – even if the flow field as a whole does not repeat itself. A coherent structure maintains its shape and size through time [64]. For example, in the current dataset, some coherent structures would include the hub vortices, tip vortices and meandering of the wake. The drawback of using POD is the ranking system used. The modes are ranked in order of decreasing energy, so modes that have low energy (and are therefore ranked lowly) could be ignored. However, they could actually be highly dynamically relevant. This drawback is addressed with DMD.

DMD is a purely data-driven algorithm that does not require any governing equations. It approximates the non-linear dynamics without the use of equations [41]. Instead, it uses the abundance of data collected to reverse-engineer the governing equations. DMD is most commonly used to provide physical insight into a system. The time-resolved data is decomposed into modes. Modes are spatial structures that have characteristic values of frequency and energy and they oscillate and/or grow/decay at the rates given by the corresponding eigenvalues [62]. These modes relate to specific physical properties of the wake and therefore the most important modes are those that correlate strongly to specific physical properties, ensuring that important modes are prioritised.

DMD was chosen because it is able to capture more physical information of the flow field which is important for understanding the factors that influence the wake dynamics and thus the loading on the downstream turbine in the wake.

To create the ROM, the original LES dataset was first rearranged to reduce the size of the 4-dimensional dataset (x, y, z and time) into 2-dimensional matrices that are more suitable and less computationally expensive to work with [41]. The 4-dimensional flow field is shown in Figure 38, where x, y and z refer to the spatial positions and t refers to the time step. Single snapshots of the dataset (X_k) were then generated and contained the velocity field information at different spatial points at single time steps. As highlighted in Figure 38 with the orange and purple borders, matrix X_k contains a concatenation of 2D "slices" of the z-y plane at different x-locations (blue borders). A snapshot matrix (X) was created by arranging these snapshots in sequential columns so that each column contained velocity field data at a single time step.

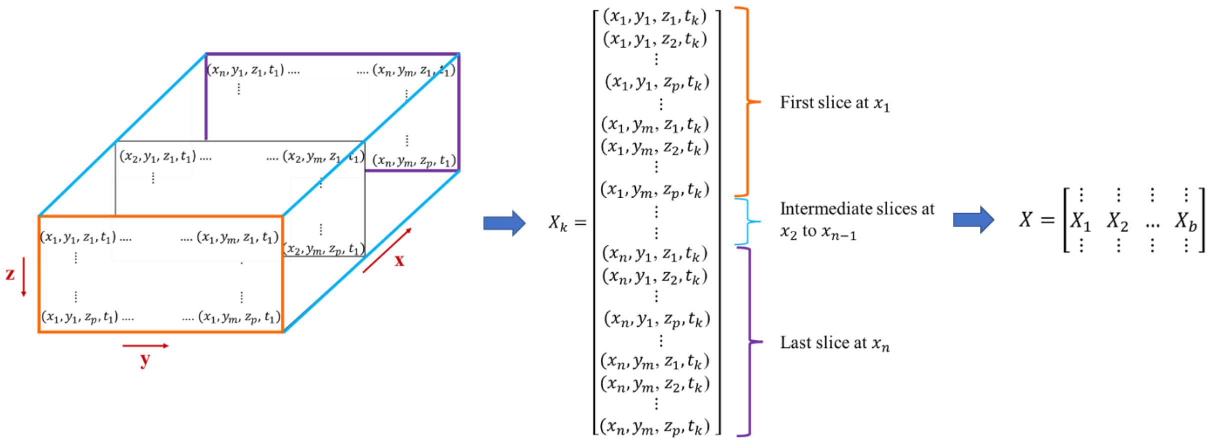

Figure 38. Processing steps of the LES dataset [41]

To work with this snapshot matrix X, its size had to be reduced and an optimal low-rank approximation of the matrix needed to be calculated that would be able to still capture the dynamics of the dataset. This was done through the method of Singular Value Decomposition (SVD). Performing SVD on matrix X decomposes it into left (U), right (V) and diagonal (Σ) singular value matrices [62], as seen in Equation 5. Truncation was then applied to these resulting matrices in order to further reduce the computational resources required. Truncation takes only the first *r* columns (singular values) from each matrix, which will lead to the number of modes generated. A truncation value of 100 was used for this study. Truncation is possible because ranking has already been done so it is certain that the least important columns are discarded first. This resulted in the truncated matrices $\tilde{U}$, $\tilde{V}$ and $\tilde{\Sigma}$ and matrices containing the remaining singular values $\tilde{U}_{rem}$, $\tilde{V}_{rem}$ and $\tilde{\Sigma}_{rem}$. This process resulted in an optimal low-rank approximation of state-space system defined by the number of singular values specified for truncation.

$$X = U\Sigma V = [\tilde{U} \quad \tilde{U}_{rem}] \begin{bmatrix} \tilde{\Sigma} & 0 \\ 0 & \tilde{\Sigma}_{rem} \end{bmatrix} \begin{bmatrix} \tilde{V} \\ \tilde{V}_{rem} \end{bmatrix} = \tilde{U}\tilde{\Sigma}\tilde{V} \tag{5}$$

Validation was then performed by comparing the validation dataset to the identification dataset. The most commonly used measurement to perform this correlation is Variance Accounted For (VAF). VAF is a quantitative measure of how much the model differs from the original data after the operations described above. The equation used to calculate the VAF is shown in Equation 6.

$$VAF_i\big(y_i(k), \hat{y}_i(k)\big) = \left(1 - \frac{\frac{1}{N}\sum_{K=1}^{N}|y_i(k) - \hat{y}_i(k)|^2}{\frac{1}{N}\sum_{K=1}^{N}|y_i(k)|^2}\right) \tag{6}$$

where $y_i(k)$ is the ith output of the model at time step k and $\hat{y}_i(k)$ is the ith output of the original simulation at time step k.

The VAF was plotted for 100 DMD modes and is shown in Figure 39. A higher percentage of VAF indicates a stronger correlation and thus less change from the original data and vice-versa.

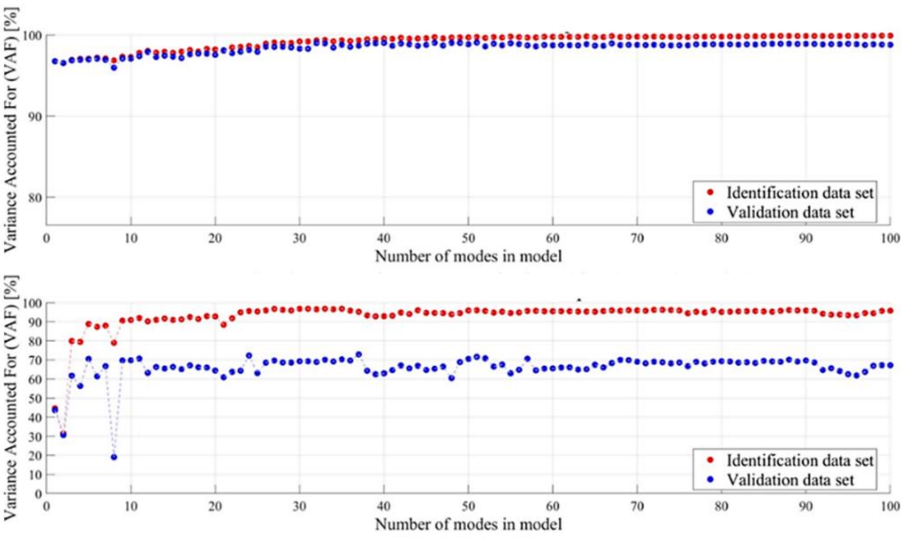

Figure 39. VAF for 100 DMD modes for the identification and validation datasets for the upstream turbine (top) and the downstream turbine (bottom)

Figure 39 shows that the model is much better at predicting the power generated for turbine 1 as opposed to turbine 2. This is because clean, undisturbed air impinges on turbine 1 whereas the turbulent air influenced by the dynamics of the upstream turbine wake impinges on turbine 2, which is further away from the linear function used to predict the trajectory of the power.

The next and final step of DMD is to apply the specific DMD algorithm. Traditional DMD uses the optimal low-rank approximation of state-space system defined in Equation 5 to calculate matrix $\tilde{A}$. $\tilde{A}$ defines the low-dimensional linear model of the dynamical system by projecting the states onto the subspace [41]. It is calculated using Equation 7.

$$\tilde{A} = U^* X' V \Sigma^{-1} \tag{7}$$

where * represents a conjugate transpose, X' is the time-shifted snapshot matrix and Σ^{-1} is the inverse of the sigma matrix from the SVD process.

The reduced order model is given by the following equation:

$$\tilde{x}_{k+1} = \tilde{A}\tilde{x}_k \tag{8}$$

where $\tilde{x}_{k+1}$ represents the projected future state and $\tilde{x}_k$ represents the projected current state.

It was chosen to use Input-Output Dynamic Mode Decomposition (IODMD), which is two steps further than traditional DMD. The first additional step is from DMD to DMDc (Dynamic Mode Decomposition with Control). The DMDc algorithm differs from the DMD algorithm in that the future state (x_{k+1}) is not only dependent on the current state (x_k), but also on a control variable (u_k) [41]. The relationship is given in Equation 9.

$$x_{k+1} = Ax_k + Bu_k \tag{9}$$

where x_{k+1} is the state vector, $u_k$is the input vector and A and B are the state-space matrices.

The second additional step is from DMDc to IODMD. IODMD combines DMD with standard subspace identification, to obtain an input-output characterisation of the system [41]. IODMD is an extension of the DMDc algorithm in that not only are the inputs mapped, but the full-order model is projected onto the output subspace which is also specified by a function [41]. It approximates the original system by a discrete time linear system with both input and output, as described by Equations 10 and 11.

$$x_{k+1} = Ax_k + Bu_k \tag{10}$$

$$y_k = Cx_k + Du_k \tag{11}$$

where x_{k+1} is the future states, x_k is the current state vector, $u_k$is the input vector and A, B, C and D are the state-space matrices.

The output snapshot matrix (Y) is created in the same way that the input snapshot matrix (X) is created in Figure 38. The structure of matrix Y is given below.

$$Y = \begin{bmatrix} \vdots & \vdots & \vdots & \vdots \\ Y_1 & Y_2 & \dots & Y_b \\ \vdots & \vdots & \vdots & \vdots \end{bmatrix} \tag{12}$$

Equations 10 and 11 can be represented in matrix form by the following:

$$X_1 = AX + BU_0 \tag{13}$$

$$Y = CX_0 + DU_0 \tag{14}$$

where x_k is replaced by matrix X, u_k is replaced by matrix U_0, x_{k+1} is replaced by matrix X_1 which has been time-shifted and y_k is replaced by Y.

The equations above are represented in matrix form as follows:

$$\begin{bmatrix} X_1 \\ Y \end{bmatrix} = \begin{bmatrix} A & B \\ C & D \end{bmatrix} \begin{bmatrix} X \\ U_0 \end{bmatrix} \tag{15}$$

The states are then projected onto the sub-space using the matrix Q. Q is a generic orthonormal basis that is used for performing the projection onto the sub-space. A generic low-order representation of the states x_k is given by the following equation where * represents a conjugate transpose.

$$\tilde{x}_k = Q^* x_k \tag{16}$$

Similarly, for each of the state-space matrices:

$$\tilde{A} = Q^* A Q \tag{17}$$

$$\tilde{B} = Q^* B \tag{18}$$

$$\tilde{C} = CQ \tag{19}$$

$$\widetilde{D} = D \tag{20}$$

Therefore, the following equations represent the reduced order model:

$$\tilde{x}_{k+1} = \tilde{A}\tilde{x}_k + \tilde{B}u_k \tag{21}$$

$$y_k = \tilde{C}\tilde{x}_k + \widetilde{D}u_k \tag{22}$$

An approximation of the full order state is given below, where U is the matrix containing the DMD modes and $\tilde{x}_k$ is the reduced order state-space matrix.

$$x_k = U\tilde{x}_k \tag{23}$$

Validation was then performed by processing the validation dataset using the same steps outlined for the identification dataset.

4.2.2 Modal Information

The modal characteristics were generated by using the mode matrix U which was generated from the DMD process in Equation 23. DMD modes are characterised by their frequency, damping ratio, energy contribution and growth rate. By analysing this information about each mode, it can be understood how each mode contributes to the wake shape and dynamics. The aim of analysing each mode is to determine which combination of modes would best capture the wake dynamics and result in the most accurate reconstruction of the flow field using less computational resources as only select features are used. 100 modes were analysed since it is most common to use between 30 to 100 modes [41], [63]. Modes after mode 100 have very low values of frequency and energy and thus provide an insignificant contribution to the flow field. Analysis of this modal information indicated that the modes are mostly ordered from highest to lowest absolute frequency, with the exception of the four mode pairs and four individual modes that have a damping ratio of 1 and thus a frequency of 0. Table 4 shows the modal information for the first 6 modes to be used as a sample reference.

Table 4. Mode information of the first 6 modes

Mode number	**Pole location λ [Real]**	**Pole location λ [Imaginary]**	**Frequency Ω [Hz]**	**Damping Ratio**	**Energy ξ**
1	-0.85	0.47	0.21	0.01	64.77
2	-0.85	-0.47	-0.21	0.01	64.77
3	-0.84	0.02	0.25	0.06	664.28
4	-0.84	-0.02	-0.25	0.06	664.28
5	-0.54	0.82	0.17	0.01	364.35
6	-0.54	-0.82	-0.17	0.01	364.35

The modes exist in eigenvalue pairs, where pairs of modes have the same magnitude of frequency, damping ratio and energy contribution, but exist on either side of the imaginary axis of the complex plane. Figure 40 shows the location of the different modes on the complex plane (left) and the frequency of the different modes with respect to the imaginary axis (right) to illustrate the pairing. The modes circled in purple and blue are used to illustrate the pairing. Based on this observation, the pairs of modes should be used together.

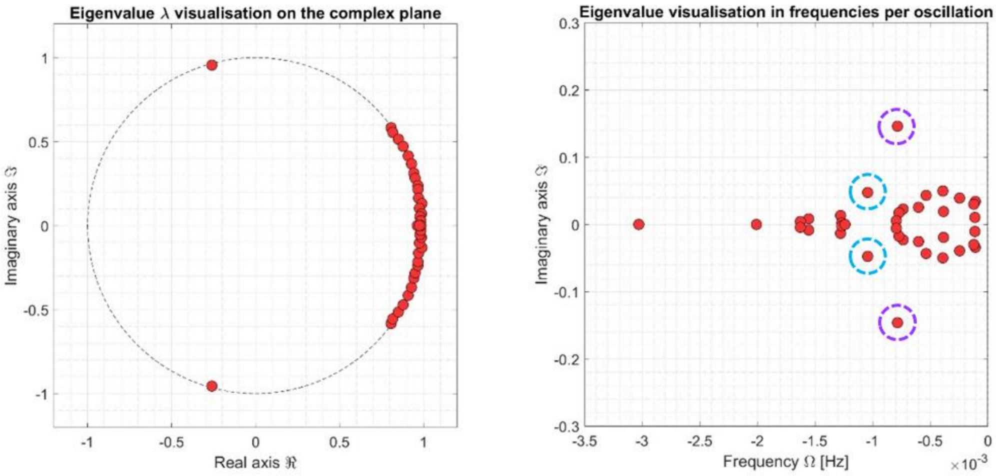

Figure 40. Locations of the different mode pairs on the complex plane [41]

In line with the aim mentioned in section 2.2, the first objective is to identify and group the modes according to the physical property of the wake that they are linked with.

4.2.3 Identification and Grouping of Modes

Identification and grouping of the modes was performed manually through visual inspection. To visualise the modes, the mid-plane of the top view of the mode was plotted to observe the entire span of the wake as it develops downstream. The velocity deficit was plotted using a colour scale to represent the magnitude of the velocity. The velocity scale was adjusted manually to better visualise the features present in the wake. Five physical wake properties have been identified and individual modes that represent each of these were collated into the five different groups as follows:

- Group 1 modes were linked to the mean flow because they capture the steady-state structure of the wake, as highlighted using a red dotted ellipse in Figure 41 – Group 1.
- Group 2 modes were linked to the vortex shedding at the tip of the blade because, as circled in Figure 41 - Group 2, there are sections of positive and negative velocity flow that exist in an oscillating pattern.
- Group 3 modes were linked to the vortex shedding at the tower because the higher velocity flow occurs only at the tower locations, as highlighted in Figure 41 - Group 3.
- Group 4 modes were linked to the wake deflection due to the yawing of the upstream turbine because it is seen from the top view in Figure 41 - Group 4 that there is a distinct deflection of the wake, as highlighted with the red dotted curved line.
- Group 5 modes were linked to the noise of the system because there is a low velocity throughout the entire flow field, as seen in Figure 41 - Group 5.

In Figure 41 the side view and top view is shown for one pair of modes in each group. These views were chosen to conduct the groupings because they capture the entire development of the wake from the upstream turbine to the downstream turbine.

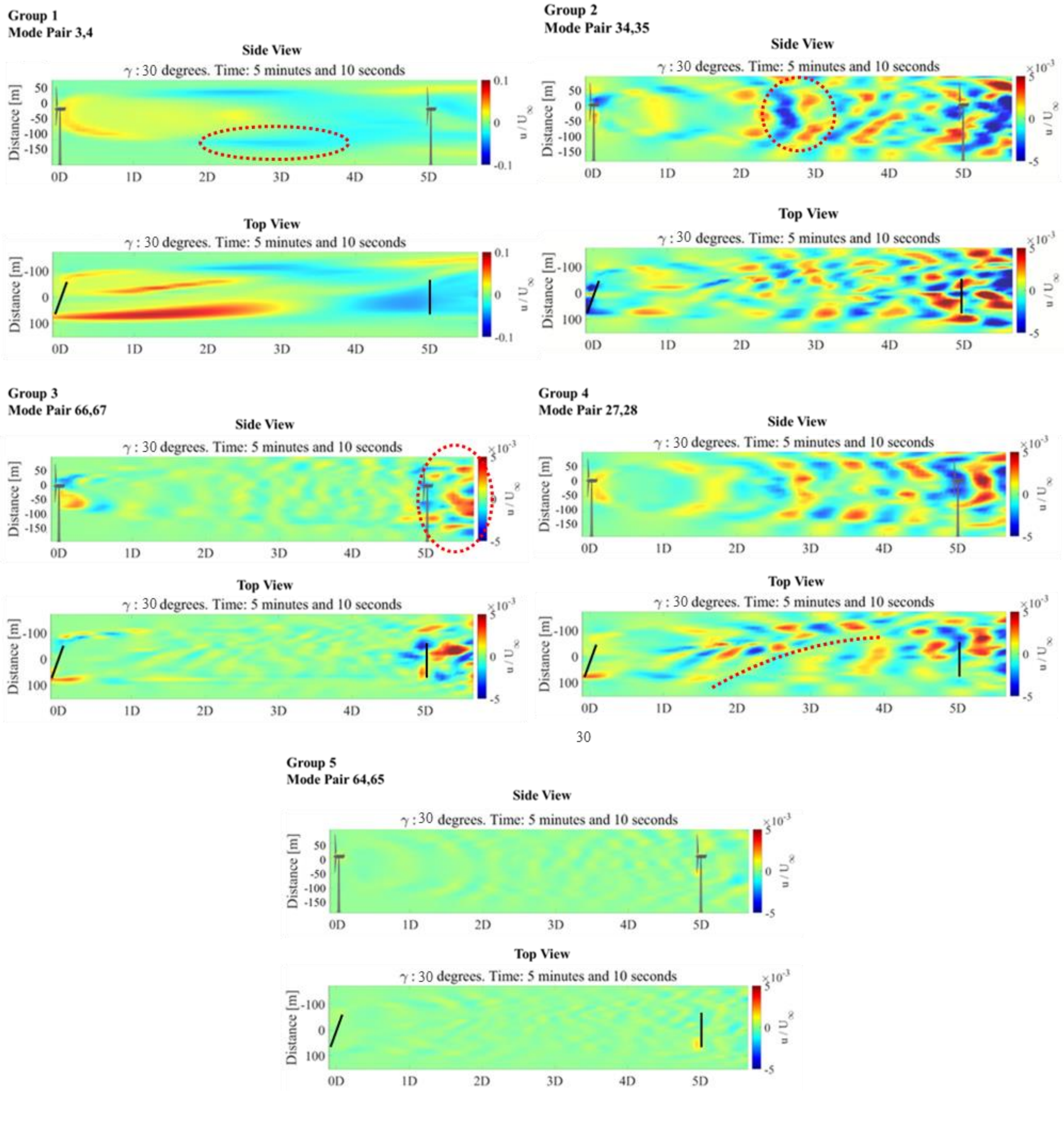

Figure 41. Top view and side view of one pair of modes from each group

Figure 42 presents a collection of some of the pairs of modes from group 4 to show the degree of similarity between different modes from the same group.

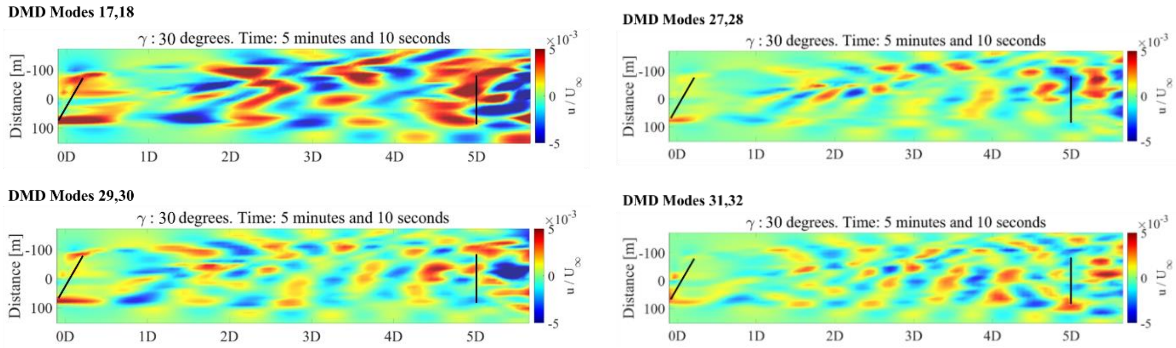

Figure 42. Top view of four pairs of modes from Group 4

However, from the modal characteristics, it was observed that the modes that are linked to the same physical property do not necessarily have similar values of frequency, damping ratio and energy. This observation was investigated further through the use of different machine learning algorithms, with the aim of grouping modes based on a trained model instead of assigning each mode manually to a specific group.

Classification Algorithm

The first algorithm tested was a supervised learning algorithm, which is a subcategory of machine learning. It makes use of labelled datasets that are trained to classify data or make predictions about the data [65]. The input data is fed into the algorithm which adjusts the weighting until the model has been fitted optimally and this fit is then validated. There are two types of supervised learning uses, namely classification and regression. Classification uses an algorithm to accurately place the data into pre-specified categories. It attempts to find patterns within the different categories and then identify characteristics in the data that allow it to be placed into the correct categories. Regression models are used to find patterns between dependent and independent data and are most commonly used for projections or forecasting. The method of classification was chosen for the use of grouping because the aim of using a model is to place different modes into the correct group that all share the same properties.

The classification algorithm was implemented using the Classification App in MATLAB. It was attempted to train the algorithm with the entire 3D transient velocity flow field, but this did not work because the algorithm was making incorrect links between the spatial and temporal points of the flow field. Therefore, the time-averaged velocity was inputted. The highest accuracy achieved with this method was 39.1%. The relationships between the different modal characteristics were then tested to investigate if there was a correlation between these values and the groups they belong to. Figure 43 shows how the different mode groups are spread across the ratios of frequency to energy. Group 3 modes are circled in black to highlight the spread of modes within the same group throughout the different ratios. A similar spread was observed for the ratio of damping ratio to frequency and damping ratio to energy.

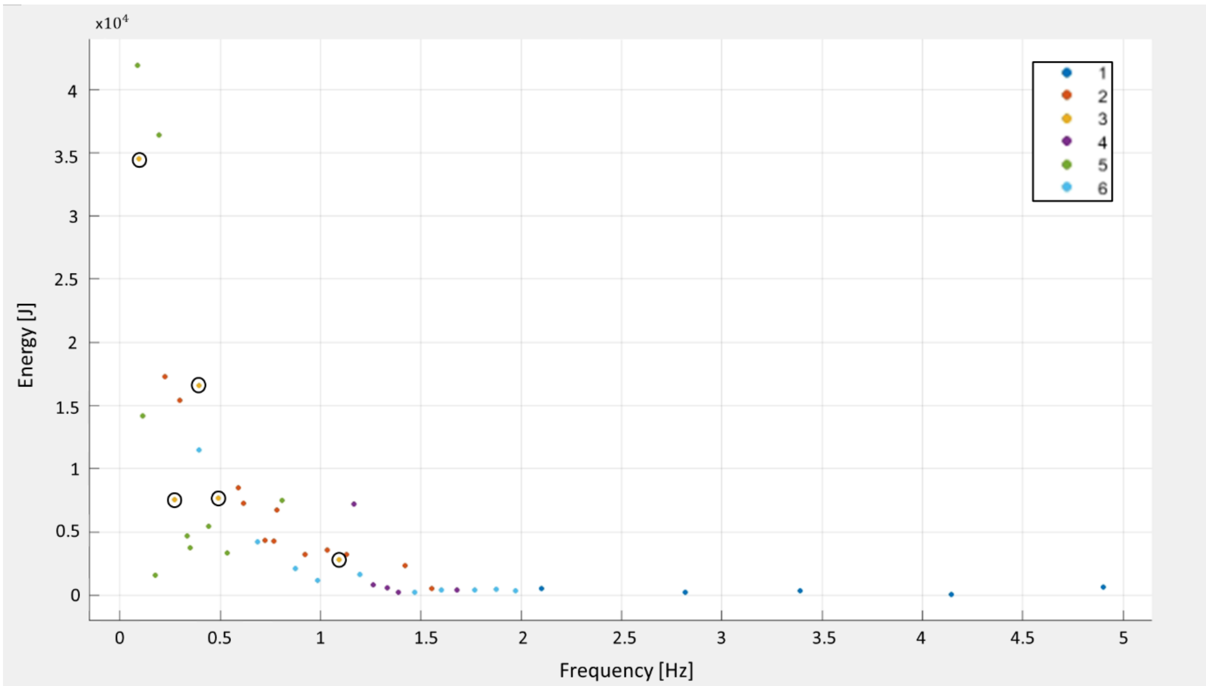

Figure 43. Spread of different mode groups across the different ratios of frequency to energy

K-Nearest Neighbours (KNN) is a method that classifies a new data point based on its proximity to already-classified data points. The k-value determines how many points next to the new data point (neighbours) will be checked. Larger values of k can lead to low variance, because it increases the likelihood of a true classification. However, it can lead to a high bias if the data point is surrounded by many data points from an incorrect group but fewer data points from the correct group that are closer to it [66]. Lower values of k can lead to high variance but low bias. An example of the KNN algorithm is shown in Figure 44. In the example, based on a k-value of 2, the unknown input would be classified as male.

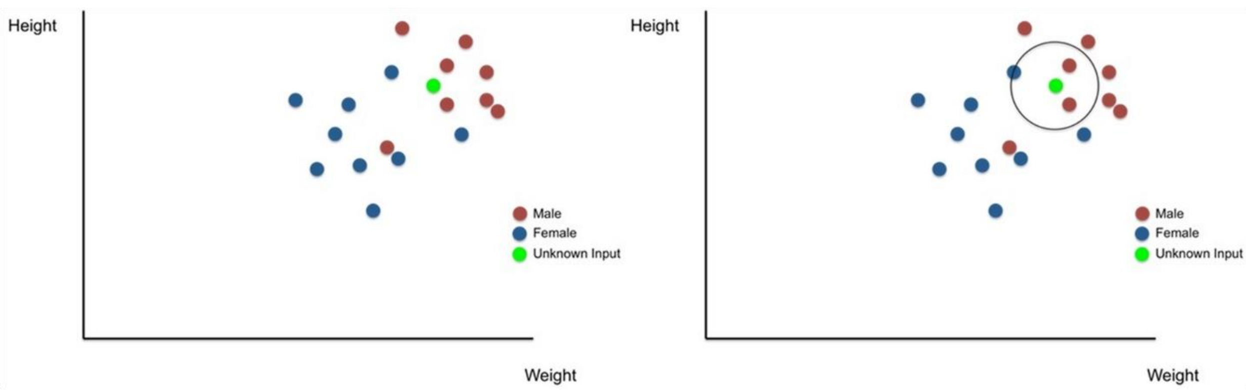

Figure 44. Example of a KNN algorithm [67]

To quantify the ability of an algorithm to group modes based on the different ratios, the modes were grouped using this method of KNN. This resulted in a maximum accuracy of 54.3%, showing that there is a weak link between the modal characteristics and the groups that the modes belong to. Figure 45 shows the confusion matrix of the correctly and incorrectly classified modes and which groups they were classified as.

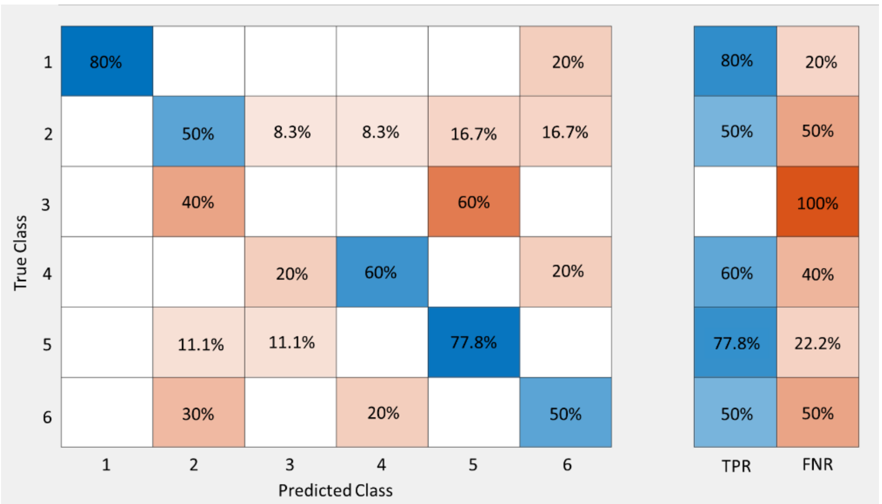

Figure 45. Confusion matrix for the KNN algorithm test

Group 1 modes (mean velocity) and Group 4 modes (yaw) were well clustered, which resulted in these groups having a lower percentage of incorrect predictions. Group 3 modes (tower vertex shedding) are mostly mistaken for Group 5 modes (noise). This is because the higher velocities are only present around the towers in Group 3 and the rest of the flow field is similar to Group 5. Group 6 modes (other) are sometimes mistaken for Group 2 modes (tip vortex shedding). This is because group 6 modes have a similar visual structure to Group 2. One mode from Group 1 (mean velocity) is misclassified because it is near Group 6 modes (other). This misclassified mode has a lower energy value than the other Group 1 modes. Due to the limited accuracy of this method, a second machine learning algorithm was tested to improve the classification process.

Deep Learning Algorithm

The next algorithm tested was a deep learning algorithm. Deep learning networks are also a subcategory of machine learning that attempts to mimic how the brain works. They consist of multiple layers, each having nodes. Each node has a specified weight and threshold (or bias). When the output of the node is above the threshold, the node is activated and data is sent to the next layer. Each individual node can be represented as a linear regression model with its own input, bias and output [68]. The more layers there are, the more complexities the model can work with which tends to increase the capability of the model. However, the number of layers needs to be compatible with the size of the dataset to prevent overfitting to the training data. The general structure of a neural network is shown in Figure 46.

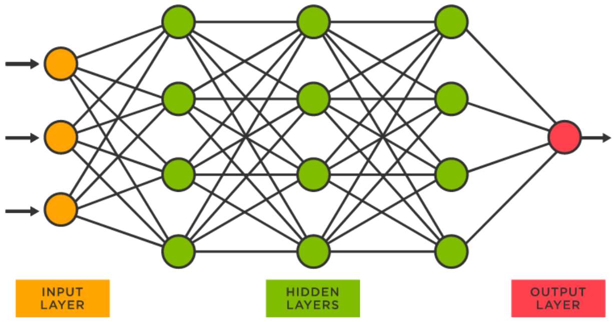

Figure 46. General structure of a neural network [69]

This algorithm was implemented using the Deep Network Designer in MATLAB. This network uses a pre-designed network with input layers, convolution layers, fully connected layers, pooling layers and other layers, connected in series and parallel. The input training data was the images of a sample of the modes and the corresponding group number that they belonged to. Figure 47 illustrates the training method for this algorithm. The training options such as the learning rate, validation frequency and minimum batch size were optimised based on trial and error to achieve a suitable upwards curve in accuracy, seen in Figure 48. The training process resulted in a validation accuracy of 67% which is much higher than the previous method tested.

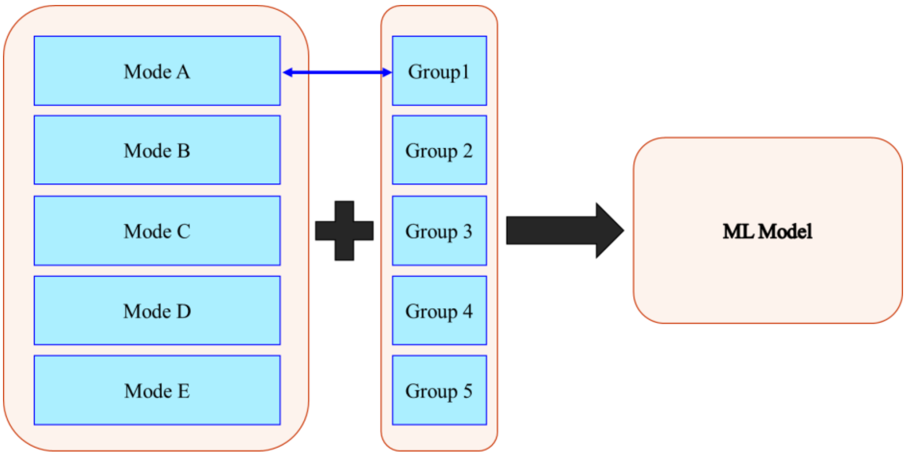

Figure 47. Training input for the Deep Neural Network

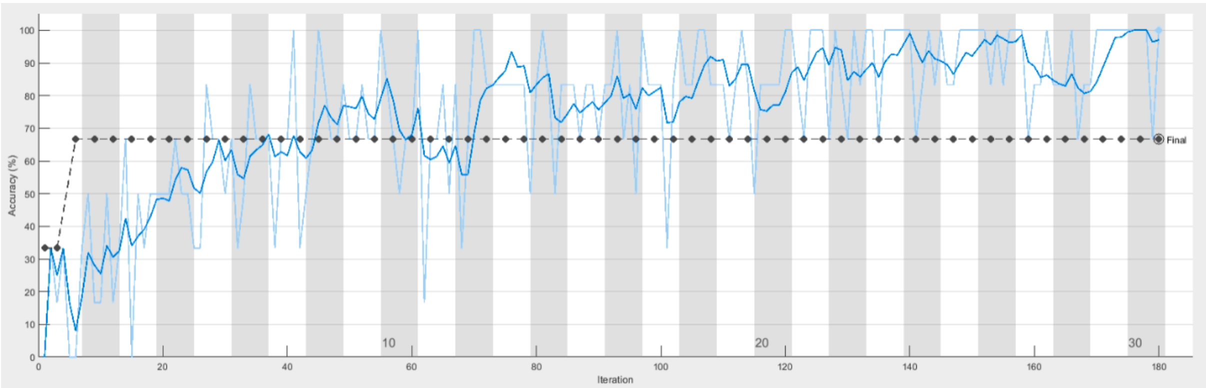

Figure 48. Deep Neural Network training curve

Five mode images (one from each group) were set aside during the training process so that the accuracy of the model could be tested manually. Once the test mode images are fed into the trained algorithm, the algorithm outputs the group to which each of the mode images belongs to. This resulted in an overall classification accuracy of 83%. All modes were classified correctly, except for the mode belonging to Group 3 which was classified as part of Group 2. This can be explained by the lack of training data for Group 3 as three images were used (compared to the other groups which had four to ten training points). This is a limitation of the amount of training data and it is expected that the accuracy of this method can increase further should a larger number of modes be used. Thus, this method and its ability to correctly group five out of six modes proves that a ML algorithm can be used to correctly group the modes. However, since only 100 modes were used in this study, the groupings were conducted by visual inspection to reduce the error margin.

After grouping, the flow field was then reconstructed using each group of modes separately. This was done to estimate which groups would be most useful to feed into the ML algorithm for prediction. It is hypothesized that the same groups that result in the most accurate reconstructions will also result in the most accurate predictions.

Figure 49 shows that Group 1 reconstructs the flow field very accurately and it has an average error of 6.39%. Reconstructions of Groups 2, 3, 4 and 5 do not individually capture the full flow field well, with all these reconstructions having an average error of 100%. Although the combination of all the modes within a group reconstruct the flow much better than any singular pair, these mode groups alone are not enough to capture the flow field sufficiently. From these tests it is observed that it is important to have modes that can capture the mean flow, since the wind turbines are in a pseudo steady state at this time step and are not yawing continuously.

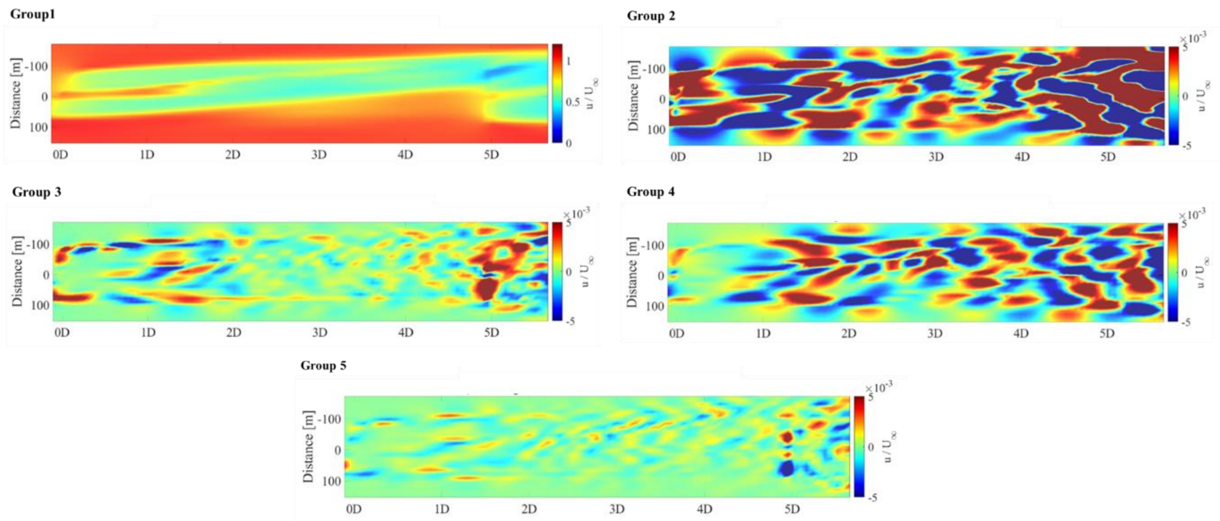

Figure 49. Reconstructions of the flow field using individual mode groups

The flow field was then reconstructed using different combinations of groups to see which combination would result in the most accurate reconstruction. A total of 37 different combinations were tested. Table 5 describes the groups or combination of groups that the different test case numbers refer to. This is followed by Figure 50 showing the Root Mean Square Error (RMSE) and the number of modes used for the reconstruction for different test cases. It is useful to keep track of the number of modes used because this is directly related to the computational resource requirement. Fewer modes will require computational resources.

Table 5. List of test cases and their corresponding groups or combinations of groups

Test Case	**Group/Combination of Groups**	**Test Case**	**Group/Combination of Groups**
1	1	20	1,2,5
2	2	21	1,3,4
3	3	22	1,3,5
4	4	23	1,4,5
5	5	24	2,3,4
6	6	25	2,3,5
7	1,2	26	2,4,5
8	2,1	27	3,4,5
9	1,3	28	1,2,3,4
10	1,4	29	1,2,3,5
11	1,5	30	1,2,4,5
12	2,3	31	1,3,4,5
13	2,4	32	2,3,4,5
14	2,5	33	1,2,3,4,5
15	3,4	34	1-100
16	3,5	35	1,11,12
17	4,5	36	1, damped modes
18	1,2,3	37	Damped modes
19	1,2,4		

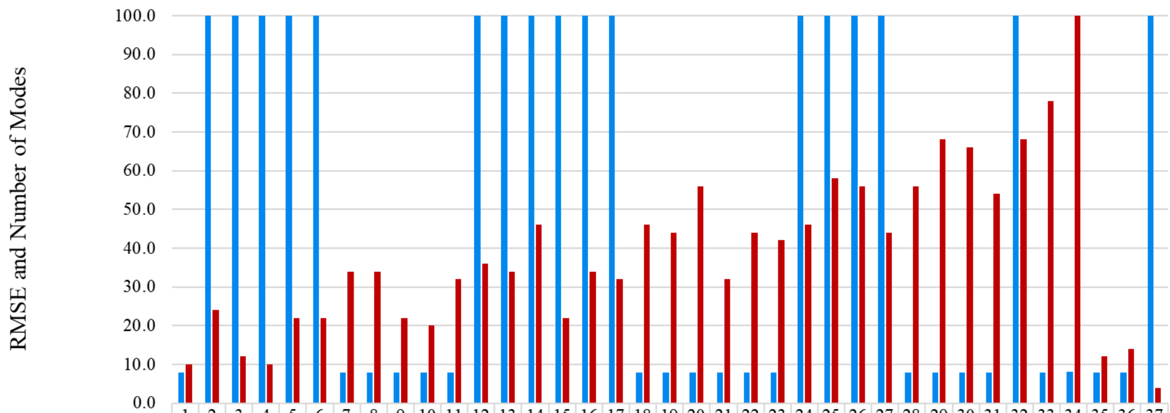

	1	2	3	4	5	6	7	8	9	10	11	12	13	14	15	16	17	18
Average RMSE	7.8	100	100	100	100	100	7.9	7.9	7.8	7.9	7.8	100	100	100	100	100	100	7.9
Number of Modes	10	24	12	10	22	22	34	34	22	20	32	36	34	46	22	34	32	46

	19	20	21	22	23	24	25	26	27	28	29	30	31	32	33	34	35	36	37
Average RMSE	7.9	7.9	7.9	7.8	7.9	100	100	100	100	7.9	7.9	7.9	7.9	100	7.9	8.0	7.9	7.8	100
Number of Modes	44	56	32	44	42	46	58	56	44	56	68	66	54	68	78	100	12	14	4

Test case

Average RMSE   Number of Modes

Figure 50. Comparison between the different groups and combination of groups used for reconstructions of the flow field

From Figure 50 it is observed from the length of the lines that Group 1 (Test Case 1) results in the most efficient reconstructions since it has the lowest combined value of RMSE value and number of modes used. Although the number of modes is a result of it coming from one group, it is a useful indication of computational resources required. It has the fourth lowest average RMSE (following Groups 1,3,5; Groups 1,5 and Groups 1,3) and Group 1 makes use of up to a quarter of the modes that the other groups use. This is an important criterion because it means that Group 1 can achieve an accuracy very similar to the other combinations of groups while using much fewer computational resources.

A previous study conducted chose to use the first 37 modes to reconstruct the flow field [41]. The reconstruction had an average absolute error of 6.52%. However, this investigation has shown that individually analysing the modes and specifically choosing certain combinations could result in an increase in accuracy (6.39% absolute error – calculated by taking the difference between the original flow field and the flow field generated with different combinations of modes). Although the increase is small in this particular investigation using this particular dataset, it is expected that the advantages will increase in larger models. This shows that it is important to conduct an analysis on the modes to choose the modes that best capture the flow field, as the first modes are not necessarily the most useful.

4.2.4 Machine Learning Algorithms for Prediction

The next objective was to determine if a ML algorithm can be used to predict the flow field at yaw angles other than those available in the dataset. This would indicate that the surrogate model can be used to analyse the flow at different yaw conditions without the need for running additional LES simulations. This would mean that wind turbine control could occur in real-time at the wind farm. Different ML algorithms were explored and details are provided in the following subsections.

Convoluted Neural Network (CNN)

The first method tested was a Convolutional Neural Network (CNN). A typical CNN consists of three layers – a convolution layer, a pooling layer and a fully-contacted layer. With each layer, the network is able to identify more and more complex features of the image, such as the colours and borders, the shapes and eventually the target object in the image [70]. CNNs are best used for computer vision problems where input is visual data such as images and videos. The advantage of this method is that detection of the flow features would be automatic, possibly allowing for prediction using the flow features identified. However, the disadvantage is that a CNN usually has difficulty processing images that have different orientations or where the target object is in a different place [70]. It is expected this will not be a major disadvantage because the orientation can be kept constant and the target image remains in the same place, only with slight variations as the upstream turbine is yawed. The CNN layers are used to extract features from the images of the flow field at different yaw angles.

Based on the functions that are typically used in a CNN, it was expected this would result in a 1D vector. This vector would then be fed into an LSTM algorithm that outputs another 1D vector at the next timestep. This new 1D vector (at the sequential timestep) would then be fed into a set of transposed convolutional layers to retrieve an output image that represents the predicted flow field at the next timesteps (or yaw angle). The algorithm was implemented using the pre-trained network GoogLeNet in the Deep Neural Network App in MATLAB. The network was trained with input images of the flow field at sequential timesteps. The algorithm outputted the features of the images (such as shapes, edges, objects and patterns) but it was unclear how to use the features to generate an image. This method was not pursued further.

Deep Learning Network

The next method tested was a Deep Learning Network using a sequence-to-sequence architecture. The aim of this method is to take in sequential images and then to predict the next images in the sequence. If the input images are ordered in sequential yaw angle (instead of sequential timesteps), the algorithm is expected to predict the flow field at yaw angles beyond what it is trained on.

An image datastore was created with sequential images of the flow field. To use an input sequence layer, 3D images are required. To use the 2D images generated instead, an image input layer was required, as well as a flattening layer to reshape the data of the image into the required size. However, this combination of layers was not able to be executed as the combination of layers for regression tasks requires a vector, a matrix or a 4D array of numeric responses. This combination of layers and inputting images are not suitable for regression tasks. Also, the only way to predict future yaw angles is to generate a sequence of images until the desired yaw angle - instead of inputting only the yaw angle and having the algorithm output the flow field at that yaw angle. Transient data where the turbines continuously yaw through a range of angles may not always be suitable to obtain. Therefore, this method was not pursued further.

Time-Series Forecasting

The aim of this method is to take in matrices representing the flow field at sequential timesteps and to generate the flow field matrices at successive timesteps. This method is similar to the Deep Learning Network explained above, except matrices are used instead of images.

The input to the training process was a matrix containing multiple columns, where each column represented the velocity flow field at a particular time step, which related to a particular yaw angle. An example of this is illustrated below in Figure 51.

t = 59 s Yaw angle = 0°	t = 60 s Yaw angle = 1°	t = 61 s Yaw angle = 1.2°	t = 62 s Yaw angle = 2.8°	t = 63 s Yaw angle = 3.6°
↑	↑	↑	↑	↑
3D velocity flow field reshaped into one column	3D velocity flow field reshaped into one column	3D velocity flow field reshaped into one column	3D velocity flow field reshaped into one column	3D velocity flow field reshaped into one column
↓	↓	↓	↓	↓

Figure 51. Example of the training input of the Time-Series Forecasting method

The algorithm was trained with four layers – a sequence input layer, an LSTM (Long Short-Term Memory) layer, a fully connected layer and a regression layer. Other training options such as the number of epochs were set based on the size of the dataset. Training resulted in the generation of a variable that represented the trained network. Prediction of future time steps was done by feeding previous time steps into this trained network. This resulted in the generation of a matrix where each column represented the flow field at predicted time steps. However, two observations were made after testing this algorithm. The first was that the yaw angle of the upstream turbine did not match what the corresponding flow field would be at that time. This is because at the transient timesteps as the turbine is rotating from a yaw angle of 10° to 30° and back, the flow is not given enough time to catch up to the yaw angle of the upstream turbine. For example, the upstream turbine rotates from 10° to 30° in a time span of 71 seconds as it rotates through several intermediate recorded angles. However, it only remains at each of these intermediate angles for a maximum of two seconds. This is not enough time for the flow to develop downstream before the yaw angle is changed again. Therefore, using the intermediate yaw angles gives an incorrect representation of the flow field. For example, Figure 52 shows two instances of the flow field when the yaw angle is at 23.2°. In the top image the turbine is yawing from 10° and therefore it looks very similar to the wake at 10°. In the bottom image the turbine is yawing from 30° and therefore it looks very similar to the wake at 30°. Both images are most likely incorrect representations of the flow field at 23.2°.

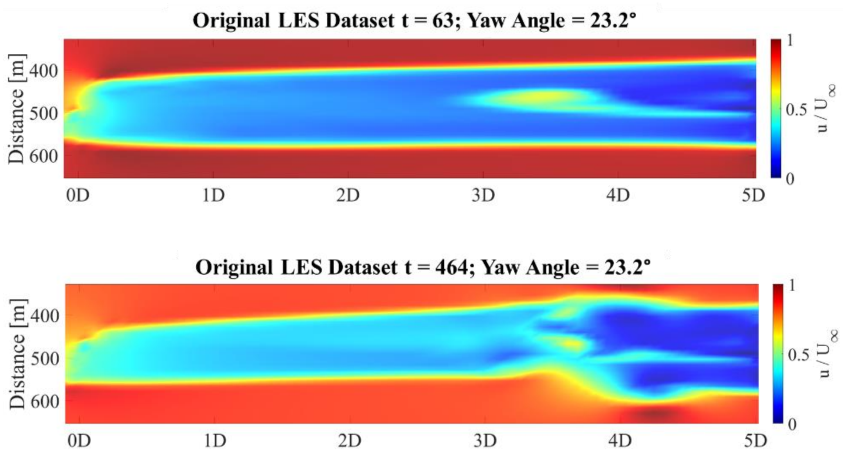

Figure 52. Comparison between two different instances of the flow field at 23.2°

Therefore, only yaw angles 10° and 30° can be used as the turbines remain at these angles for a sufficient amount of time (approximately 150 seconds). The second observation was that it cannot be determined at what angle the flow field is at for the predicted time steps. This is because at sequential timesteps the yaw angles are not evenly spaced. In the example used above, the prediction will be of the flow field at t = 64s, but since one timestep does not represent a constant difference in yaw angle, it will not be known what yaw angle it is predicting. Therefore, this method was not pursued further.

Neural Network Fitting (NNF)

The fourth method tested was an NNF model. The aim is to take in different yaw angles and their corresponding flow fields, and after training it would be possible to input a yaw angle and have the algorithm return the corresponding flow field matrix for that specific yaw angle. The yaw angle will be treated as the dependent variable because its change causes the change in the flow field whereas all other variables in the LES simulation remain the same.

This method was implemented using the Neural Network Fitting App in MATLAB. This model requires two input variables, namely a Predictor variable and a Response variable. The Predictor variable is similar to an independent variable and the Response variable is similar to a dependent variable. The columns of the Response variable correspond to the columns of the Predictor variable. In this scenario, the columns of the Predictor variable contain the yaw angles of the upstream turbine and the columns of the Response variable contain the flow field at each corresponding yaw angle. An example of the input is shown in Figure 53.

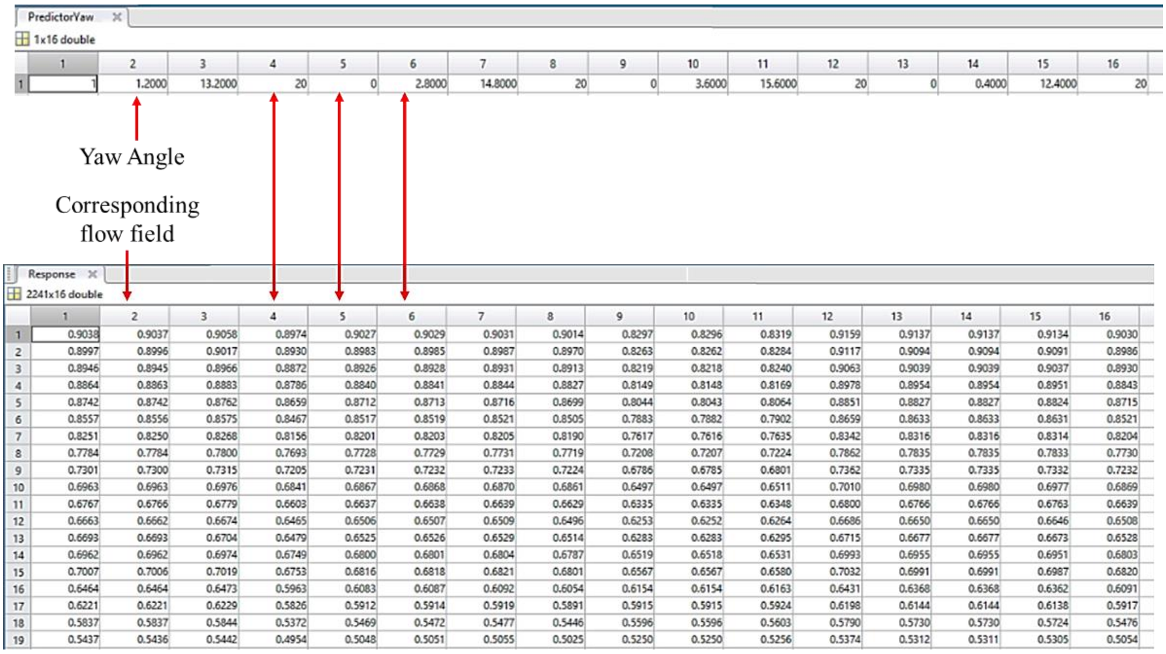

	1	2	3	4	5	6	7	8	9	10	11	12	13	14	15	16
1	1	1.2000	13.2000	20	0	2.8000	14.8000	20	0	3.6000	15.6000	20	0	0.4000	12.4000	20

	1	2	3	4	5	6	7	8	9	10	11	12	13	14	15	16
1	0.9038	0.9037	0.9058	0.8974	0.9027	0.9029	0.9031	0.9014	0.8297	0.8296	0.8319	0.9159	0.9137	0.9137	0.9134	0.9030
2	0.8997	0.8996	0.9017	0.8930	0.8983	0.8985	0.8987	0.8970	0.8263	0.8262	0.8284	0.9117	0.9094	0.9094	0.9091	0.8986
3	0.8946	0.8945	0.8966	0.8872	0.8926	0.8928	0.8931	0.8913	0.8219	0.8218	0.8240	0.9063	0.9039	0.9039	0.9037	0.8930
4	0.8864	0.8863	0.8883	0.8786	0.8840	0.8841	0.8844	0.8827	0.8149	0.8148	0.8169	0.8978	0.8954	0.8954	0.8951	0.8843
5	0.8742	0.8742	0.8762	0.8659	0.8712	0.8713	0.8716	0.8699	0.8044	0.8043	0.8064	0.8851	0.8827	0.8827	0.8824	0.8715
6	0.8557	0.8556	0.8575	0.8467	0.8517	0.8519	0.8521	0.8505	0.7883	0.7882	0.7902	0.8659	0.8633	0.8633	0.8631	0.8521
7	0.8251	0.8250	0.8268	0.8156	0.8201	0.8203	0.8205	0.8190	0.7617	0.7616	0.7635	0.8342	0.8316	0.8316	0.8314	0.8204
8	0.7784	0.7784	0.7800	0.7693	0.7728	0.7729	0.7731	0.7719	0.7208	0.7207	0.7224	0.7862	0.7835	0.7835	0.7833	0.7730
9	0.7301	0.7300	0.7315	0.7205	0.7231	0.7232	0.7233	0.7224	0.6786	0.6785	0.6801	0.7362	0.7335	0.7335	0.7332	0.7232
10	0.6963	0.6963	0.6976	0.6841	0.6867	0.6868	0.6870	0.6861	0.6497	0.6497	0.6511	0.7010	0.6980	0.6980	0.6977	0.6869
11	0.6767	0.6766	0.6779	0.6603	0.6637	0.6638	0.6639	0.6629	0.6335	0.6335	0.6348	0.6800	0.6766	0.6766	0.6763	0.6639
12	0.6663	0.6662	0.6674	0.6465	0.6506	0.6507	0.6509	0.6496	0.6253	0.6252	0.6264	0.6686	0.6650	0.6650	0.6646	0.6508
13	0.6693	0.6693	0.6704	0.6479	0.6525	0.6526	0.6529	0.6514	0.6283	0.6283	0.6295	0.6715	0.6677	0.6677	0.6673	0.6528
14	0.6962	0.6962	0.6974	0.6749	0.6800	0.6801	0.6804	0.6787	0.6519	0.6518	0.6531	0.6993	0.6955	0.6955	0.6951	0.6803
15	0.7007	0.7006	0.7019	0.6753	0.6816	0.6818	0.6821	0.6801	0.6567	0.6567	0.6580	0.7032	0.6991	0.6991	0.6987	0.6820
16	0.6464	0.6464	0.6473	0.5963	0.6083	0.6087	0.6092	0.6054	0.6154	0.6154	0.6163	0.6431	0.6368	0.6368	0.6362	0.6091
17	0.6221	0.6221	0.6229	0.5826	0.5912	0.5914	0.5919	0.5891	0.5915	0.5915	0.5924	0.6198	0.6144	0.6144	0.6138	0.5917
18	0.5837	0.5837	0.5844	0.5372	0.5469	0.5472	0.5477	0.5446	0.5596	0.5596	0.5603	0.5790	0.5730	0.5730	0.5724	0.5476
19	0.5437	0.5436	0.5442	0.4954	0.5048	0.5051	0.5055	0.5025	0.5250	0.5250	0.5256	0.5374	0.5312	0.5311	0.5305	0.5054

Figure 53. Example of the training input of the Neural Network Fitting method

The first attempt was to train the algorithm with the entire 3D flow field at 20 yaw angles (10 instances at 10° and 30° each). This resulted in an input training matrix of 51543 x 20, where 51543 is the 3D velocity flow field for the 20 different instances of the two yaw angles. However, this required 79.2GB of RAM. Through testing it was determined that the number of yaw angles (columns) does not have a significant effect on computational resources required compared to the number of rows. 84 GB of RAM was enabled on the PC but this was also insufficient as training took more than 24 hours to start. Therefore, due to the computational resources required, it was established that the NNF model cannot be trained with the full 3D flow field at one time. To account for this, the flow field was split into 2D "slices" that were fed into the NNF model separately to reduce the computational resource requirement. There were three axes along which the 3D flow field could be sliced – the x, y and z axes. Slicing along the x-axis results in 74 slices of the z-y plane (front view), slicing along the y-axis results in 27 slices of the z-x plane (side view) and slicing along the z-axis results in 23 slices of the y-x plane (top view). To minimise the number of slices required since it is not ideal to train with individual slices of the flow field, it would be best to train with the 23 slices of the top view. The top view is also an important view that captures the entire development of the wake and most of the dynamic properties of the wake. Therefore, each slice (for a single yaw angle) had a matrix of size of 1998 x 1. The NNF model could then be trained with individual slices of the flow field at several instances of yaw angles.

In order to test the extrapolation ability of the algorithm, it was attempted to train the model with flow field inputs at 10° and 25°, so that the prediction at 30°could be compared to the original LES flow field at 30°. However, as established above, the intermediate yaw angles between 10° and 30° cannot be used because it only remains at these yaw angles for two seconds.

Therefore, the model was trained with the flow field when it was steady at only 10° and 30°. A total of 10 timesteps were used for each yaw angle at first to test the general working of the algorithm. 10 layers were used and the training algorithm used was the Levenberg-Marquardt algorithm because these were the default settings. However, the model took 45 minutes to train and the prediction has an average error of 5.19% when compared to the original LES. The output predictions of the flow field at certain yaw angles are given in Figure 54.

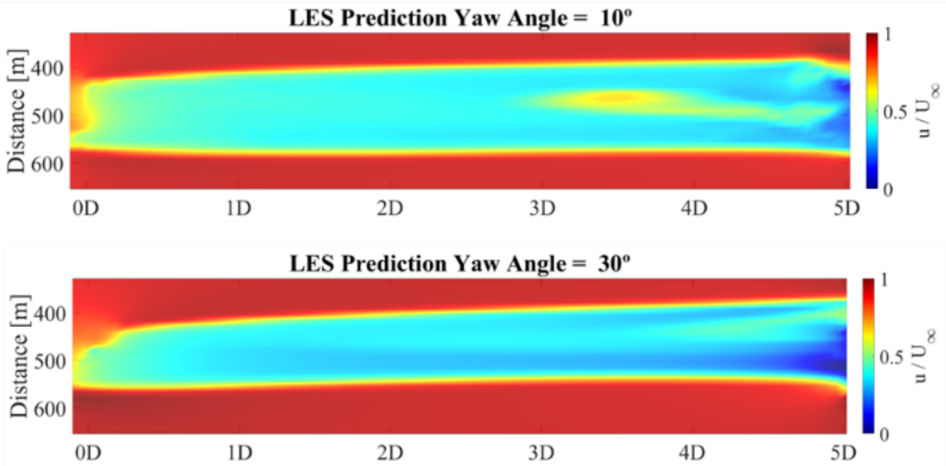

Figure 54. NNF model of LES-trained predictions using default settings

To improve its prediction capability, the workings of the NNF model was analysed in more detail.

The design of the NNF model has, by default, an input layer, an output layer and a minimum of one hidden layer. The example of the network diagram shown in Figure 55 is a model with 1 hidden layer.

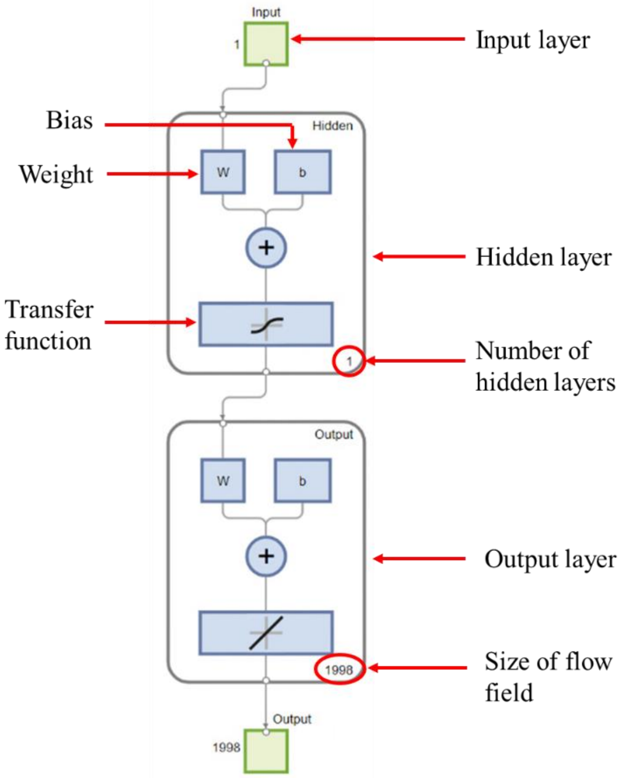

Figure 55. Network diagram for the Neural Network Fitting model

In the Input layer, the maximum and minimum row values are mapped to values within the range [-1 1] because the next layer (Layer 1) contains the tanh function which has asymptotes at -1 and 1. The input layer function takes in a specific yaw angle that a prediction is required for and three constant values – an offset, a gain and a minimum y-value. The input layer returns a processed matrix that corresponds to the velocity flow field at that particular yaw angle.

```
xp1 = mapminmax_apply(x1,x1_step1);
```

Yaw angle outside of training dataset

Consists of 3 constants:
x1_step1.xoffset
x1_step1.gain
x1_step1.ymin

This is then fed into Layer 1, together with a matrix of weights and bias values for the different input yaw angles. The weight matrix is multiplied by the output from the Input layer and it is added to the bias matrix. The neural transfer function, which is equivalent to the tanh function is applied to these inputs to calculate the output of Layer 1, which is another matrix.

Output of Input layer

```
a1 = tansig_apply(repmat(b1,1,Q) + IW1_1*xp1);
```

Bias column vector
10 x 1

Size of predictions required

Weight vector column
10 x 1

In Layer 2, the output of Layer 1 is multiplied with the weight matrix for Layer 2 and the product is added to the bias matrix which is reshaped into the correct size compatible with the weight matrix.

Output of Layer 1

```
a2 = repmat(b2,1,Q) + LW2_1*a1;
```

Bias column vector
1998 x 1

Size of predictions required

Weight matrix
1998 x 10

The output of Layer 2 is then fed into the Output layer which reverses the mapping of the matrix to return to a velocity flow field matrix which is the prediction at a particular yaw angle.

```
y1 = mapminmax_reverse(a2,y1_step1);
```

Output of Layer 2

Consists of 3 constants:
y1_step1.ymin
y1_step1.gain
y1_step1.xoffset

There are two properties of the model that can be changed manually during the training process – the number of hidden layers and the specific type of algorithm that is used. To optimize the functionality of the model, these parameters were tested and the optimal settings were chosen.

It is essential to match the number of layers to the size of the dataset. Having too few layers could result in a loss in accuracy and it is possible that the model will not be trained properly [71]. Having too many layers could unnecessarily increase the complexity and time requirements and could also lead to a loss in accuracy. Compared to other common neural network datasets, this dataset is small in size [38], [72]. Since it is hypothesized that an optimal number of layers for a normal-size dataset is three [71], for this dataset it is hypothesized that not more than two layers will be required. Since the number of layers is dependent on the specific dataset, the best way to determine the optimal number of layers is through experimentation. The size and values of the dataset and the type of algorithm was kept constant for the tests and only the number of layers were changed. The results of the tests are given in Table 6.

Table 6. Average error for different number of hidden layers used

	Number of Layers			
	1	2	10	50
Average error at 10° (%)	6.5898	7.0779	10.3827	18.6981
Average error at 30° (%)	8.0826	8.0364	9.7634	15.1303
Average error (%)	**7.34**	**7.56**	**10.07**	**16.91**

Based on the results given above, it was chosen to use one hidden layer.

There are three different training algorithms to choose from. The Levenberg-Marquardt algorithm is usually the fastest, the Bayesian Regularisation is generally slow but generalizes well to different datasets and the Scaled Conjugate Gradient is memory efficient and is most suitable for low memory situations [73]. Each training algorithm was trained with the same input data and one hidden layer. The results from the training are given in Table 7.

Table 7. Average error for different training algorithms

	Training Algorithm		
	Levenberg-Marquardt	Bayesian Regularization	Scaled Conjugate Gradient
Average error at 10° (%)	6.590	6.437	7.118
Average error at 30° (%)	8.083	8.339	8.184
Average Error (%)	**7.34**	**7.39**	**7.65**

It was found that the Levenberg-Marquardt training algorithm resulted in the lowest overall percentage error. Therefore, this algorithm was used for all future training scenarios.

Training of the model was again conducted with the flow field at 10° and 30° with the new optimized settings as determined above. This resulted in much better predictions of the flow field with an average error of 1.07%. The predictions at a sample of yaw angles are shown in Figure 56. Based on the results of the latest test with the optimized settings, it was decided that this model will be used for all future training.

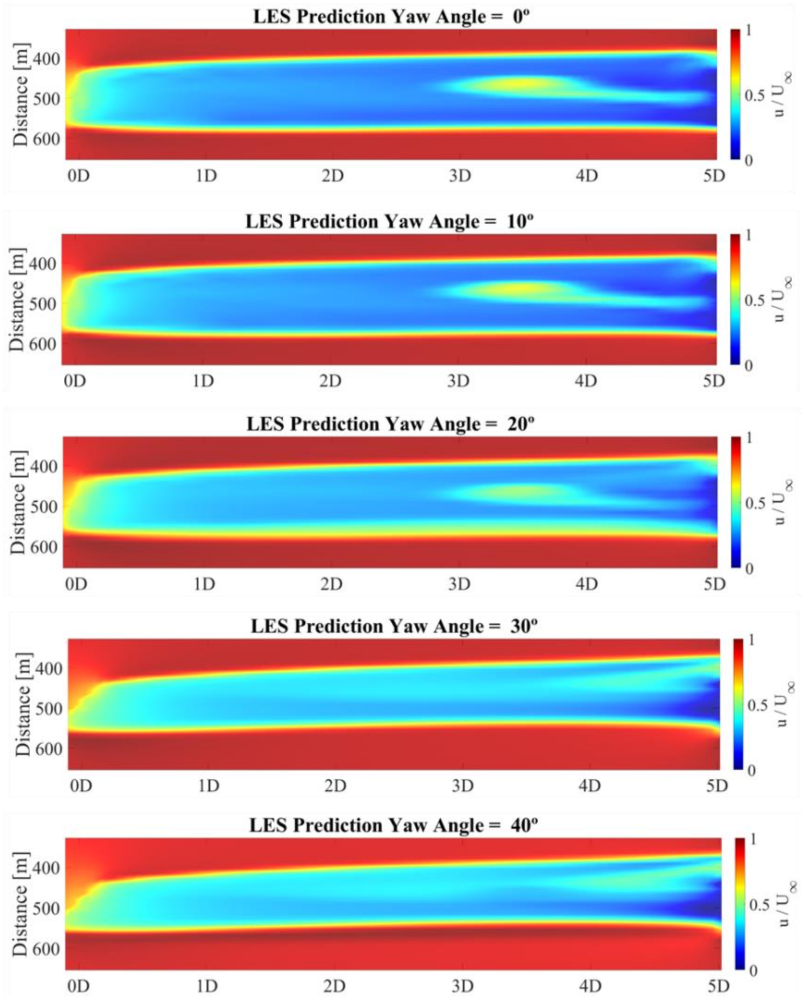

Figure 56. Preliminary predictions of the flow field with optimized NNF model settings

5 RESULTS

5.1 Comparison between the LES Model and the Hot-Wire Anemometer Measurements

The aim of the comparison between the LES model and the hot-wire anemometer measurements was to determine the relationship between the yaw angle of the upstream turbine and the wake deflection to determine the applicability of the dataset and the applicability of the hot-wire measurements to bridge any gaps in the dataset.

There were two features of the experimental setup that differed from the LES model. The first was that the experiments were conducted in a boundary layer wind tunnel, with a boundary layer thickness of 21 cm at the test-section, whereas the LES model had a uniform inflow with no boundary layer. A boundary layer is always present in a wind tunnel and its formation could not be avoided completely to match the conditions of the LES model. However, the differences between having a boundary layer and not having one can be accounted for.

The second feature was that the model wind turbine used to conduct the experiments exhibited the behaviour of a propeller instead of a wind turbine. As explained above in section 4.1.3 – Wind Turbine Model, the model wind turbine was required to be driven by a motor to achieve the same tip-speed ratios as a full-scale wind turbine. However, using a motor means that energy is added to the flow instead of only being extracted by the wind turbine. Therefore, it is expected that certain differences between the LES model results and the hot-wire measurements will be observed. However, the main focus of this comparison was to determine the applicability of the dataset, and therefore these differences are not significant.

The first difference expected is the difference in magnitude of the normalised velocities between the hot-wire measurements and the LES model. Since the experimental wind turbine was driven by a motor, it injected energy into the flow by converting the torque of the shaft to produce axial thrust for propulsion. This resulted in a normalised velocity (U/U_∞) greater than one, as the flow was accelerated to a value higher than the freestream velocity. Comparatively, the LES simulation modelled a full-scale wind turbine that is driven by the wind and therefore extracts energy which resulted in a normalized velocity (U/U_∞) of less than one in the wake region.

It is also expected to observe differences between the two curves in the vertical direction between a position of $z/D = 0$ to $z/D = 0.44$. This is due to the presence of the boundary layer in the hot-wire measurements, which has a normalised height of $z/D = 0.44$. Due to the boundary layer, the hot-wire measurements are expected to have a minimum velocity at the floor that increases exponentially towards the freestream speed at the edge of the boundary layer. In contrast, due to a uniform velocity inflow, the LES model is expected to have a maximum freestream velocity from the floor till the wake region, followed by a maximum velocity above the wake region again (i.e. a uniform velocity all around the wake).

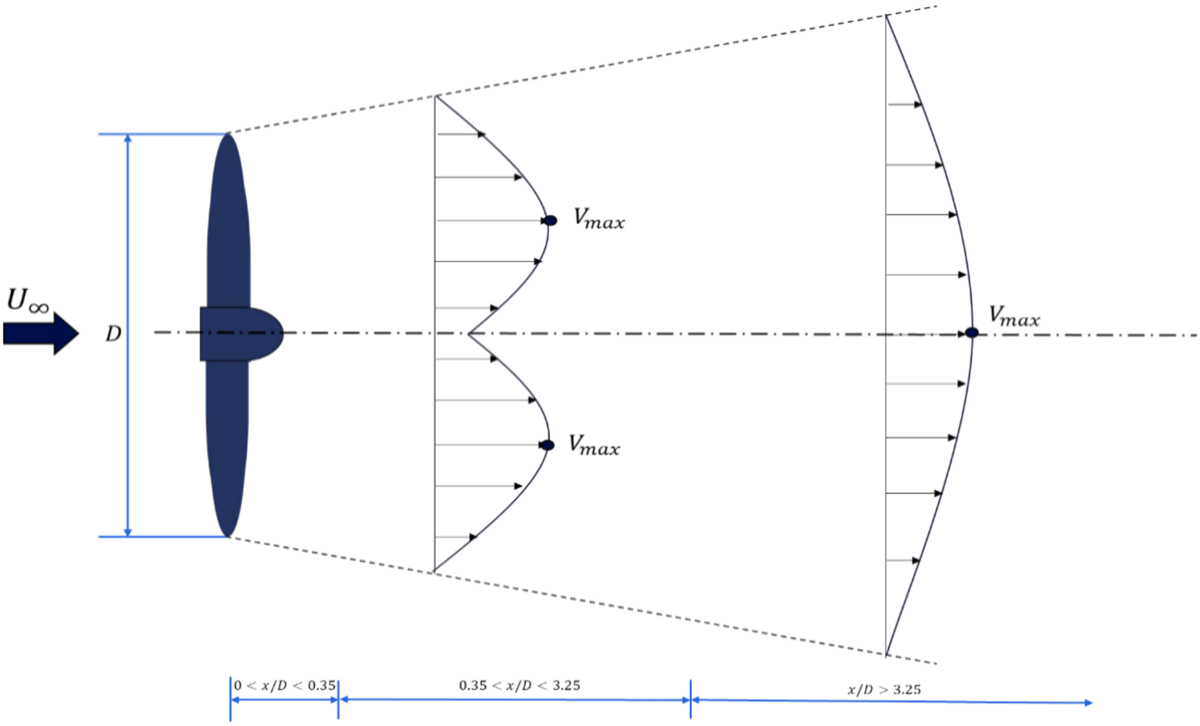

Figure 57. Top view of the velocity profile of the wake at different distances downstream of a propeller [74]

Taking into account the effect of the boundary layer and the model's propeller-like behaviour which is illustrated in Figure 57 and in Stuermer et. al [75], the expected velocity curve at the centre line (at a position of y = 0D) is as follows. It is expected that the flow velocity will be a minimum at the floor and increase towards freestream speed as it approaches the edge of the boundary layer. Above the boundary layer it is expected to have two maximum velocity peaks halfway between the bottom of the rotor and the hub and halfway between the hub and the top of the rotor, as illustrated by the V_{max} positions in Figure 57. However, since one maximum velocity peak lies within the boundary layer, the magnitudes and locations are expected to vary. The magnitudes of the maximum velocity peaks are expected to decrease and their locations are expected to approach the hub height the further downstream the measurements are taken, as seen in Figure 57. There is also expected to be a minimum velocity trough at the hub in the near-field region as no thrust is produced at this location. The further downstream the measurements are taken, the greater the velocity becomes at this hub location until it becomes the single point of maximum velocity, as illustrated in Figure 57.

Taking into account the uniform inflow conditions and the absence of a boundary layer, it is expected that the LES curve at the centre line (y = 0D) is as follows. The curve is expected to be at a maximum at the floor since it is at freestream speed. It is expected to decrease towards a minimum as it approaches the wake region. In the wake region it is expected to observe two peaks of minimum velocity within the rotor area as energy is being extracted from the freestream, resulting in a lower velocity in the wake region, as modelled in Figure 58. At the hub height it is expected for there to be a slight increase in velocity due to the vortex shedding of the hub. The curve is expected to return to a maximum velocity above the wake region as the uniform profile indicates that there is a uniform velocity of freestream magnitude surrounding the wake region. A visual representation of the shape of the expected curve is shown in black in Figure 58. This shape was derived from an analytical model that approximates the wake shape with a three-part function where each part describes a particular dominant component of the wake – namely the main wake (blue), the tip vortices (orange) and the hub jet (green) [76]. The combined equation is shown in Equation 24 [76].

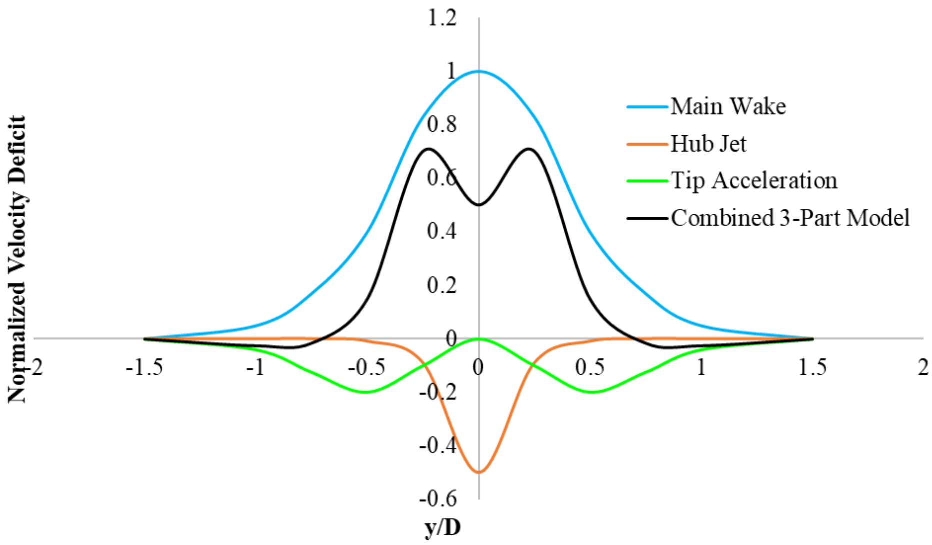

Figure 58. Velocity curves representing the different components of the wake [76]

$$\hat{u} = \boxed{A_m\left(e^{-\left(\frac{r}{2\sigma_m}\right)^2}\right)} - \boxed{A_t\left(\left(\frac{r}{\sigma_m}\right)^2 e^{-\left(\frac{r}{2\sigma_m}\right)^2}\right)} - \boxed{A_h\left(e^{-\left(\frac{r}{2\sigma_h}\right)^2}\right)} \tag{24}$$

The coordinates x, y and z represent the streamwise, spanwise and vertical directions respectively. H represents the hub height and r represents the distance from the wake centre. The half-width of the main wake is represented by σ_m, and the half-width of the hub jet is represented by σ_h and the equations used to describe them are given below.

$$\sigma_m(\tilde{x}) = D(k_m\tilde{x} + \varepsilon_m) \tag{25}$$

$$\sigma_h = D(\varepsilon_h) \tag{26}$$

As mentioned above in section 3 – Description of the Dataset, comparisons will be made with the hot-wire measurements at an upstream turbine yaw of 10° and 30° and a downstream yaw of 10°. A front view of the LES model at 10° and 30° at x = 2.5D and x = 4D are shown in Figure 59 for a visual representation of the LES model curves presented below. The white dashed lines indicate the locations at which the hot-wire measurements were taken (also detailed in Figure 31).

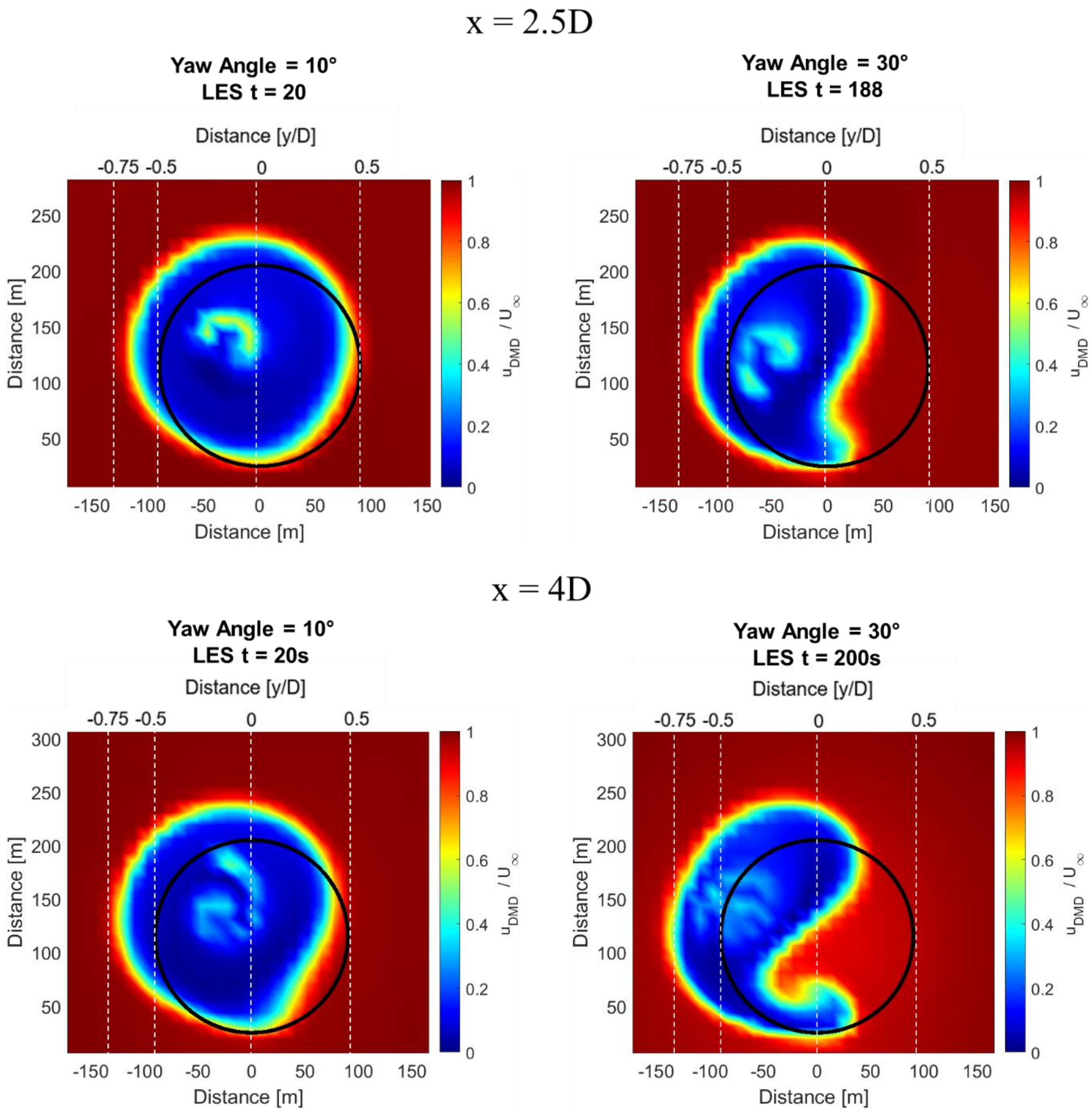

Figure 59. Front view of the wake at x = 2.5D and x = 4D at 10° and 30°

As explained in section 4.1.8, hot-wire measurements were taken at five spanwise and two streamwise locations. The velocity field at these same locations were extracted from the LES model for a comparison. Table 8 shows the tracking of the wake for both the methods. The following key is used:

- No wake: There is no wake present
- Centre: The centre of the wake is present
- Edge: The edge of the wake is present
- Between: A section between the centre and the edge of the wake is present

Table 8. Tracking of the wake from LES and Hot-Wire

y-location	LES	Hot-Wire
Upstream turbine: 10°; Downstream turbine: 0°		
x = 2.5D		
y = -0.75D	No wake	No wake
y = -0.5D	Between	Between
y = 0D	Centre	Centre
y = +0.5D	Edge	No wake
x = 4D		
y = -0.75D	No wake	No wake
y = -0.5D	Between	Between
y = 0D	Centre	Centre
y = +0.5D	Edge	No wake
Upstream turbine: 30°; Downstream turbine: 0°		
x = 2.5D		
y = -0.75D	No wake	No wake
y = -0.5D	Between	Between
y = 0D	Between	Centre
y = +0.5D	No wake	No wake
x = 4D		
y = -0.75D	No wake	No wake
y = -0.5D	Between	Between
y = 0D	Between	Between
y = +0.5D	No wake	No wake

There was generally a good agreement of the wake tracking with the LES and the hot-wire measurements. The hot-wire measurements indicate a greater expansion of the wake as the results at x = 4D show no detection of the centre of the wake as opposed to at x = 2.5D. Both methods indicate deflection of the wake towards the negative side with an increase in yaw angle. As highlighted in red, at x = 4D the centre of the wake is shifted and no longer detected at y = 0D. Based on these results, a definite relationship and quantification of the wake deflection with respect to yaw angle cannot be made at this stage. Smoke measurements will instead be used to quantify the wake deflection (outlined in section 4.1.7). However, these observations show that the LES dataset can be used in this application for training of the surrogate model and in future aspects of the research that involves the yaw misalignment of a two-turbine array. These observations also indicate that the hot-wire measurements could be used to assist in bridging any gaps that exist in the dataset in terms of intermediate yaw angles.

5.2 Smoke Visualisation Measurements

To visualise the change in the wake as the upstream turbine and downstream turbine are yawed, smoke visualisation tests were conducted.

The experiment was set up as outlined in section 4.1.7 – Smoke Visualisation. The wake deflection at the downstream turbine location was analysed since one of the aims of this research is to study the impact of the wake on the downstream turbine. Figure 60 shows the graph of the deflection of the centreline of the wake with respect to the yaw angle of the upstream turbine. A total of five images were analysed at each yaw angle and the standard deviation of the tests were used to calculate the error margins.

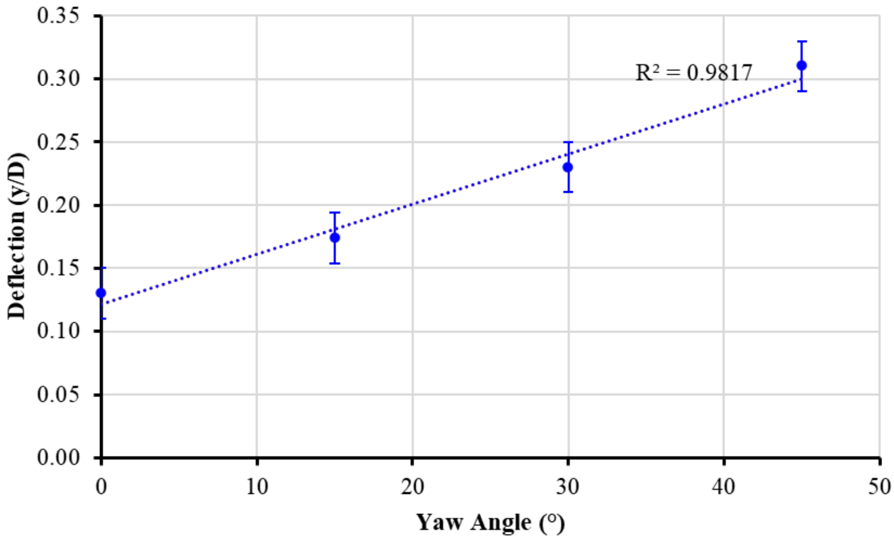

Figure 60. Average deflection of the centre of the wake at different yaw angles of the upstream turbine

The maximum deflection of the centre of the wake was 0.31D at 45°. Figure 60 shows that the larger the yaw angle, the more the wake is deflected. The curve most resembles a straight line, indicating that between 0° to 45°, the wake is deflected by the same amount as the yaw angle increases. This trend correlates to previous studies conducted [31], [77]. Figure 61 shows a collation of the results from previous studies on an upstream turbine at different yaw angles. The curves with triangles indicate values that were calculated based on images presented in the studies. The studies referenced here however did not attempt to describe the trend of wake deflection observed.

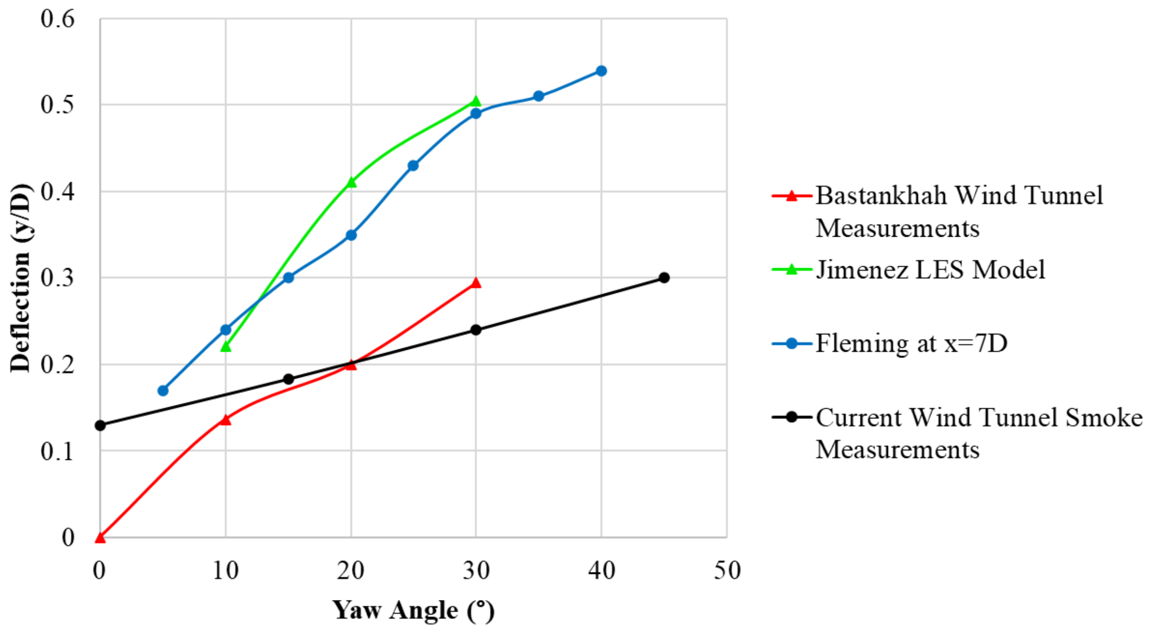

Figure 61. Collation of experimental results from previous studies measuring the deflection of the wake at x = 5D [77], [78], [79]

There is a relatively good correlation of the trends observed between the previous studies and the current study. There is especially a relatively good correlation between the trend and magnitude of deflection between the experiments conducted by Bastankhah, except for the non-zero deflection measured at a yaw angle of 0° in the current study. This difference could be attributed to the presence of a downstream turbine at the location of x = 5D in the current study. The downstream turbine's rotation could cause a minimal increase in deflection of the wake at x = 5D, as it was observed in section 5.2 – Smoke Measurements, that the model turbine causes an acceleration of the wake at the tip of the blades.

Although the trendlines for each curve are inconclusive due to the limited number of yaw angles tested in each, it could be assumed that each correlate strongest to a straight line. This trend makes sense up to a yaw angle of 45°, however it is expected that at a certain yaw angle, the wake will not deflect proportionally and there will be a smaller change in defection as the yaw angle increases. This is expected because the yaw angle will be large enough that it reaches a stall angle. Beyond this, majority of the wake will not even pass through the rotor area and thus the effect that the upstream turbine has on the deflection of the wake will decrease. This maximum yaw angle is expected to be between 45° and 90° because at 90°, the rotor is parallel to the flow and no percentage of the freestream passes through the rotor area.

Using the same method detailed above in section 4.1.7 - Data Acquisition and Processing, the edges of the wake were identified and Figures 62 and 63 were created to visualise the development of the wake downstream and the degree to which it impinges on the downstream turbine. Based on the trendline of the curve in Figure 60, linear interpolation was performed between the four measured angles (0°, 15°, 30° and 45°) to quantify the deflection at three additional intermediate angles (10°, 20° and 40°) since these angles will be compared to the force measurements and hot-wire anemometry measurements conducted at a later stage. The solid dark blue lines represent the edges and centre-line of the wake as it is deflected. The dotted black line represents the middle line between the two turbines and the red and green dashed lines indicate the streamwise positions at which the hot-wire measurements will be taken – for future comparison. The short, coloured lines each represent a distance of 0.1D, to visualise the value of the deflections more clearly.

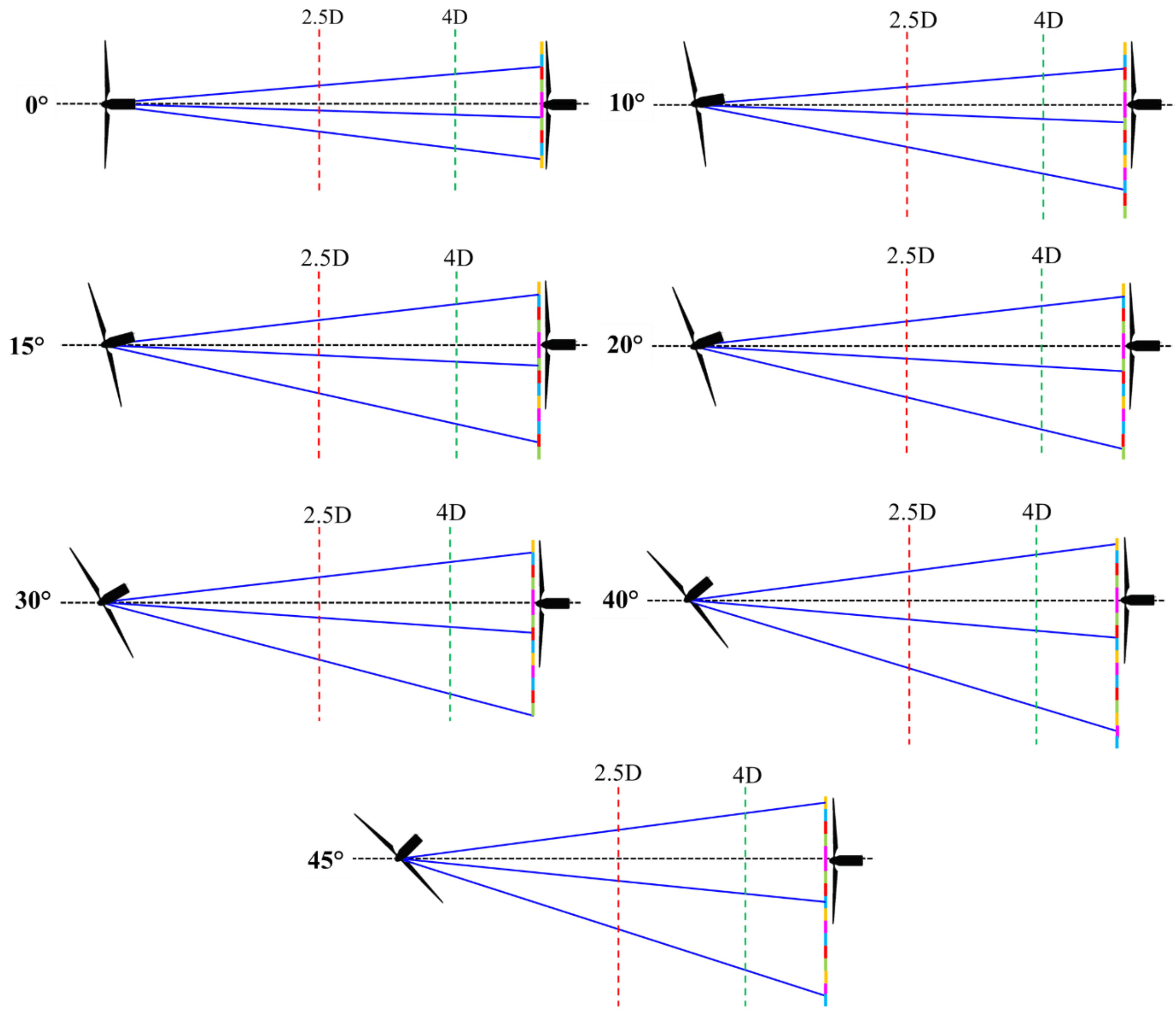

Figure 62. Top view of the wake deflections as observed with the smoke measurements at different yaw angles of the upstream turbine

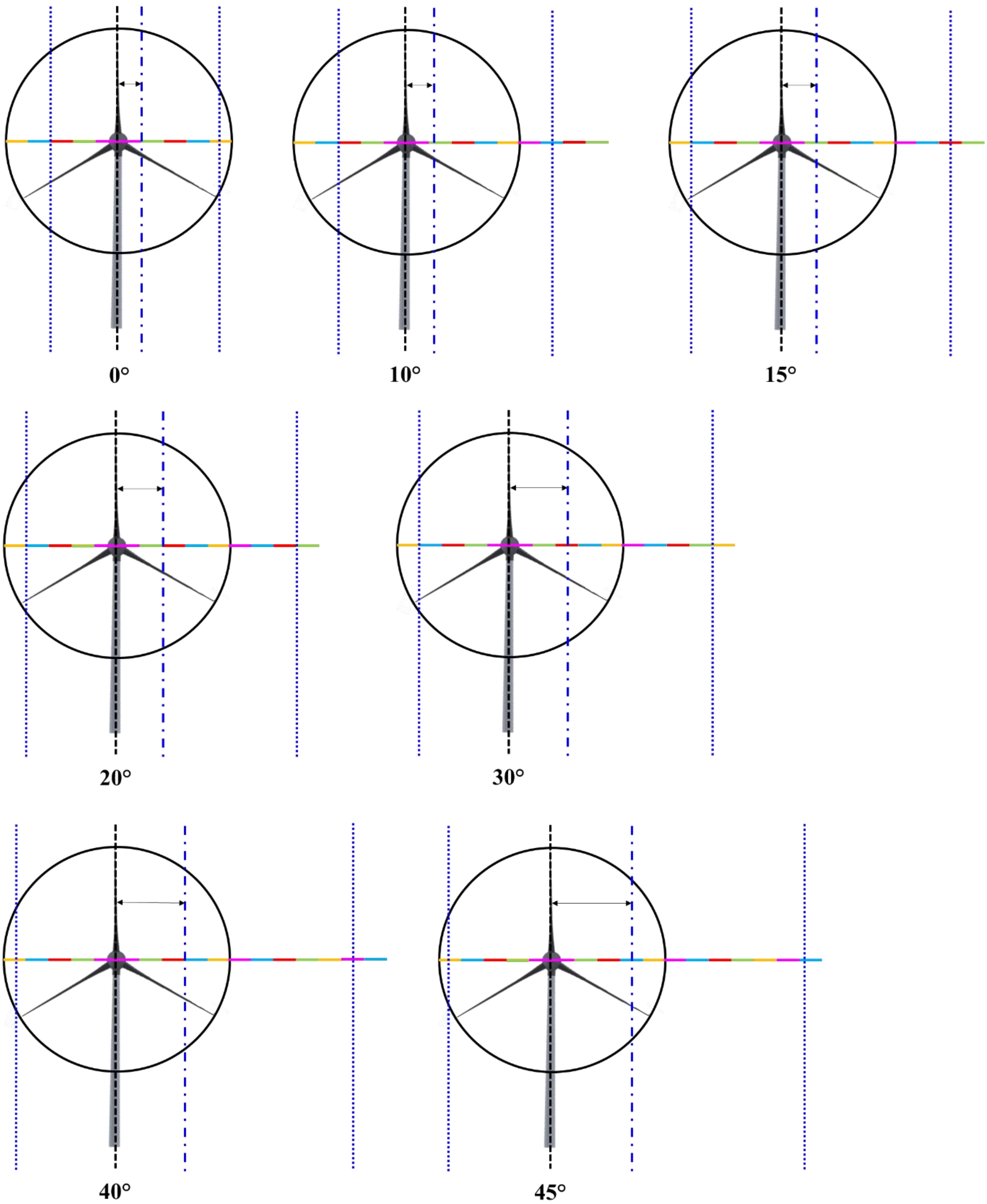

Figure 63. Front view of the wake deflections as observed with the smoke measurements at different yaw angles of the upstream turbine

From Figure 62, the angle of deflection of the centre of the wake was calculated and is shown in Figure 64. The error bars are slightly larger than expected due to the difficulty in accurately defining the edges of the wake visually. These results were compared to the predictions generated from the surrogate model. Based on the deflection of the edges of the wake it was also observed that the wake expands as it develops downstream and the amount of expansion increases with an increase in yaw angle.

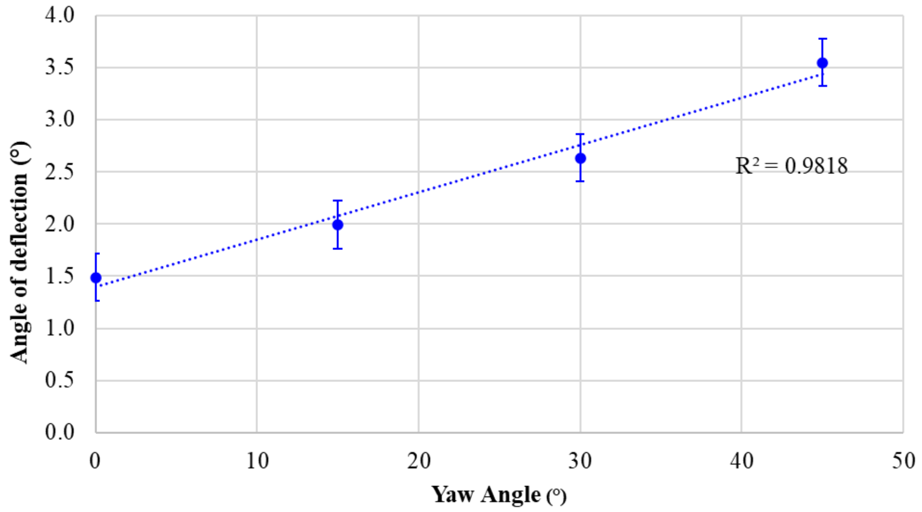

Figure 64. Angle of deflection of the centreline of the wake at different yaw angles of the upstream turbine

As discussed in section 1.2.1 there are certain characteristics that are observed in the wake of a wind turbine such as the rotation of the wake in a helical shape as it develops downstream, the meandering of the wake in the vertical direction as it develops downstream and the shedding of the hub vortices. These characteristics were observed in real-time as the wake developed downstream, however they will not be represented here. There are also characteristics that are observed when the turbine is at non-zero yaw angles, such as the kidney-shaped deflection at large yaw angles (seen in Figure 65), the meandering of the wake in the spanwise direction as it develops downstream (seen in Figure 66) and the deflection of the wake in the spanwise direction (seen in Figure 67).

The kidney-shaped deflection was observed in previous studies and the reason for its formation is detailed in section 1.2.1 – Kidney-Shaped Deflection. The meandering of the wake in the spanwise direction was also observed in previous studies and can be attributed to the strong lateral velocity induced by the counter-rotating vortex pair [78]. The deflection of the wake is attributed to the lateral force that the yawed turbine exerts on the incoming flow which induces a spanwise velocity in the wake [31]. These characteristics are shown in Figures 65 to 67.

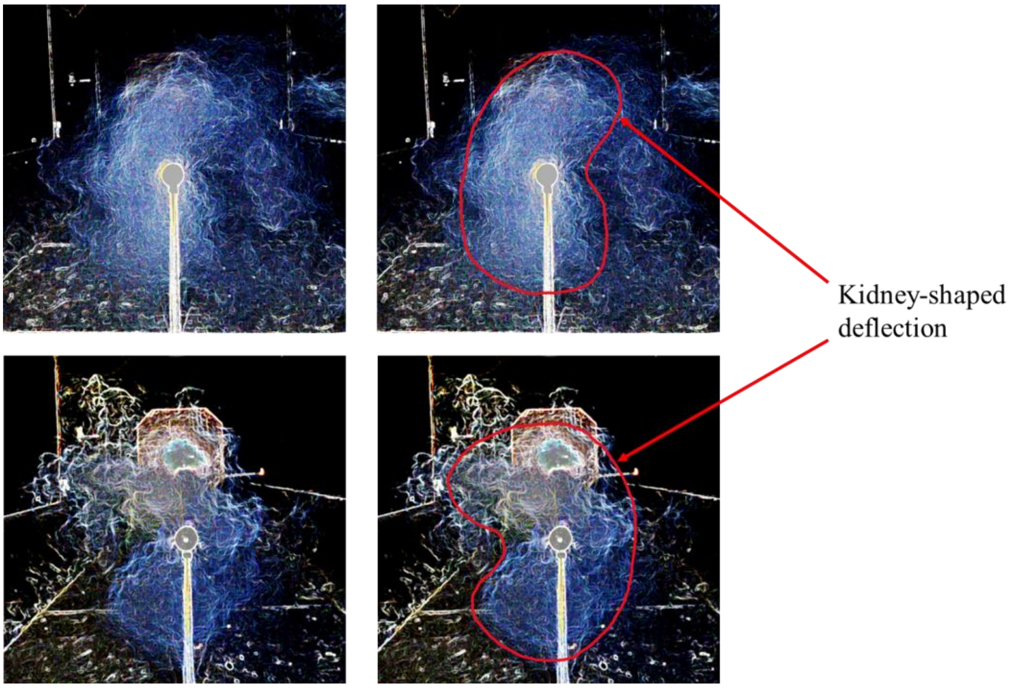

Figure 65. Kidney-shaped deflection of the wake observed with the smoke visualisation at large yaw angles

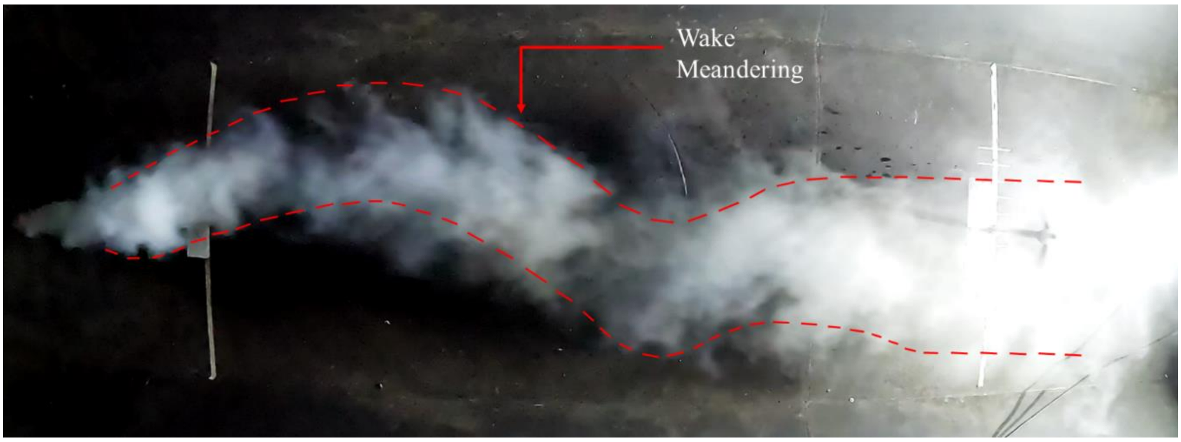

Figure 66. Wake meandering in the spanwise direction – observed with smoke visualisation

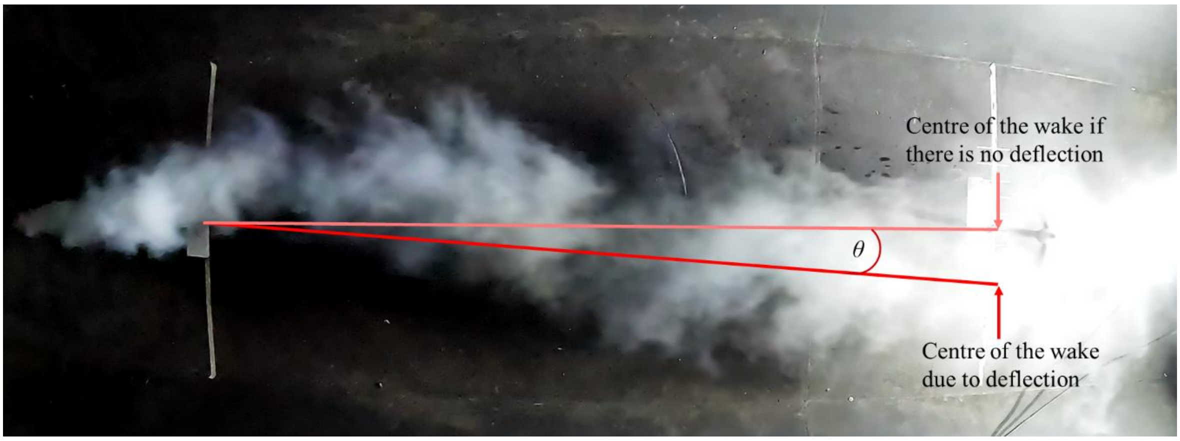

Figure 67. Deflection of the wake at non-zero yaw angles – observed with smoke visualisation

Thus, from the smoke visualisation measurements, the relationship between the wake deflection and the yaw angle follows an approximately linear trendt until 45°. The magnitude of the wake deflection and the expansion was also quantified and compared to previous experimental research conducted on the yaw of an upstream turbine. The smoke visualisation method also allowed the visualisation of additional characteristics of the wake which will be used to better understand the dynamics and structure of the wake.

5.3 Hot-Wire Measurements

The hot-wire results were also used to understand the trends in the wake as the upstream yaw angle was changed from 0° to 40° in increments of 10° and when the downstream turbine is yawed from 0° to 40° in increments of 20°. As detailed in section 4.1.8, hot-wire measurements were taken at five spanwise locations and two streamwise locations. See Figure 31 for a visual representation of these locations. The graphs below use the following key. The solid grey lines indicate the top and bottom of the rotor, the dashed grey line represents the middle of the rotor and the square line indicates the boundary layer. The graphs below only display the curves above the boundary layer because as described above in section 5.1, the flow within the boundary layer behaves differently. The labels 0,0 to 40,0 and 30,0 to 30,40 indicate the angle of the upstream turbine followed by the angle of the downstream turbine.

The first results presented below are the measurements at the streamwise location of x = 2.5D, which is halfway between the two turbines.

From Figure 68(a), it can be seen there is a trend that the larger the yaw angle of the upstream turbine, the lower the velocity of the wake at this location. From the results analysed in section 5.1, it was observed that there are two regions along the centreline of the wake above and below the hub that have a higher velocity compared to the rest of the wake area. As the turbine is yawed, the wake is deflected and thus the centreline of the wake with the regions of high velocity are also deflected – resulting in a lower velocity being measured at the centre of the rotor (y = 0D) at larger yaw angles.

From Figure 68(b) it is observed that as the yaw angle increases from 0° to 20°, the velocity of the flow at this location increases. This could be due to the wake nearing this location as the yaw angle increases. However, since it is still not directly in the wake, the flow is being accelerated by the turbine blade causing the slight increase in velocity. At larger yaw angles of the upstream turbine such as 30° and 40°, the velocity streamline is no longer constant, but has a sinusoidal pattern at this location. This is because the wake has deflected to a large enough degree that this location starts to detect the wake. However, the wake has not been deflected enough such that the centre of the wake is at this location. This can be deducted because the expected propeller pattern seen in Figure 68(a) and described in section 5.1 is not observed. Instead, there is a maximum velocity at hub height followed by a minimum velocity above hub height.

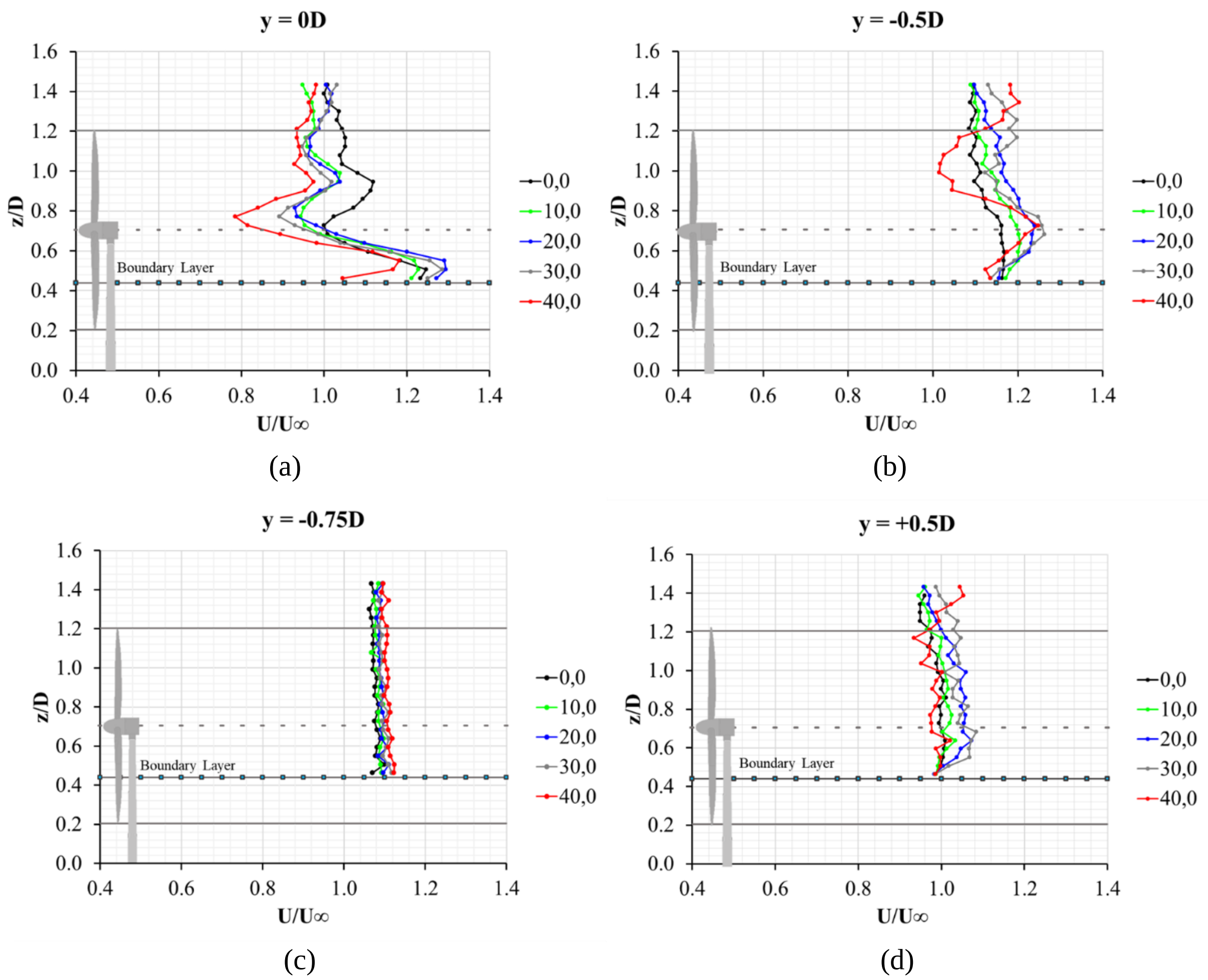

Figure 68. Hot-wire measurements at x = 2.5D at different y-positions, comparing different yaw angles of the upstream turbine

Figure 68(c) shows the measurements taken even further to the left of the turbine at y = -0.75D. It is observed that the velocity streamlines remain constant above the boundary layer, despite the change in yaw angle. This is because the wake does not deflect this far to the right even at large yaw angles and therefore no wake is detected at this location. Therefore, what is observed is the freestream flow that is not influenced by the turbine dynamics.

At the tangent on the right side of the turbine at y = +0.5D, seen in Figure 68(d), the streamlines are mostly constant. This is because these measurements are on the edge of the wake and as the yaw angle increases, the wake is deflected towards the opposite side – away from this location. Therefore, what was observed is mostly the freestream flow. However, the velocity was not as constant as the velocity at y = -0.75D because this location at y = +0.5D is closer to the wake and still partially influenced by the wake as the turbine is yawed.

Measurements were also taken when the upstream turbine was kept at a constant yaw angle of 30° and the downstream turbine was yawed from 0° to 40° in increments of 20°. These tests were performed to investigate if the downstream turbine has an effect on the wake between the two-turbine array. The following graphs were plotted at different spanwise locations.

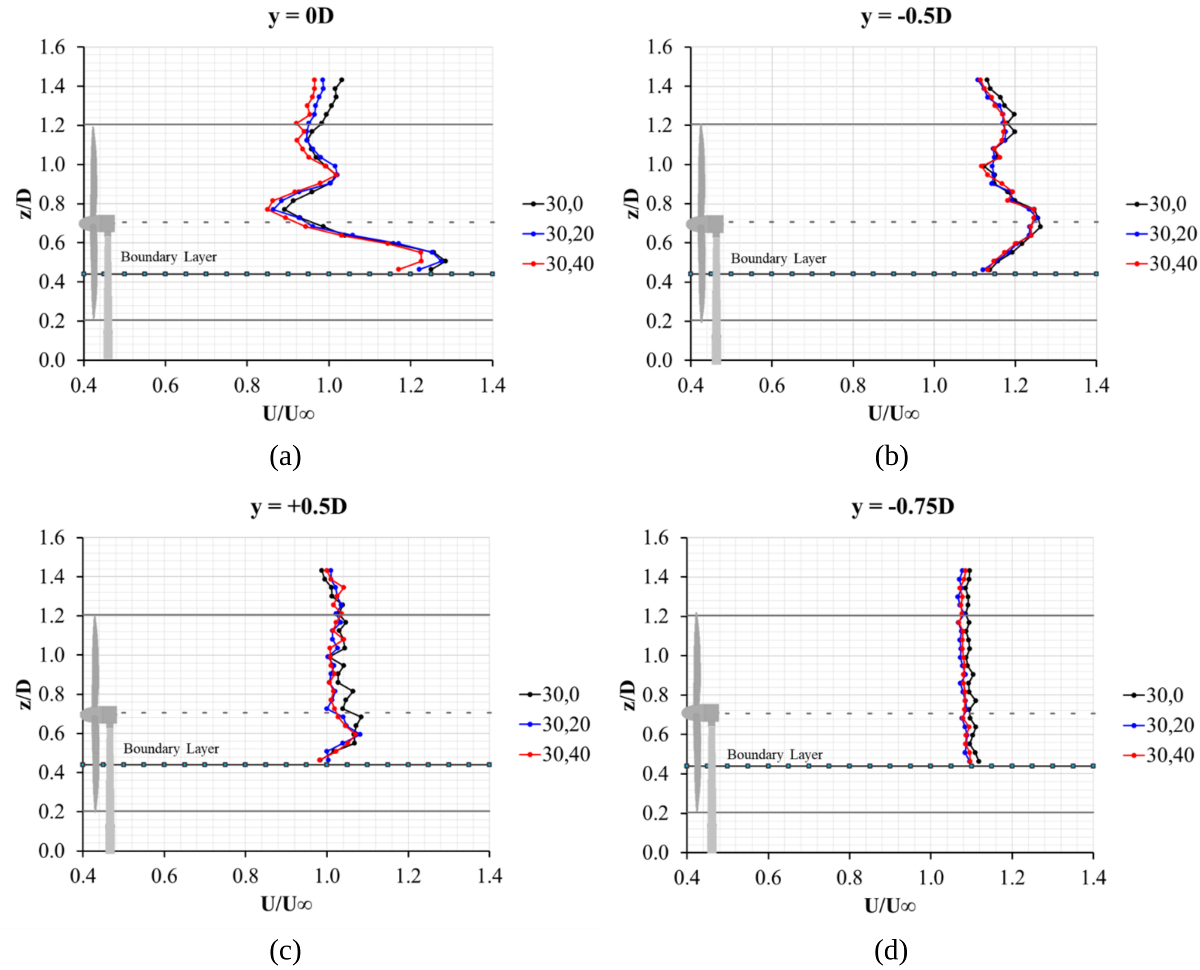

Figure 69. Hot-wire measurements at x = 2.5D at different y-positions, comparing different yaw angles of the downstream turbine

From Figure 69 it is observed that the downstream turbine does not significantly influence the wake between the upstream and downstream. The average ratio between the different angles (30,0:30,20:30,40) at y = 0D is 1:0.98:0.96. At y = -0.5D the ratio is 1:1.02:1.03, at y = -0.75Dis 1:1.02:1.02 and at y = 0.5D the ratio is 1:0.99:1.00. These ratios are very close to one, which indicate how similar the velocities are at each angle of the downstream turbine. This is because only the flow very close to the downstream turbine is being drawn in by the downstream turbine and its rotation is not sufficient to affect the flow far upstream of it.

A comparison was then made between the measurements taken further downstream at x = 4D.

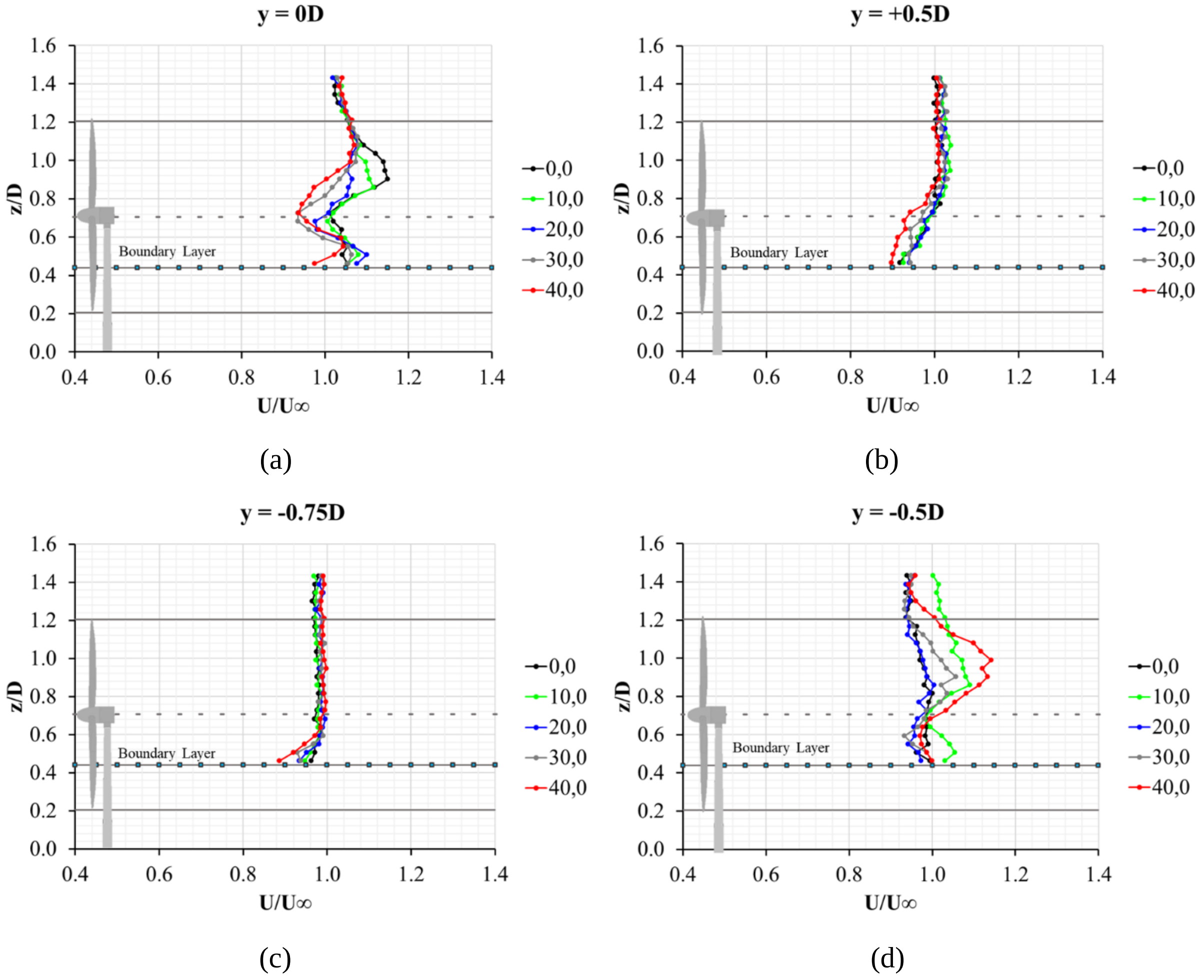

Figure 70. Hot-wire measurements at x = 4D at different y-positions, comparing different yaw angles of the upstream turbine

Similarly to the results at x = 2.5D, at the location of y = 0D, the larger the yaw angle of the upstream turbine, the lower the velocity. However, it was observed that the maximum velocity peak below the hub has a lower velocity compared to the results at x = 2.5D. When propellers are close to the ground, the area in front of the propeller on the ground is influenced by the propeller suction which feeds the vorticity of the ground vortex that forms [80]. This could increase the velocity close to the boundary layer. Also, the presence of the boundary layer could cause the turbulent structures to move towards the ground [81]. However, since it is further downstream, it is hypothesized that the propeller-induced ground vortices have less of an effect on the wake flow and therefore the flow is slower at this location compared to the location further upstream at x = 2.5D.

In Figure 70(b) at y = -0.5D, the velocity is mostly constant at small yaw angles (0° and 10°) of the upstream turbine. From a yaw angle of 20°, the velocity above the hub increases as the yaw angle increases. This indicates that there is greater deflection of the wake at larger yaw angles and therefore only at the larger yaw angles is the wake detected at this location. The wake is detected from a yaw angle of 20° at x = 4D, whereas at 30° at x = 2.5D. This provides evidence of the wake expansion in the streamwise direction and that the deflection of the wake increases the further downstream the measurement is taken.

In Figure 70(c) and 70(d) at y = -0.75D and y = +0.5D respectively, the velocity is mostly constant for all angles as there is no detection of the wake at these locations.

The effect of the yaw of the downstream turbine at x = 4D was also investigated. Similarly to x = 2.5D, the yaw angle of the downstream turbine does not have a great effect on the wake even at the location of x = 4D.

These hot-wire anemometer results show that the deflection of the wake increases as the yaw angle of the upstream turbine increases. This observation correlates with the smoke visualisation measurements (see Figure 60) and the LES simulations (see Figure 56) which both indicated the same result. The hot-wire results also show that the wake expands downstream which results in a greater defection being detected further downstream. This observation also correlates with the smoke visualization measurements (see Figure 62) and the LES simulations (see Figure 59).

However, it was not possible to measure the exact spanwise location that captured the edge of the wake at each angle. This would have required testing each spanwise location from y = -0.5D to y = -0.75D, since the precise location of the edge of the wake could not be predicted. Hence, it cannot be determined from these hot-wire measurements what the exact degree of deflection is and how much the deflection changes with the change in yaw angle. Instead, these hot-wire results will be used to analyse other aspects of the wake such as the velocity profile of the wake for the wind turbine model.

5.4 Combination of Experimental Results

To understand more about the wake dynamics of the flow when an upstream and downstream turbine are at different yaw angles, three sets of experimental tests were combined, namely force tests, smoke visualisation tests and hot-wire anemometer tests. The combination of these results and the overall conclusions drawn from the experimental observations are presented below.

Each force exerted on the downstream turbine will be analysed separately. The conventions used for the forces and moments are shown in Figure 33, but is shown again here for convenience in Figure 71. The red dot in the figure indicates the point at which the calibration measurements were taken and therefore where forces and moments are measured. This location will be referred to as the measurement location from here onwards.

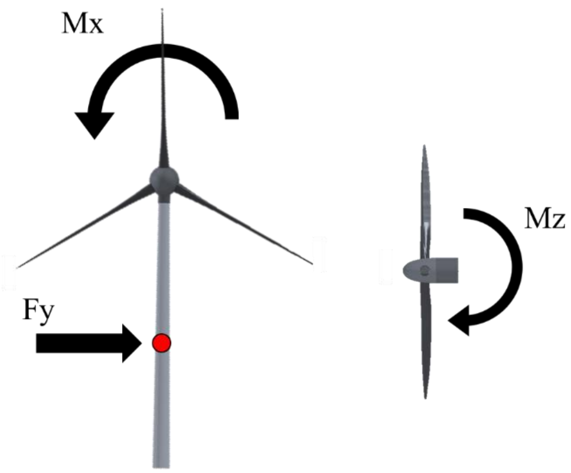

Figure 71. Conventional directions used for force and moment measurements

Figure 72 shows the graph of the yaw angle of the upstream turbine versus the force exerted in the y-direction on the downstream turbine.

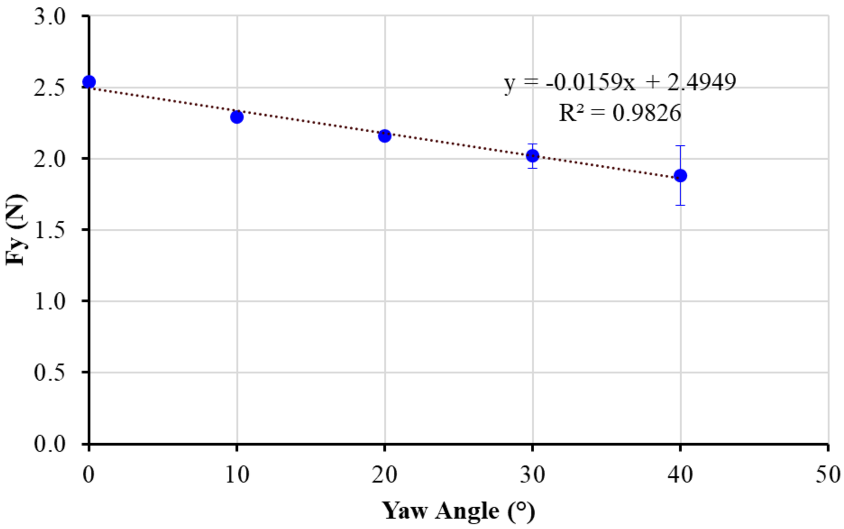

Figure 72. Graph of Fy versus the yaw angle of the upstream turbine

Figure 72 illustrates that the larger the yaw angle of the upstream turbine, the smaller the force exerted on the downstream turbine in the y-direction. This is explained by the deflection of the wake to the side in the horizontal direction, combined with the characteristic of the wake that it is rotating about the x-axis in a spiral shape as it travels downstream (as seen in Figure 4 section 1.2.1). From the hot-wire measurements taken and the velocity curves plotted of the LES model, it was observed that the larger the yaw angle the greater the presence of the wake at this location and therefore the greater the deflection of the wake. The lower velocity observed (shown in Figure 68(a)) also indicates a lower force experienced. From the smoke visualisation measurements taken, the reason for the decrease in Fy can be attributed to a combination of two features of the flow. The first feature is that the strength of the wake dissipates radially from the centre of the wake. A representation of this feature is shown in Figure

73, where a lighter shade of red represents a weaker wake region. When the tower comes into contact with the weaker region, it will experience a lower force. The second feature is that the tangent to the bottom of the spiral of the wake impinges on the measurement location, also illustrated in Figure 73.

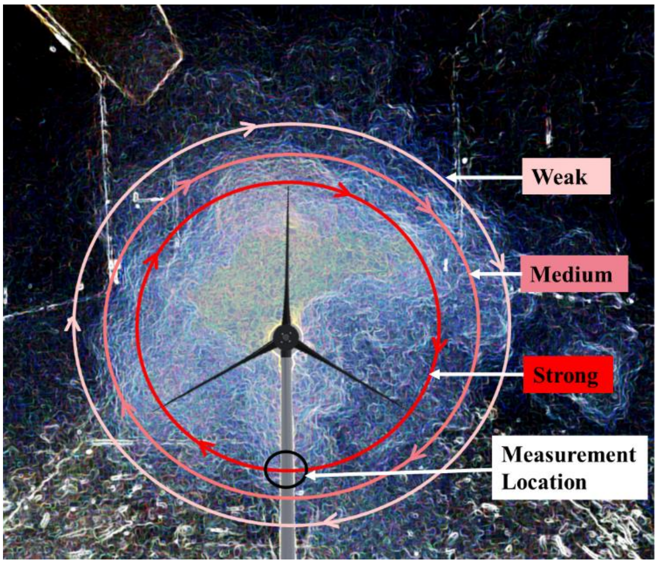

Figure 73. Illustration of the different strengths of the wake and the impingement of the wake on the tower at the measurement location

At an upstream turbine yaw angle of 0°, the strongest region of the wake (darkest shade of red) impinges on the measurement location and thus there is a strong force in the y-direction at the measurement location. At larger yaw angles, a vertical displacement is observed. Vertical displacement of the wake has been observed in a previous study done [27] and its magnitude and direction are dependent on the interaction between the counter-rotating vortex pair, the ground, and the rotation direction of the wake. As the upstream turbine is yawed and the wake is deflected upwards and to the right, a weaker region of the wake (lighter shade of red) impinges on the measurement location, resulting in a lower force. However, this deflection also results in a different tangent to the wake spiral impinging on the measurement location. The further up the circumference of the spiral wake, the greater Fz is and the lower Fy is (until there is only a force in the z-direction halfway up the circumference). See Figure 74 for a visual representation of the explanation given above. Therefore, as the yaw angle increases, Fy decreases.

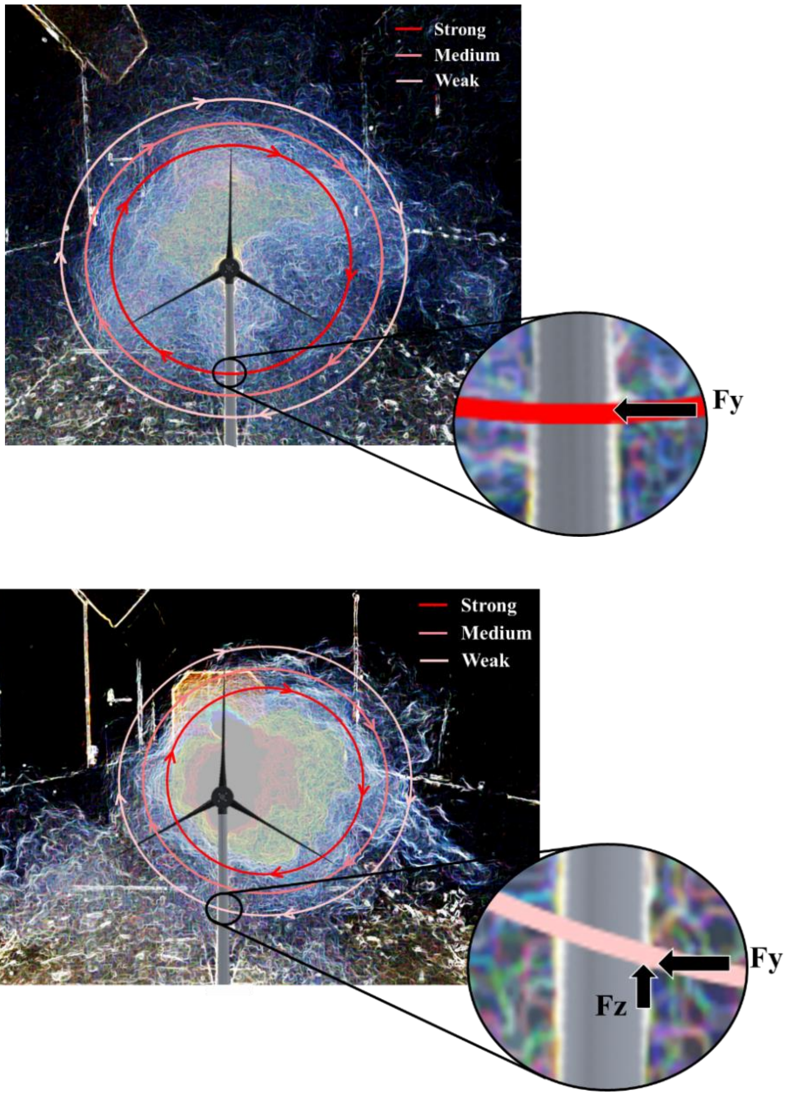

Figure 74. Illustration of the change in the magnitude of Fy on the tower from a yaw angle of 0° (top) to 30° (bottom)

Figure 75 shows the graph of the yaw angle of the upstream turbine versus the moment about the x-axis exerted on the downstream turbine.

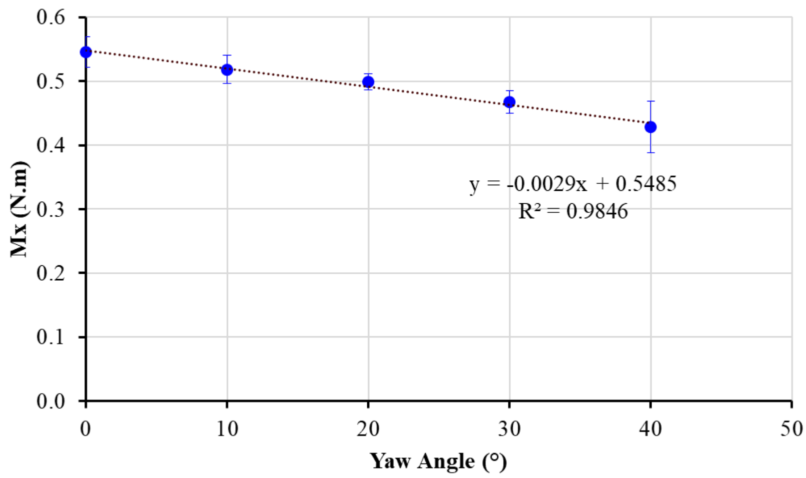

Figure 75. Graph of Mx versus the yaw angle of the upstream turbine

Figure 75 shows that the larger the yaw angle, the smaller the moment about the x-axis (Mx). This could be due to a decrease in Fy, an increase in the moment arm or a combination of both. From Figure 72, it can be seen that Fy does decrease. From Figure 76 it can be seen that there is a slight decrease in the moment arm, meaning that there is a slight deflection of the wake in the vertical direction. The moment arm is calculated by dividing the moment (Mx) by the force (Fy) at the different yaw angles. There is also a minimal change in the point of maximum velocity in the hot-wire anemometer measurements as seen in Figure 77.

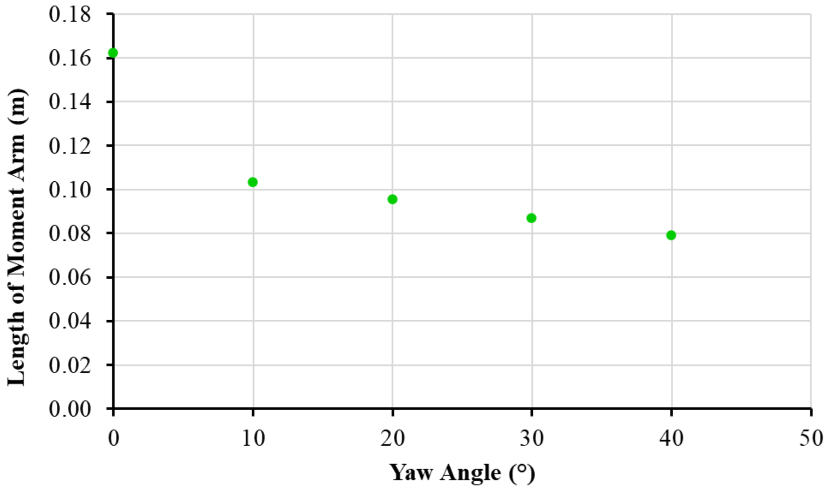

Figure 76. Moment arm of My at different yaw angles

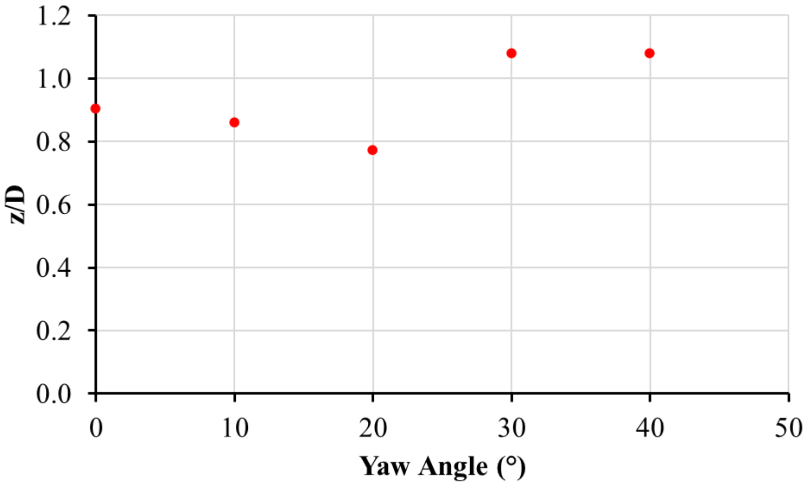

Figure 77. Position of maximum velocity at different yaw angles

Figure 78 shows the graph of the yaw angle of the upstream turbine versus the moment about the z-axis exerted on the downstream turbine.

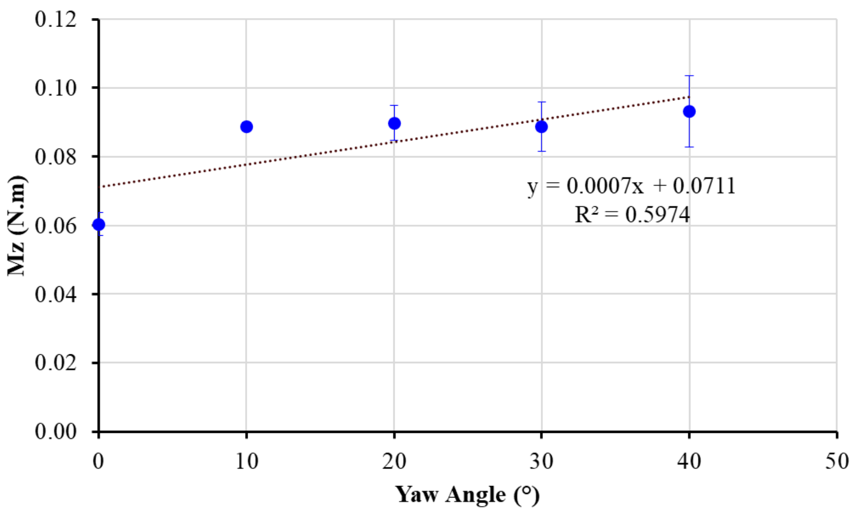

Figure 78. Graph of Mz versus the yaw angle of the upstream turbine

Figure 78 shows that the larger the yaw angle, the larger the moment about the z-axis. The difference between no yaw and a yaw angle of 40° is 0.033 N.m. This is explained by a combination of factors. The first is that as the wake is deflected to the right-hand-side, there is a greater entrainment of clean air on the left-hand side. This is evident in the smoke visualisation (Figure 62), LES results (Figure 56) and the hot-wire measurements (section 5.3). As the yaw angle increases, the location at the edge of the turbine ($y = -0.5D$) detects more of the wake, whereas the location at the opposite edge of the turbine ($y = +0.5D$) only detects the freestream velocity. Clean air has a higher velocity and therefore is expected to exert a greater force on the left of the turbine compared to the wake side that has a lower velocity. The second factor is the change in the length of the moment arm on both sides of the turbine. From literature describing the wake of a propeller, it is shown that there is a region of maximum velocity halfway between the hub and the tip of each blade, as seen in section 5.1 in Figure 57. The wind turbine model in this study has been shown to behave similarly to a propeller based on the results in section 5.1 and it can be assumed that there is a region of maximum velocity approximately halfway between the centreline of the wake and the edge of the wake as the turbine is yawed and the wake is deflected. This means that as the yaw angle increases, the point of maximum velocity (and thus maximum force) on the left-hand side moves closer to the hub of the downstream turbine and the point of maximum velocity (and thus maximum force) on the right-hand side moves further away from the hub of the downstream turbine. However, both the smoke visualisation or hot-wire measurements were not able to confirm the relative size of the moment arm on both sides of the tower.

From the experimental results presented above, the flow dynamics of the wake can be described as follows. When there is no yaw, the wake is mostly symmetrical about the centreline, with the minor non-symmetry attributed to the rotation direction of the rotor. The wake expands in the streamwise direction and the larger the yaw angle, the greater the expansion. Also, the larger the yaw angle, the greater the deflection of the wake in the yaw direction. The wake also experiences a deflection in the vertical direction due to the rotation direction of the wake and the interaction between a counter-rotating vortex and the ground. At large yaw angles, a kidney-shaped deflection of the wake can be observed from the front view which is caused by the interaction between the tip vortices and the freestream and the hub vortices, which create a counter-rotating vortex pair. The wake develops downstream in a helical pattern, while also oscillating along the spanwise axis. The downstream turbine causes the flow just in front of itself to accelerate before impingement. Apart from this, the downstream turbine does not affect the flow field. However, it is hypothesized that its orientation does affect some of the forces it experiences.

In conclusion, the larger the yaw angle of the upstream turbine, the lower the Fy, and Mx but not Mz. Therefore, it is beneficial in terms of the loading on the downstream turbine. In addition, the smoke visualisations and hot-wire measurements confirms the hypothesis that a larger yaw angle improves the entrainment of clean, undisturbed air and therefore likely increases the power output of the downstream turbine. This is in agreement with previous studies [17], [28], [77], [82]. Within the range of yaw angles studied, it is not certain what the optimal yaw angle is, which could be greater than 40°.

5.5 Validation of the Machine Learning Model by Comparison to the Original LES data

To validate the predictive capability of the ML algorithm outlined in section 4.2.4 – Neural Network Fitting (NNF), the ML model was trained on the original LES data, the model was used to predict the flow field at select yaw angles and these predictions were compared to the original LES data. The aim is for the ML model to be able to predict the flow field as closely to the original LES dataset as possible. A low percentage error will indicate that the model has good predictive capabilities and therefore can be used to predict other scenarios that may not necessarily have data to fully validate the results with.

As mentioned in section 3, there are only two yaw angles at which a uniform wake is reached throughout the flow field – at 10° and 30°. The ML algorithm requires a minimum of two yaw angles for training to predict the wake at different angles and therefore the flow field at 10° and 30° were used for training. However, this means that the ML algorithm predictions cannot be validated against any other yaw angles than those it was trained on. This is not ideal, but it still allows for an indication of the accuracy and effectiveness of the ML model.

As described in section 4.2.4, the ML algorithm that was used was an NNF model in MATLAB. It is important to note that because the dataset contains transient data, each timestep represents a different data point where the flow is at that particular angle. This is possible because the flow is slightly different at the different timesteps, but is still representative of the flow field at that same angle. A total of 174 training points were used for each yaw angle. This resulted in a training Predictor matrix of size 1 x 348. As found in section 4.2.4, the ML model needed to be trained in 2D top-view “slices” due to computational resource limitations. This resulted in 23 training Response matrices each of size 1998 x

348. The Levenberg-Marquardt algorithm was used with one hidden layer. This resulted in a training time of 15 minutes and 29 seconds.

A comparison was made between the original LES model and the resulting prediction of the wake trained on the LES data and the results are shown in Figures 79 and 80. The LES prediction is plotted in the top graph, followed by the original LES model in the middle, with the percentage difference between the two at the bottom. An average of all 174 instances was taken at both yaw angles to compare to the predicted flow field. These comparisons were made at the centre-plane of the flow field (z = 0D).

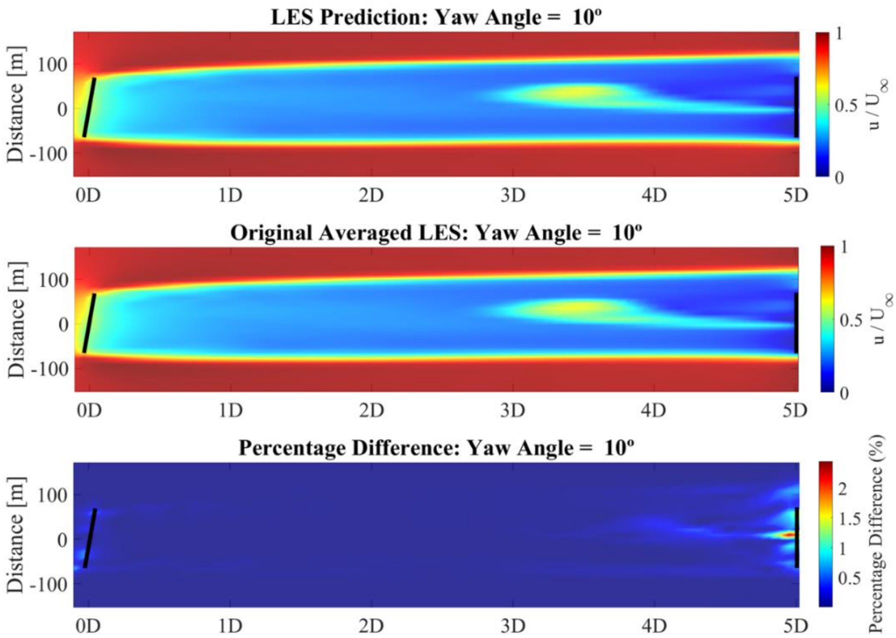

Figure 79. Top view prediction of the flow field at 10° and comparison to the original LES

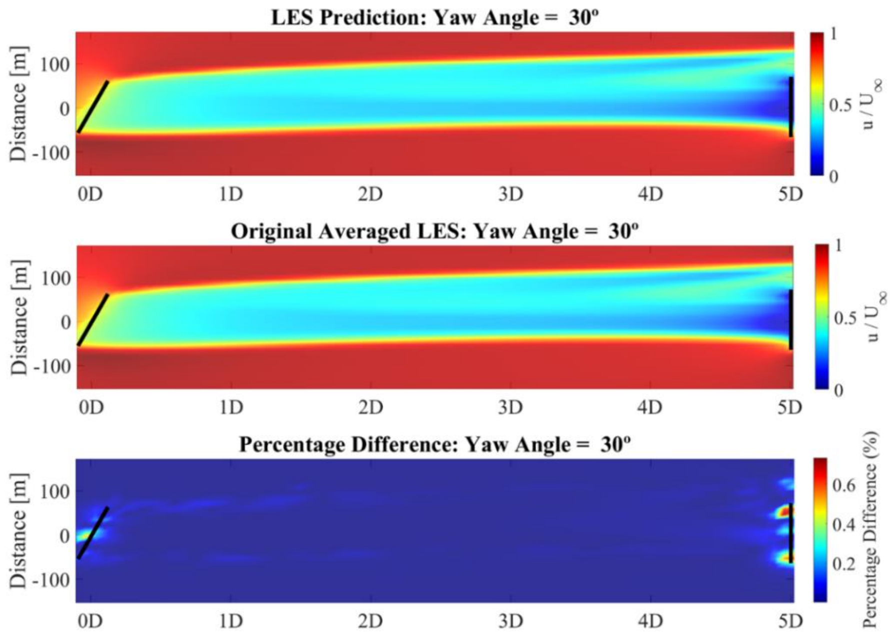

Figure 80. Top view prediction of the flow field at 30° and comparison to the original LES

The differences between the original LES model and the LES prediction are very small for both yaw angles, with a maximum percentage difference of 2.4% and an average error of 0.03%. The proposed reason for this is that an average was taken of all the timesteps of the original LES dataset, to result in a single time-averaged representation of the wake at a particular yaw angle (Original Averaged LES plots). The error is calculated by comparing the prediction to this time-averaged wake, which could be the cause for the small percentage errors. It is observed that the largest errors are concentrated around the two turbines. This can be attributed to the dynamics of the turbines.

These results show that the ML model has good predictive capabilities and therefore can be used to predict other scenarios with confidence.

5.6 LES-Trained Machine Learning Predictions

The final aim of this study is to investigate the ability of a surrogate model to accurately predict the wake of a two-turbine array at different yaw angles. The ML model was trained on the original LES data (baseline) from which the surrogate model predictions will be compared to. This is the same LES-Trained model that was created in section 5.6 but here the predictive capabilities of the model will be investigated. Visualisation of a sample of the training input, the model settings and the training time for a single slice is given below.

Table 9. Summary of the LES training data

Predictor variable size:	1 x 348
Response variable size:	1998 x 348
Sample of training data at 10°	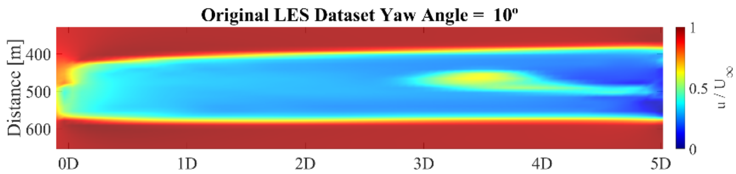
Sample of training data at 30°	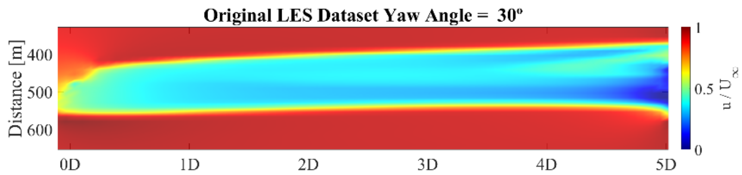
Training time per slice:	15 minutes 29 seconds

After the model was trained, functions were generated that represented the trained model at each slice. An array of different yaw angles can be fed into the functions and the model can output the flow field predicted at the required yaw angles for the required slices. Figure 81 shows the predicted flow field at the middle slice (z = 0D) for a sample of different yaw angles.

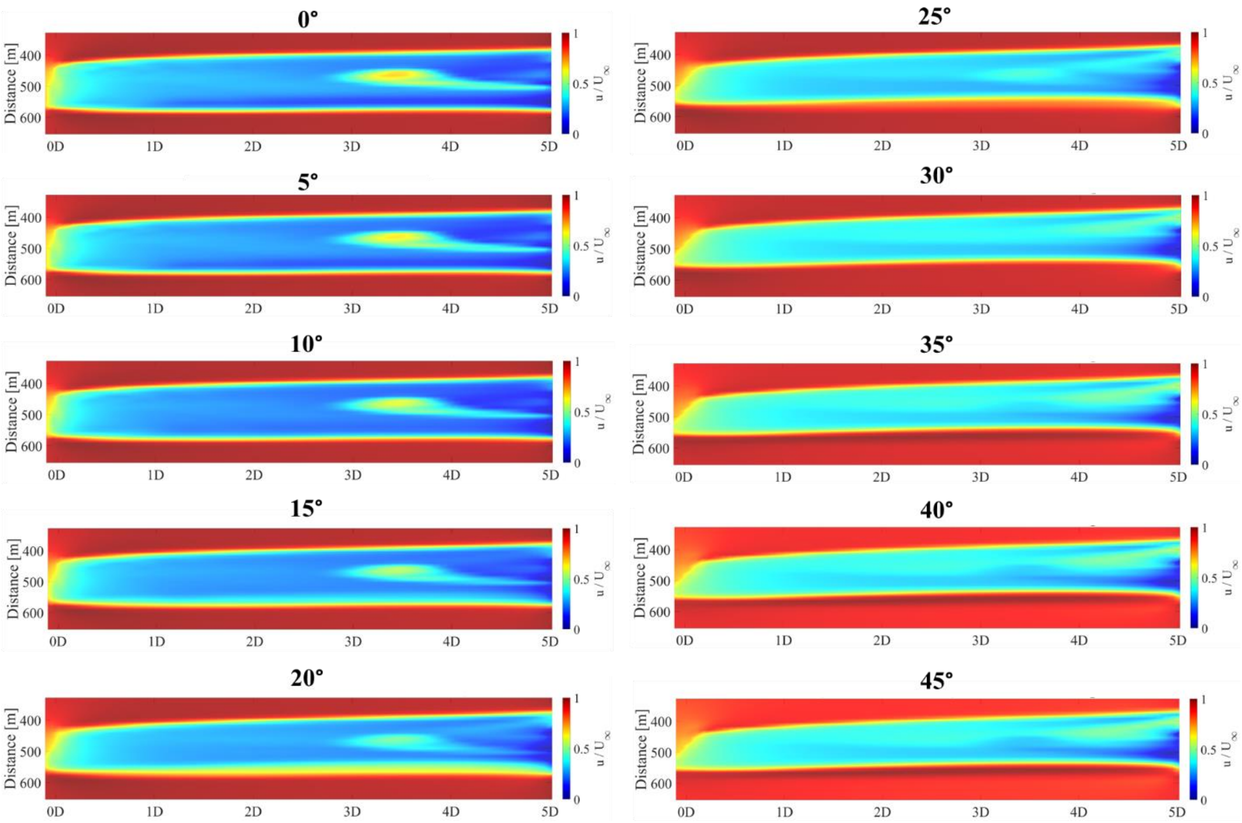

Figure 81. LES-trained model predictions at multiple yaw angles

A point-by-point velocity comparison of the LES-Trained model to the original LES the was made in section 5.5. At other angles, comparisons will be made with smoke visualisations.

The angles of deflection from the smoke measurements were calculated using the measured deflection of the wake at x = 5D and x = 0D. An illustration is shown in Figures 62 and 64. The angles of deflection from the LES-trained predictions were calculated using the same principle. However, an additional processing step was required to identify the edge of the wake and thus measure the deflection at the different streamwise locations.

It was first attempted to use the velocity matrix generated from the ML model to identify the edge of the wake. However, the velocity matrix was of size 27 x 74. 27 velocity points in the z-direction was too low a resolution. This meant that the difference between the velocity values from one row to another was very large, which resulted in the deflections at different yaw angles being very similar. An example of the deflection at x = 5D at different yaw angles is shown in Figure 82. Therefore, another method was required that had a finer resolution.

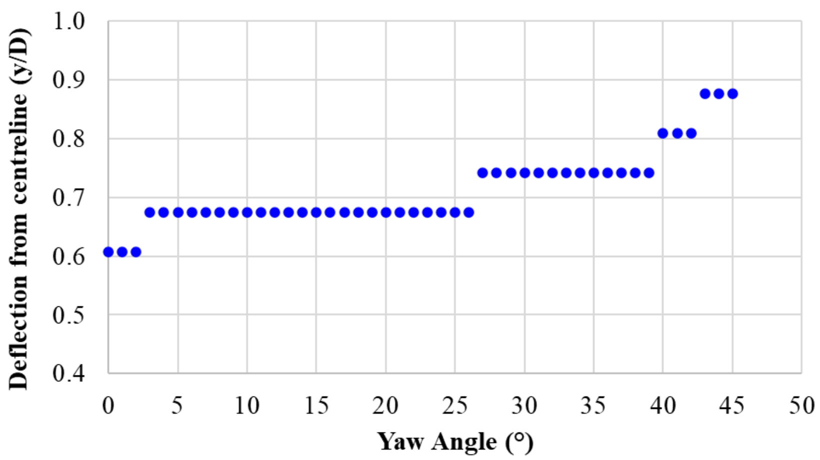

Figure 82. Deflection of the wake at x = 5D (Using Velocity Matrix)

Alternatively, one can use the images of the flow field since an automatic colour interpolation is performed to plot a colourmap from the velocity matrix. This results in a matrix of size 444 x 2212. It was first attempted to convert the RGB values of the image to grayscale and use the grayscale intensity matrices to identify the edge of the wake at the different streamwise positions. This conversion (in MATLAB) resulted in each pixel being represented by a single distinguishable value instead of a combination of three RGB values. Each pixel was given a single value from 0 to 255. The matrix of grayscale values was plotted in Excel. Conditional formatting was used to determine which grayscale value distinguishes the edge of the wake (found to be 200). However, upon further investigation of the MATLAB conversion function, certain peculiarities listed below were observed.

1. Pixels with the same grayscale intensity values had RGB values that differed significantly in numerical representation and in appearance. An example is shown below.

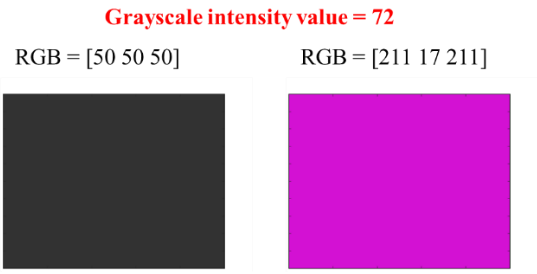

Figure 83. An example of pixels with the same grayscale intensity values with different RGB values

2. Pixels with the exact same RGB values had differing grayscale intensity values. For example, an RGB value of [255 67 255] can have a range of grayscale intensity values of between 114 and 116.

This could introduce inaccuracies in the quantification of the wake deflection because a pixel could be detected as matching the threshold edge value, but it could be a completely different RGB colour. Also, a pixel at the edge of the wake could be skipped because the grayscale intensity values differ whereas it is actually the exact same RGB value. Since the range at which these differences occur cannot be controlled or quantified, it was decided to use a different method where the error margin could be controlled.

An RBG image of the flow field at one yaw angle was still converted into a grayscale matrix to determine the preliminary threshold value of 200. However, this value was only used once to identify the corresponding RGB value that defined the edge of the wake. The row identified as the edge of the wake on the grayscale matrix was used to determine the exact RGB colours that define the edge of the wake. This RGB value was [255 211 50], which corresponds to the colour shown in Figure 84.

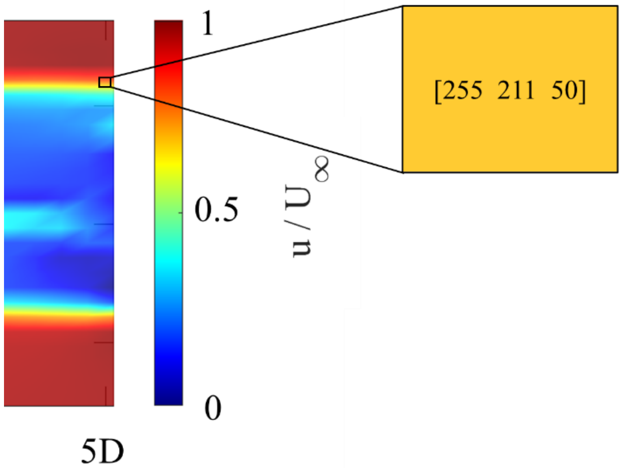

Figure 84. Threshold RGB value and the corresponding colour visualisation within the flow field

This RGB value was then set as the threshold value that all future RGB flow field images will use to identify the edge of the wake. A 5% error margin was set for each of the three RGB values because the exact same colour is not found in every image. This meant that the RGB values could each vary by 12.5. A visual representation of the four maximum limits of the colour variations and their corresponding RGB matrix is shown in Figure 85. This indicates that the margin is acceptable as there is not a significant difference in the colours and would still result in a true identification of the edge of the wake.

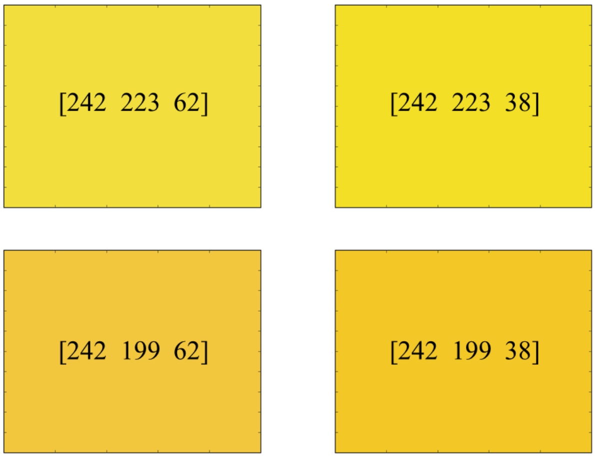

Figure 85. RGB limits of the threshold and their corresponding colour visualisations

For every image generated at the different predicted yaw angles, the edge of the wake was identified for six streamwise positions (0D, 1D, 2D, 3D, 4D and 5D) and the deflection at each location was calculated. Using these deflections, a curve was plotted describing the deflection of the wake as it develops downstream. An example of a deflection curve plotted for a predicted yaw angle of 15° is shown in Figure 86.

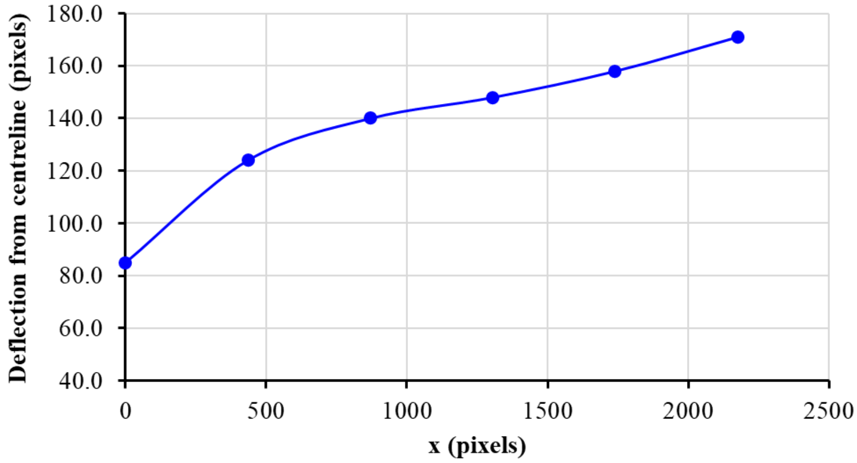

Figure 86. Deflection of the wake from the centreline at a yaw angle of 15°

It was observed that the trend of the curve most closely represents a straight line. Therefore, a straight-line equation was generated between x = 0D and x = 5D and the gradient of the curve was used to calculate the angle of deflection of the wake. This process was repeated for all predicted yaw angles from 0° to 45° for comparison to the smoke measurements. These results and a comparison to the DMD-Trained models are shown in section 5.8.

The error margins for the smoke measurements were calculated based on standard deviations of the deflections measured for the ten images at each yaw angle and the error in the deflection angle which made use of the arctan function. The error margins for the LES-Trained and DMD-Trained models were calculated based on the error in identifying the correct pixel RGB value that represents the edge of the wake, the error in the deflection of the wake at the different streamwise positions and the error in the deflection angle. The error in the models is relatively small mostly because the accuracy to which a single colour can be identified is high as it makes use of three values.

5.7 DMD-Trained Model

To determine which physical properties of the wake flow are most important in reconstructing an accurate flow field, different mode groups were combined and reconstructed together. The results are detailed below. However, based on the reconstructions in section 4.2.3, it is hypothesized that Group 1 will result in the most accurate predictions.

Table 10. Summary of the physical property that each group is linked to

Mode Group	Physical Property
1	Mean flow
2	Tip vortices
3	Tower vortices
4	Yaw of the wake
5	Other

As explained above, the ML model requires a minimum of two data sets for training. Since the flow field changes from 10° to 30°, the mode values also change. Hence, the modes needed to be generated at both these angles. The dataset at the two angles were fed separately into the ROM, which resulted in the generation of two sets of modes (one set at each yaw angle). However, due to the different structure of the flow fields at the two yaw angles, it could not be assumed that the modes would be grouped the same for both yaw angles. For example, at 10° mode 2 could belong to Group 2 but at 30° it could belong to Group 3. Therefore, the modes from each yaw angle were grouped separately. An illustration of this process is shown in Figure 87.

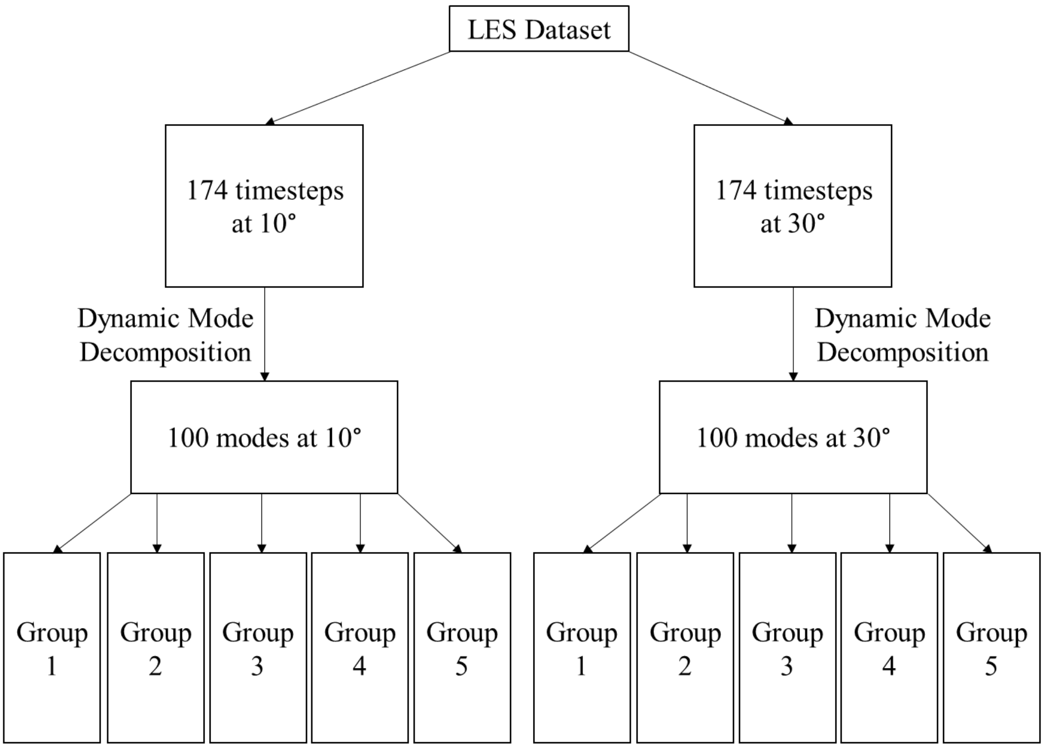

Figure 87. Illustration of the division of the LES dataset and grouping of the modes

As mentioned above, the grouping was done through visual inspection. It was discovered that the modes generated when the dataset is split have a much lower velocity compared to the modes generated when the full transient dataset is used (seen in section 4.2.3 and Figure 41). This is because the full flow field at each yaw angle is in a pseudo steady-state and most of the dynamics are removed, since the input to the DMD is only a single yaw angle. Therefore, the modes generated for these flow fields also have lower velocities. However, the modes were still able to be grouped into the five groups given above. The grouping of the modes at each yaw angle is shown in Table 11 and 12. An example of one mode from each group is visualised and the mode it represents is in bold and highlighted in red.

Table 11. Mode groupings at a yaw angle of 10°

Mode Group	**Modes and Visual Representation of a Single Mode from the Group**
1 – Mean Flow	**1** 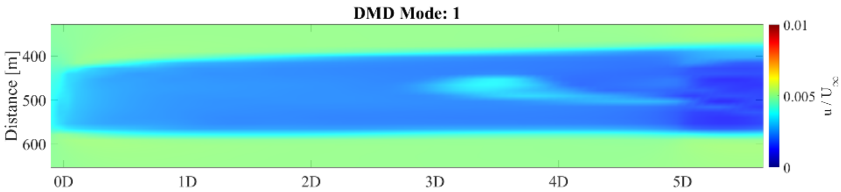
2 – Tip Vortices	48, 50, 51, 52, 53, 54, 55, 56, 57, 60, 61, 62, 63, 64, 65, 68, 69, 70, 71, 72, 73, 74, 75, 76, 78, 79, 80, 82, 83, 84, 85, 86, 87, 89, 91, 95, 96, **97**, 98, 99, 100 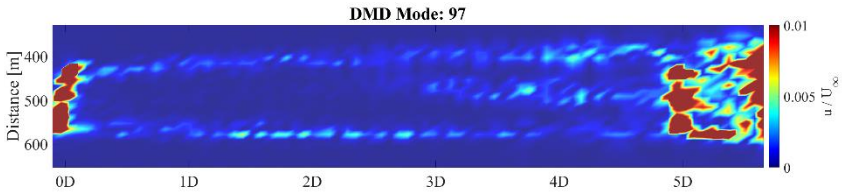
3 – Hub/Tower Vortices	6, **7**, 8, 11, 18, 19, 21, 22, 24, 25, 29, 30, 31, 36, 40, 44, 45, 47, 55, 58, 59, 66, 67, 77, 81, 88, 90, 92, 93, 94 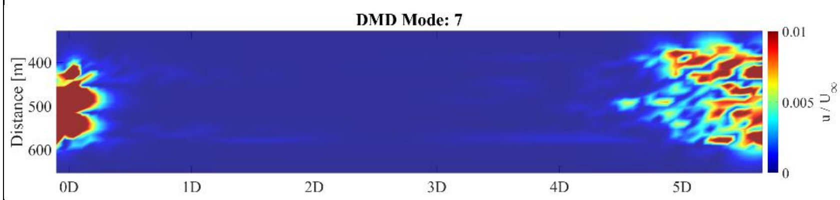
4 – Yaw	**9**, 10, 12, 14, 15, 16, 17, 20, 23, 26, 27, 28, 32, 33, 34, 35, 37, 38, 39, 41, 42, 43, 46, 49 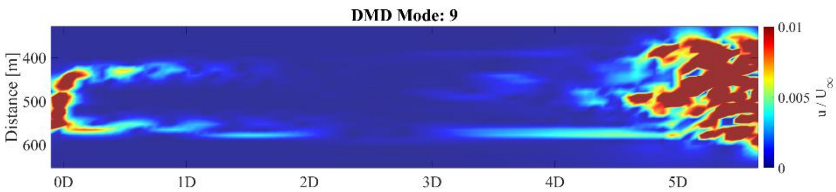
5 - Noise	No Modes

Other	**2**, 3, 4, 5 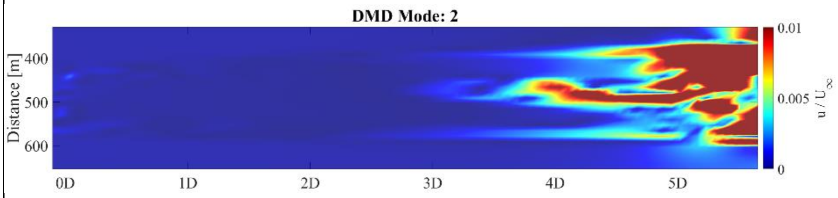

Table 12. Mode groupings at a yaw angle of 30°

Mode Group	**Modes and Visual Representation of a Single Mode from the Group**
1 – Mean Flow	**1** 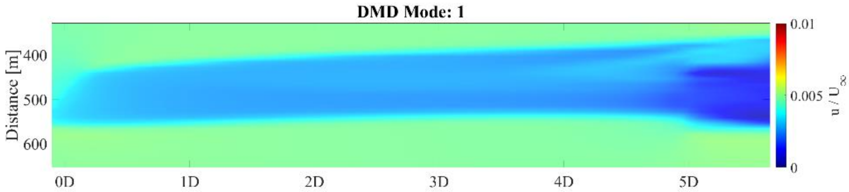
2 – Tip Vortices	9, 11, 12, 13, **15**, 16, 17, 95, 96, 98, 99, 100 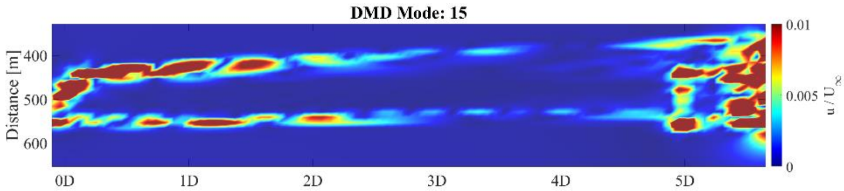
3 – Hub/Tower Vortices	3, 4, 6, 22, 23, 24, 26, 31, **32**, 33, 34, 35, 36, 37, 38, 3, 40, 41, 42, 43, 44, 45, 46, 47, 48, 49, 50, 51, 52, 53, 56, 57, 58, 59, 60, 61, 62, 63, 64, 65, 67, 68, 69, 71, 74, 76, 79, 83, 88, 89, 90, 91, 92, 93, 94, 97 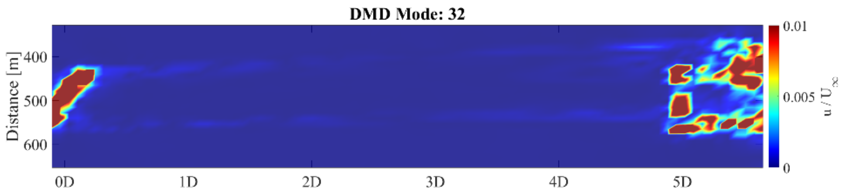
4 – Yaw	8, 10, 14, 18, 19, **20**, 54, 55, 66, 70, 73, 75, 77, 78, 80, 81, 82, 84, 85, 86, 87 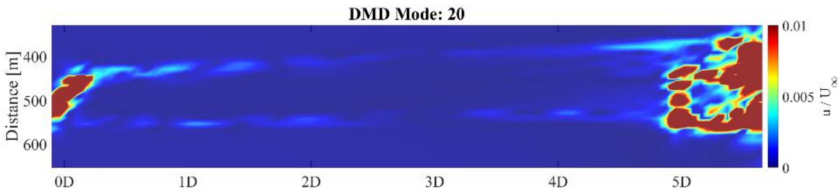

5 - Noise	7, 27, 28 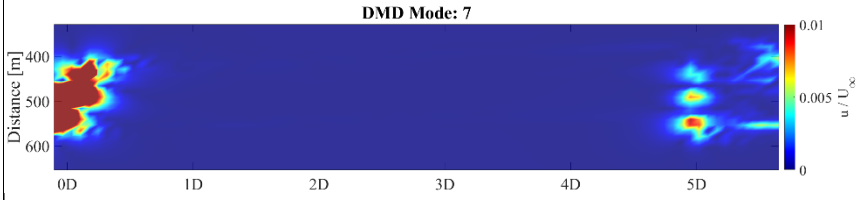
Other	2, 5, 21, 25, 29, 30 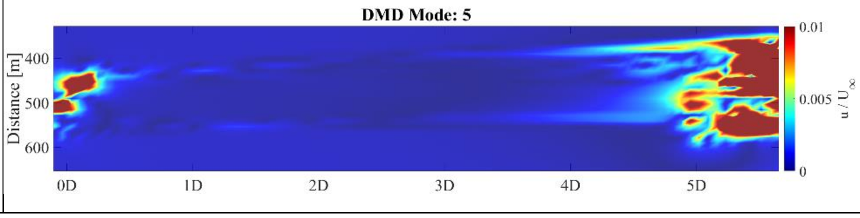

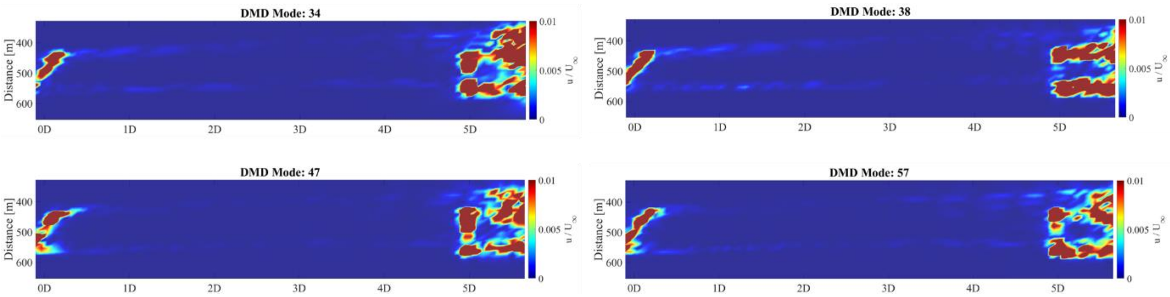

Figure 88. A sample of four modes from Group 3 at 30°

Train with an entire group

It was first attempted to train the ML model to predict the behaviour of a single group by feeding in all the modes from the entire group (at 10° and 30°). Visualisation of a sample of the training input, the model settings and the training time for a single slice when training Group 4 is given below. The output from the ML model is also shown in Figure 89 for a sample of yaw angles.

Table 13. Summary of the DMD training data

Predictor variable size:	1 x 45
Response variable size:	1998 x 45
Sample of training data at 10°	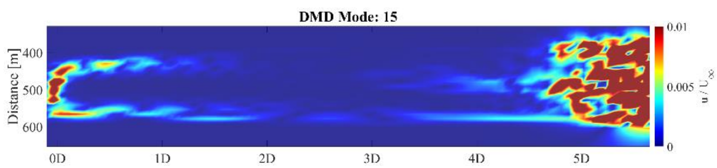
Sample of training data at 30°	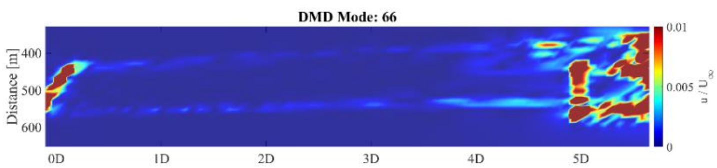
Training time per slice:	2 minutes 59 seconds

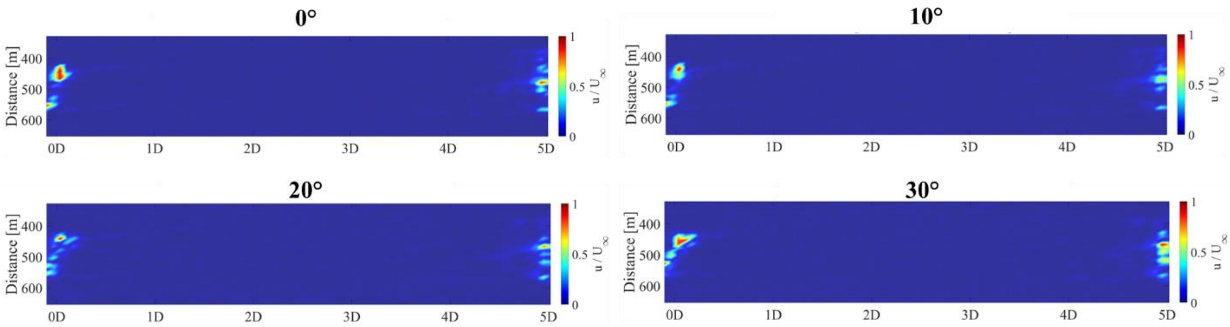

Figure 89. ML output predictions when trained with all the modes of Group 4

The output is the prediction of a single mode group at different yaw angles – not a prediction of the flow field. The output matrices are of size 1998 x 1, where each column matrix represents the mode group at a particular yaw angle. In order to reconstruct the mode group back to a flow field, it needs to be multiplied by the state-space matrix variable *xstates*. The state-space matrix converts modes back into a full transient flow field dataset. The size of the state-space matrix for 100 modes 100 x 909, where each row corresponds to a specific mode and each column represents a different timestep. However, it was discovered that multiplication of the mode matrix predicted with the *xstates* variable would not result in the intended reconstruction. In order to make the multiplication mathematically possible based on matrix sizes, the predicted mode group matrix (1998 x 1) would need to be multiplied with a single row from the state-space matrix (i.e. 1 x 909). However, the prediction is of an entire mode group, which consists of multiple modes. Therefore, the reconstruction cannot be performed accurately if the entire group is reconstructed using the value of a single mode (single row of *xstates*).

Train with individual modes

After training, all the modes from a certain group can be combined and used to reconstruct the flow field. However, when training with individual modes, it is important to make sure that the same mode at 10° and at 30° is used. This proved to be challenging because as the flow field changes with the yaw angle, so do the values of the modes. This means that without a definite ranking method that ensures correct ranking of the modes despite yaw angle, there is no way to keep track of individual modes. Also, even if the modes were able to be ranked by a definite parameter, it is not certain that a mode's values will change proportionally with a change in yaw angle. For example, mode 2 might have the 4th highest energy value at 10°, but the 9th highest energy at 30°. However, to investigate this method further, the following process was used. Before training, the 100 modes at 10° and 30° were placed into the five groups based on visual appearance, as shown in Table 11 and 12. Within each group (for each angle) the modes were ranked according to highest frequency (subgroup a) and according to highest energy (subgroup b) as these are the most defining characteristics of the modes. A sample of the ranking in group 2 is shown below. As determined in section 4.2.2, the modes exist in eigenvalue pairs. However, some modes shown below are not paired because the second half of their pair is in a different group.

Table 14. Ranking of the modes within Group 2a and Group 2b

Group 2a			Group 2b		
Rank Within the Group	Corresponding Mode from 10°	Corresponding Mode from 30°	Rank Within the Group	Corresponding Mode from 10°	Corresponding Mode from 30°
1	97, 98	96	1	99, 100	96
2	85, 86	99, 100	2	91	99, 100
3	87	95	3	87	12, 13
4	79, 80	98	4	68	98
5	54	16,17	5	60, 61	95

Using their new rankings, each mode (at 10° and 30°) was fed into the ML model and the model output predictions of the individual modes at different yaw angles. Visualisation of a sample of the training input, the model settings and the training time for a single slice when training mode 1 is given below.

Table 15. Summary of the DMD training data for a single mode

Predictor variable size:	1 x 2
Response variable size:	1998 x 2
Training data at 10°	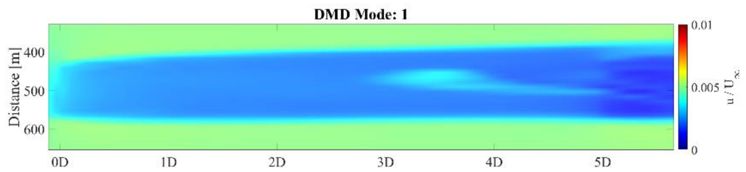
Training data at 30°	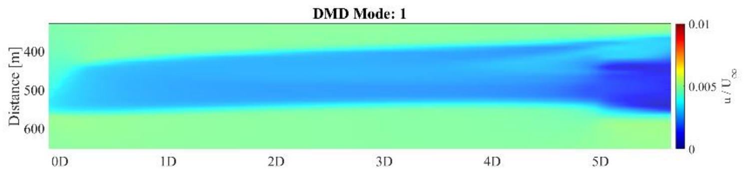
Training time per slice:	1 second

Since individual modes were output, the flow field can be reconstructed using the state-space matrix. For example, to reconstruct group 2, modes a, b and c can be combined and multiplied by columns a, b and c of the state-space matrix – ensuring that each mode is multiplied with the correct corresponding state-space column. However, this introduced another complication. A state-space matrix is generated from DMD and it is dependent on the yaw angle. Since the LES dataset contains data at 10° and 30°, the state-space matrix at these two angles can be generated with good accuracy. However, since there is no LES data at the intermediate angles at which the predictions are made, the state-space matrix for these angles cannot be generated using the same DMD process. To assess the outputs of this model despite the sources of error, the additional state-space matrices were generated by feeding it into the same ML model as is used for the modes. The ML model was trained on the state-space matrices at 10° and 30° and it was used to predict the state-space matrices at the intermediate angles. However, it is expected that this method does not result in accurate state-space matrices because the matrices are not dependent only on yaw angle. There are multiple other factors in the DMD process that differentiate one state-space matrix from another and the ML model does not take these factors into account, i.e. the state-space matrices may not progress uniformly from 10° to 30° as the ML model predicts. This could contribute greatly to the error in the prediction.

Different combinations of groups were reconstructed separately and together to assess which groups (and thus physical properties of the wake) are most important for the reconstructions. The reconstructions were compared to the original LES data and an average of the errors at the two yaw angles were taken. It was found that the reconstruction using Group 1 alone results in a good representation of the flow field whereas Groups 2, 3, 4 and 5 individually do not represent the flow field at all, as was observed in section 4.2.3. Therefore, the results shown in Figure 90 contain only the reconstructions when Group 1 is combined with different groups and subgroups. Subgroup 'a' refers to the group ranked according to highest frequency and subgroup 'b' is ranked according to highest energy.

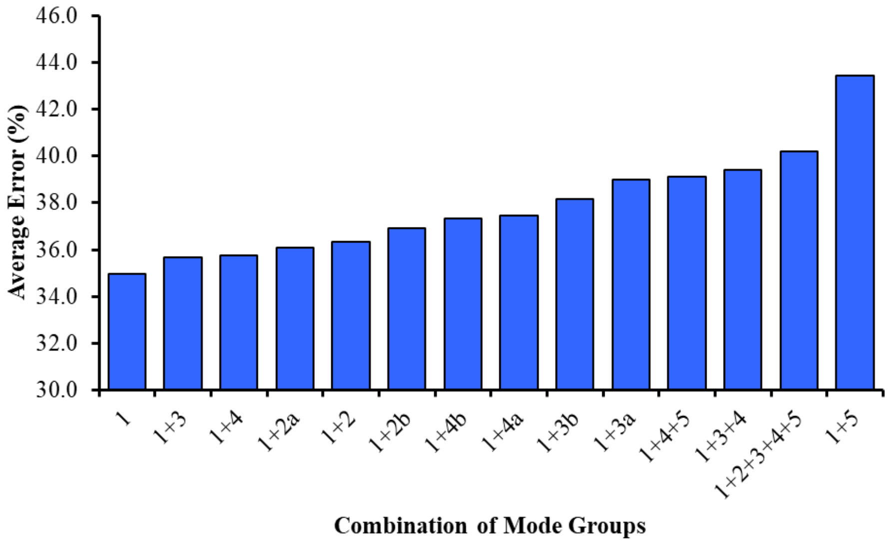

Figure 90. Average error of the reconstructions using different mode group combinations

Figure 90 shows that Group 1 (mean flow) is the most important for reconstruction of the flow field. This is because the ML model is trained on instances where the flow field is at a pseudo steady-state. It was observed that the more modes that are used, the worse the predictions get. Since Group 1 results in the most accurate predictions, the results onwards will be using only Group 1. Figure 91 shows the reconstructions of the flow field when Group 1 was used.

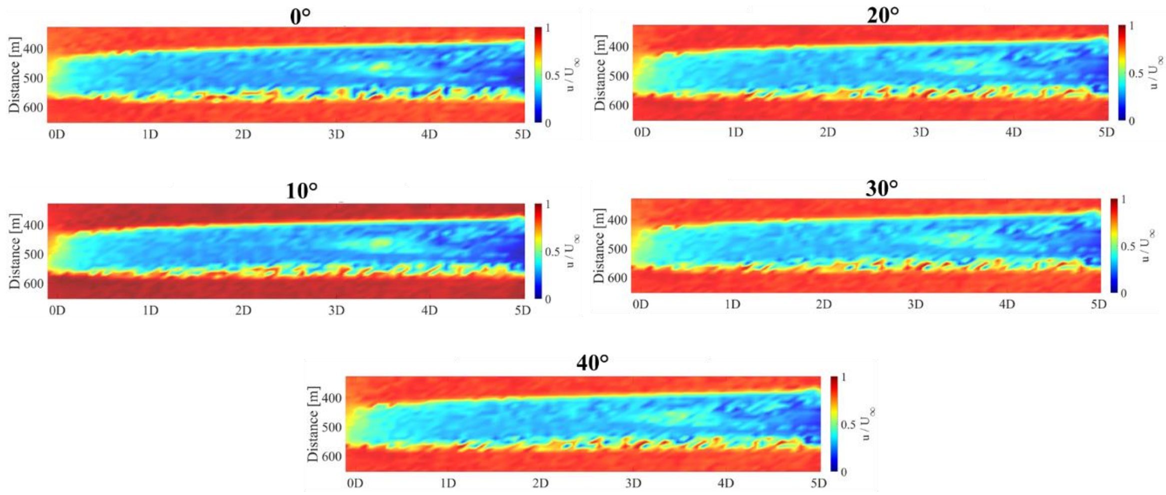

Figure 91. Reconstruction of the flow field using only Group 1

It is observed that there is not much change in the overall wake structure at the different yaw angles and the amount of change in the deflection of the wake is not clearly visible. For a more detailed evaluation of the predictions, the velocity field predictions from this DMD-trained model are first compared to the LES-trained predictions. The results are shown in Figure 92.

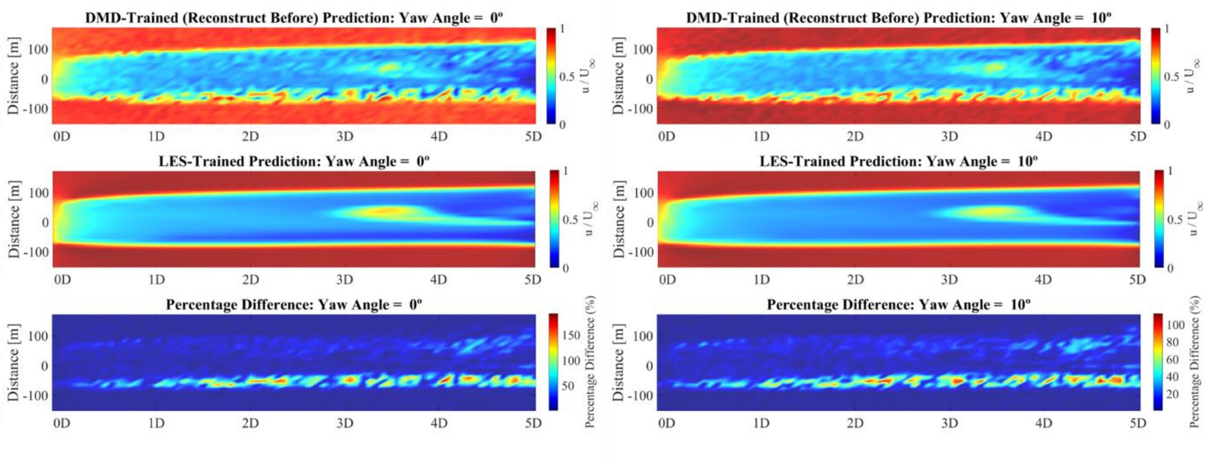

Figure 92. Comparison between the DMD-Trained model and the LES-Trained model at a sample of yaw angles

Predictions at four yaw angles are shown above because the predictions do not change significantly throughout the different yaw angles. When compared to the LES-Trained model, the average error throughout all the yaw angles is 6.96%. It is observed that the largest errors occur the edge of the wake where the wake is supposed to deflect away from. This means that the DMD-Trained model does not predict the deflection of the wake well. To investigate further the ability of the DMD-Trained model to predict the deflection of the wake, the angle of deflection of the wake will be quantified and compared to the smoke visualisation measurements. The angles of deflection of the predictions were calculated in the same way as the LES-trained predictions above and are compared in Figure 95.

5.8 DMD-Trained (Reconstruct Before)

Reconstructing the flow field before training the ML model removes the need for different state-space matrices. Since the ML model is trained with reconstructions at the two yaw angles, the output is an already reconstructed flow field at the intermediate angles. In this method, the modes from the specific mode groups are combined and the transient flow field is reconstructed (at each of the two yaw angles). For each mode group, the resulting matrix is of size 2241 x 174. It is important to note that this method does not reduce the computational resources used – unlike the DMD-Trained method above – because reconstructing the flow results in the same size of matrices as the original LES dataset. Therefore, this method would have no computational resource advantage over using the original LES data. However, it is possible that this method could result in better predictions since the noise and unnecessary dynamics present in the LES data can be filtered out. But to assess if this method has any advantages over training with the LES data, an additional dataset would be required. However, the purpose of testing this method is just to observe the possible accuracy achievable when training with DMD data of a single group.

Visualisation of a sample of the training input, the model settings and the training time for mode Group 1 is given below.

Table 16. Summary of the DMD training data (reconstruct before)

Predictor variable size:	1 x 348
Response variable size:	1998 x 348
Sample of training data at 10°	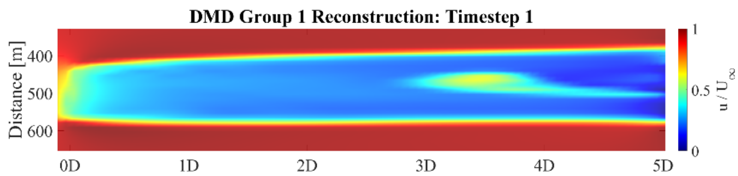
Sample of training data at 30°	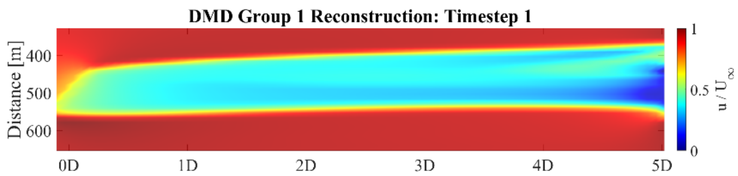
Training time per slice:	12 minutes 30 seconds

Figure 93 shows the predicted flow field at the middle slice (z = 0D) at a sample of different yaw angles.

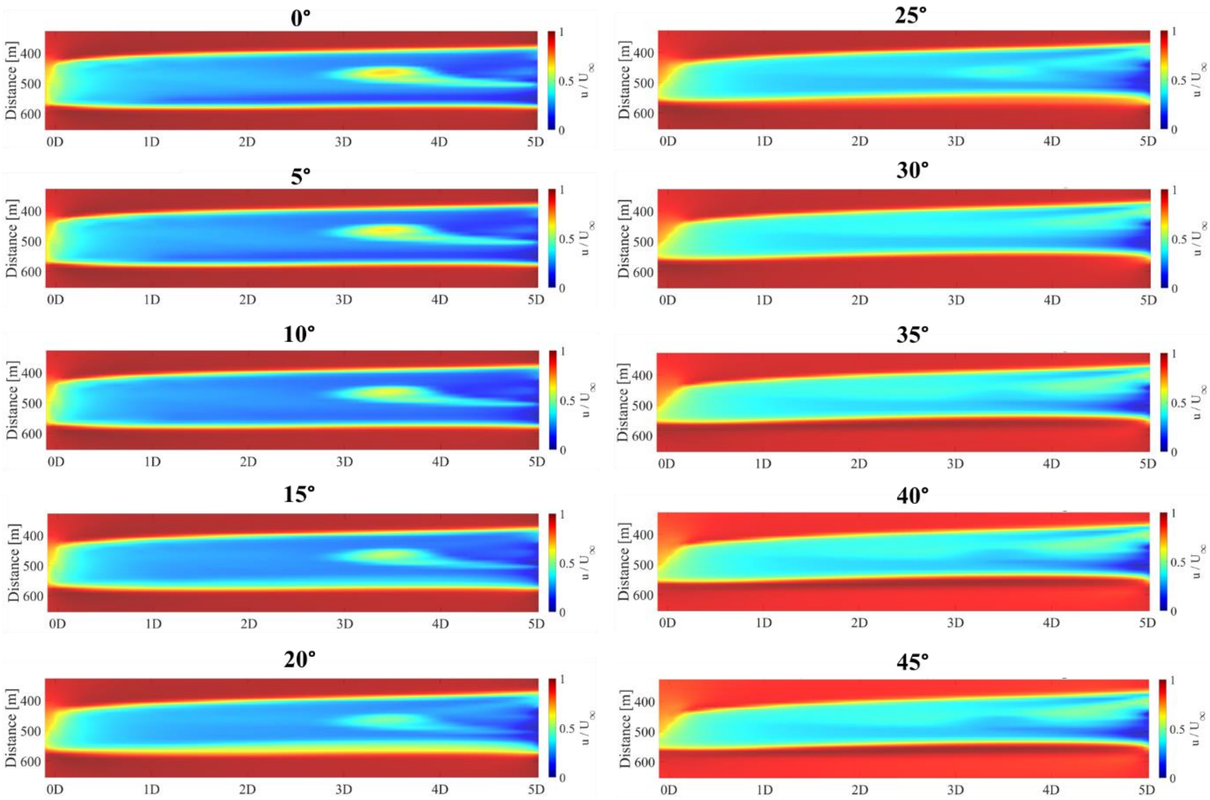

Figure 93. DMD-trained (reconstruct before) model predictions at different yaw angles

A velocity field comparison between the DMD-Trained (reconstruct before) model and the LES-trained model is shown below at a few select yaw angles.

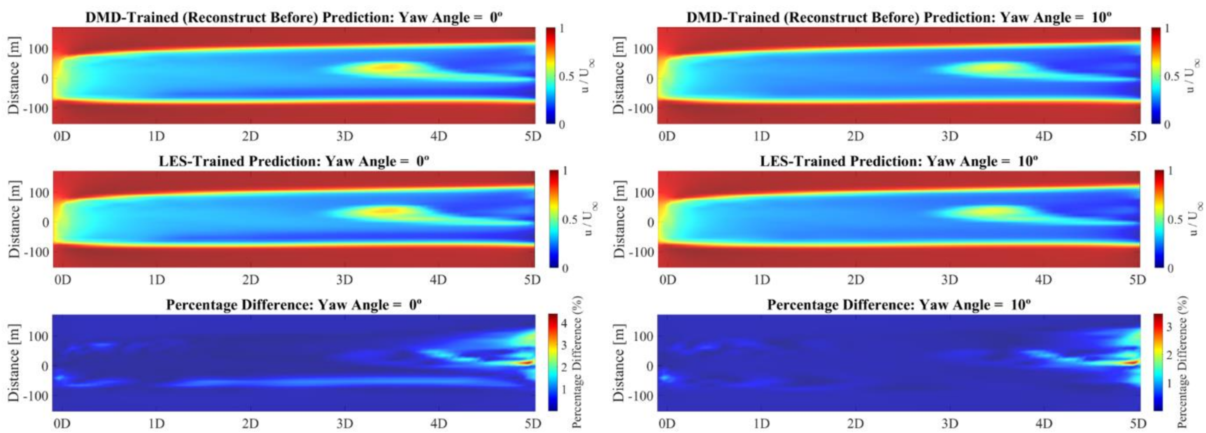

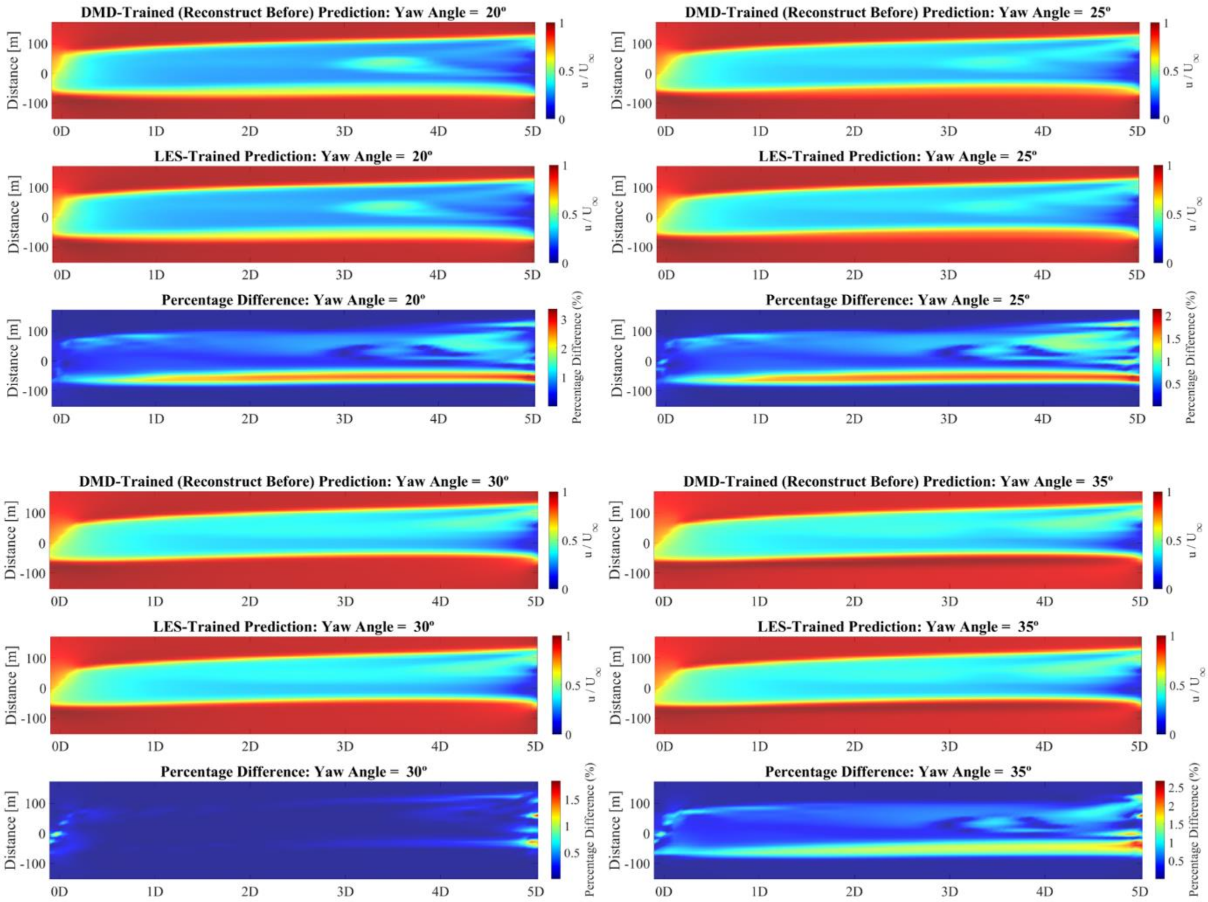

Figure 94. Comparison between the DMD-trained (reconstruct before) model predictions and the LES-trained model predictions

The average percentage difference between the LES-Trained and the DMD-Trained (reconstruct before) model was 0.38%. However, as mentioned above, it cannot be proven which model results in the most accurate predictions of the wake unless another dataset is used that both models are compared to. As observed in Figure 94, the largest errors occur at the edge of the wake where it should deflect away from. This means that the two models predict the deflections of the wake slightly differently, especially after 10°. The same process that was used to quantify the deflection angle of the previous two models was used for this model and the comparison is made below.

Table 17. Comparisons of Angles of Deflection for Different Methods

Yaw Angle (°)	Smoke Visualisation (°)	LES-Trained Predictions (°)	DMD-Trained Predictions (°)	DMD-Trained Predictions (reconstruct before) (°)
0	1.49	2.028	2.185	2.212
15	2.10	2.264	2.422	3.210
30	2.75	3.735	2.343	3.709
45	3.43	3.735	2.317	3.473

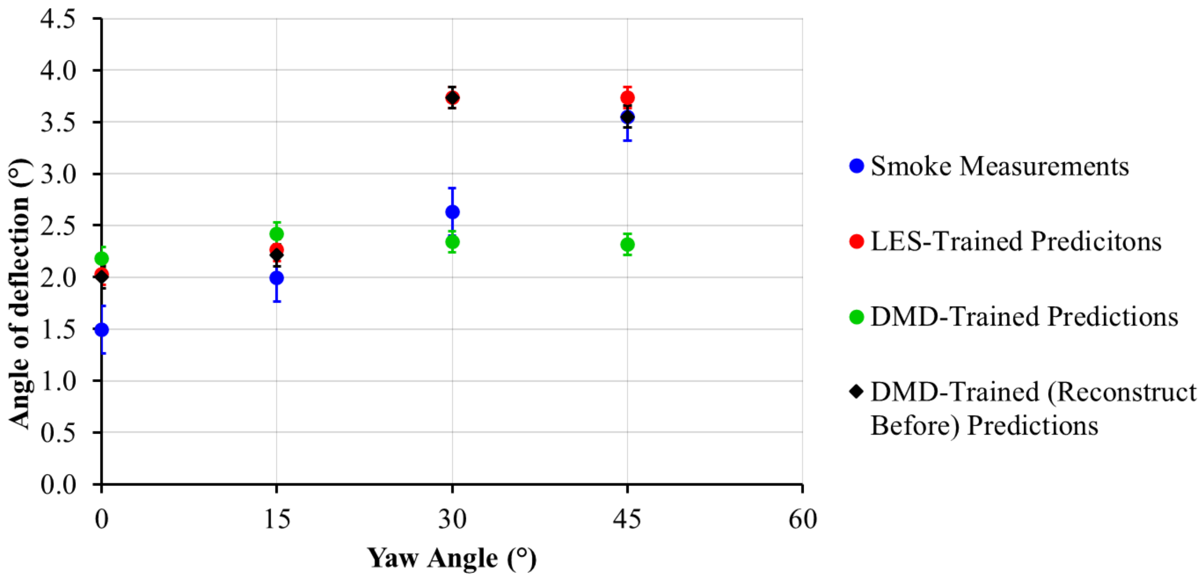

Figure 95. Comparison of the angles of deflection between the smoke measurements and all three ML models

Similar trends are observed for the smoke measurements, LES-Trained model and DMD-Trained (reconstruct before) models. The larger the yaw angle the larger the angle of deflection. However, the models indicate a small increase from 0° to 10°, a large linear increase from 10° to 30° and then a possible plateau from 30° onwards. Since the training data fed into the ML model was at 10° and 30°, it is hypothesized that the minimal change in angle of deflection before 10° and after 30° is attributed to the limits of the ML model. This could indicate that the ML model is good at interpolation but not at extrapolation. As mentioned in section 5.4, it is expected that a limit should exist because at a certain yaw angle, the turbine will reach a stall angle thus the yaw angle would not have a significant effect on the wake deflection. However, the smoke measurements indicate this limit is beyond 45°. Due to three out of the four predictions for both models falling within the error margins of the smoke visualisation measurements, it can be concluded that there is a good agreement between the three.

The DMD-Trained model does not predict a significant change in the deflection of the wake at different yaw angles, indicating worse predictive capability. The sources of error can be attributed to the quality of data that it is trained on and the error in reconstruction. Firstly, there is inaccuracy induced in the tracking of a mode through the different yaw angles. Secondly, there is error in the generation of the state-space matrices at intermediate angles.

The surrogate model method (DMD-Trained) has shown that it significantly reduces the computational resources required since a single mode can be used instead of an entire LES flow field. However, due to the challenges with reconstruction, the end predictions are not good. To combine achieving both an accurate prediction and a reduction in computational resources, complications such as the mode tracking and the prediction of accurate corresponding state-space matrices for different yaw angles would need to be overcome.

6 CONCLUSION

From the combination of experimental measurements taken and the results generated from the surrogate model, a greater understanding of the wake characteristics and the loads experienced by the downstream turbine due to the upstream turbine being at non-zero yaw angles was achieved. It was determined that a larger yaw angle results in a greater deflection of the wake. This relationship is hypothesised to be linear until the tested yaw angle of 45°, however it is expected to plateau after it reaches its stall condition. The maximum angle of deflection recorded experimentally was 3.4° and from the surrogate model the maximum was 3.7°. A greater deflection means that there is greater entrainment of clean, undisturbed air with more energy and thus it is expected that this would lead to greater combined power outputs of the turbine array. It was also found that a larger yaw angle results in lower forces and moments being exerted on the downstream turbine due to the deflection of the wake. This means that this wake redirection technique is beneficial for both the power output and the lifespan of the wind turbines.

The surrogate model tested can predict the wake of a two-turbine array when the upstream turbine is at other non-zero yaw angles than those it was trained on. The LES-trained model predicts the wake behaviour and deflection of the wake very similarly to what was observed with the experimental measurements. The DMD-trained (reconstruct before) model, in which specific modes were chosen for prediction, predicts the wake very similarly to the LES-trained model (average difference of 0.38%) and therefore also to the experimental measurements, with an average difference in deflection to the experimental results of 19.8%. This model does not reduce the computational resources required when compared to the LES-trained model, but it could have an advantage in that only select modes were used instead of the entire flow field. However, it is not possible to test this comparison with the current dataset. The DMD-trained model, in which specific modes were chosen for prediction and the reconstruction was made after training, did not predict the wake deflection well. This is attributed to the inaccuracy in tracking of a mode through different yaw angles and the difficulty in generating accurate state-space matrices at predicted yaw angles. To achieve both an accurate prediction and a reduction in computational resources, complications such as those mentioned above would need to be resolved.

7 RECCOMENDATIONS

- To be able to further test the predictive capability of the LES-Trained and DMD-Trained models, it would be useful to have a second dataset that contains flow field information at the intermediate yaw angles. This way the surrogate model predictions can be validated against other yaw angles and not just those it was trained on.

- The capability and effectiveness of the DMD-Trained model is limited by the ability to track individual modes through different yaw angles and the ability to generate accurate state-space matrices for reconstruction of the flow field. Therefore, to improve the prediction capability, it would be important for future work to investigate how an individual mode can be kept track of through the different yaw angles to ensure the correct modes are used during reconstruction. It would also be important to develop a method to accurately generate the state-space matrices at the intermediate yaw angles.

- For a more in-depth analysis of the forces exerted on the downstream turbine, an iterative design and testing process of a wind turbine model would be required to ensure the model behaves like a wind turbine and not a propeller.

8 REFERENCES

[1] F. Porté-Agel, M. Bastankhah, and S. Shamsoddin, “Wind-Turbine and Wind-Farm Flows: A Review,” *Boundary Layer Meteorol*, vol. 174, no. 1, pp. 1–59, Jan. 2020, doi: 10.1007/s10546-019-00473-0.

[2] Editor, “Vertical Axis Wind Turbines vs Horizontal Axis Wind Turbines.” Accessed: Oct. 24, 2024. [Online]. Available: https://www.windpowerengineering.com/vertical-axis-wind-turbines-vs-horizontal-axis-wind-turbines/

[3] WindcycleEnergy, “The Pros and Cons of Vertical Axis Wind Turbines.” Accessed: Oct. 24, 2024. [Online]. Available: https://windcycle.energy/vertical-axis-wind-turbines-2/#:~:text=VAWTs%20have%20lower%20efficiency%20rates,of%20energy%20as%20a%20HAWT.

[4] Luvside, “Horizontal wind turbines: advantages & disadvantages.” Accessed: Oct. 24, 2024. [Online]. Available: https://www.luvside.de/en/hawt-advantage-disadvantage/

[5] Energy.gov, “How Do Wind Turbines Work? ,” https://www.energy.gov/eere/wind/how-do-wind-turbines-work. Accessed: Oct. 09, 2024. [Online]. Available: <div class="csl-entry">gov, E. (n.d.). *How Do Wind Turbines Work?* . Https://Www.Energy.Gov/Eere/Wind/How-Do-Wind-Turbines-Work.</div>

[6] C. Steiness, “Horns Rev Vattenfall.”

[7] Enel, “Wind Farm.” Accessed: Oct. 09, 2024. [Online]. Available: https://www.enelgreenpower.com/learning-hub/renewable-energies/wind-energy/wind-farm

[8] “North Hoyle Wind Farm”.

[9] Alberta, “Alberta and Modern Wind Power.” Accessed: Oct. 10, 2024. [Online]. Available: http://www.history.alberta.ca/energyheritage/energy/wind-power/alberta-and-modern-wind-power.aspx#:~:text=As%20of%202013%2C%20the%20largest,generating%201.8%20MW%20of%20power

[10] “Non-technical-summary”.

[11] “Horns Rev Offshore Wind Farm Environmental Impact Assessment: Summary of EIA Report,” 2000. [Online]. Available: www.elsam.com

[12] edf, “Wesley-Ciskei Wind Farm.” Accessed: Oct. 10, 2024. [Online]. Available: https://edf-re.co.za/operational/wesley-ciskei/

[13] G. Plaven, "Wind energy keeps turning in rural Oregon." Accessed: Oct. 10, 2024. [Online]. Available: https://www.theotheroregon.com/cover_story/wind-energy-keeps-turning-in-rural-oregon/article_32c4ff1a-a623-11ec-b27b-8f384d70c6a0.html

[14] K. W. Van Treuren and T. A. Burdett, "Experimental Testing of Wind Turbines Using Wind Tunnels With an Emphasis on Small-Scale Wind Turbines Under Low Reynolds Numbers," 2014, pp. 67–110. doi: 10.2495/978-1-78466-004-8/004.

[15] M. Piano *et al.*, "Tidal stream resource assessment uncertainty due to flow asymmetry and turbine yaw misalignment," *Renew Energy*, vol. 114, pp. 1363–1375, 2017, doi: 10.1016/j.renene.2017.05.023.

[16] X. Zhao *et al.*, "Experimental study on the characteristics of wind turbine wake field considering yaw conditions," *Energy Sci Eng*, vol. 9, no. 12, pp. 2333–2341, Dec. 2021, doi: 10.1002/ese3.987.

[17] C. Cossu, "Evaluation of tilt control for wind-turbine arrays in the atmospheric boundary layer," *Wind Energy Science*, vol. 6, no. 3, pp. 663–675, May 2021, doi: 10.5194/wes-6-663-2021.

[18] J. Annoni, A. Scholbrock, M. Churchfield, and P. Fleming, "Evaluating Tilt for Wind Farms Preprint Evaluating Tilt for Wind Plants." [Online]. Available: http:/www.osti.gov/scitech

[19] J. Bartl *et al.*, "Wind tunnel experiments on wind turbine wakes in yaw: Effects of inflow turbulence and shear," *Wind Energy Science*, vol. 3, no. 1, pp. 329–343, Jan. 2018, doi: 10.5194/wes-3-329-2018.

[20] R. Scott, "Characterizing Tilt Effects on Wind Plants," Portland, OR, Jan. 2000. doi: 10.15760/etd.6911.

[21] F. Trigaux, M. Moens, P. Chatelain, and G. Winckelmans, "Tilted wind turbines in farm configuration for improved global efficiency," in *Journal of Physics: Conference Series*, IOP Publishing Ltd, Sep. 2020. doi: 10.1088/1742-6596/1618/6/062035.

[22] J. Cutler, A. P. J. Stanley, J. J. Thomas, and A. Ning, "Optimization of turbine tilt in a wind farm," in *AIAA Scitech 2021 Forum*, American Institute of Aeronautics and Astronautics Inc, AIAA, 2021, pp. 1–10. doi: 10.2514/6.2021-1180.

[23] C. L. Archer and A. Vasel-Be-Hagh, "Wake steering via yaw control in multi-turbine wind farms: Recommendations based on large-eddy simulation," *Sustainable Energy Technologies and Assessments*, vol. 33, pp. 34–43, Jun. 2019, doi: 10.1016/j.seta.2019.03.002.

[24] J. Bartl *et al.*, “Wind tunnel experiments on wind turbine wakes in yaw: Effects of inflow turbulence and shear,” *Wind Energy Science*, vol. 3, no. 1, pp. 329–343, Jan. 2018, doi: 10.5194/wes-3-329-2018.

[25] J. Schottler, J. Bartl, F. Mühle, L. Sætran, J. Peinke, and M. Hölling, “Wind tunnel experiments on wind turbine wakes in yaw: Redefining the wake width,” *Wind Energy Science*, vol. 3, no. 1, pp. 257–273, Jan. 2018, doi: 10.5194/wes-3-257-2018.

[26] F. Campagnolo, V. Petrović, C. L. Bottasso, and A. Croce, “Wind tunnel testing of wake control strategies,” in *Proceedings of the American Control Conference*, Institute of Electrical and Electronics Engineers Inc., Jul. 2016, pp. 513–518. doi: 10.1109/ACC.2016.7524965.

[27] J. Bossuyt, R. Scott, N. Ali, and R. B. Cal, “Quantification of wake shape modulation and deflection for tilt and yaw misaligned wind turbines,” *J Fluid Mech*, vol. 917, 2021, doi: 10.1017/jfm.2021.237.

[28] J. Bartl, F. Mühle, and L. Sætran, “Wind tunnel study on power output and yaw moments for two yaw-controlled model wind turbines,” *Wind Energy Science*, vol. 3, no. 2, pp. 489–502, 2018, doi: 10.5194/wes-3-489-2018.

[29] M. F. Howland, S. K. Lele, and J. O. Dabiri, “Wind farm power optimization through wake steering,” *Proc Natl Acad Sci U S A*, vol. 116, no. 29, pp. 14495–14500, 2019, doi: 10.1073/pnas.1903680116.

[30] N. Bempedelis, S. Laizet, and G. Deskos, “Turbulent entrainment in finite-length wind farms,” *J Fluid Mech*, vol. 955, Jan. 2023, doi: 10.1017/jfm.2022.1064.

[31] M. Bastankhah and F. Porté-Agel, “Experimental and theoretical study of wind turbine wakes in yawed conditions,” *J Fluid Mech*, vol. 806, pp. 506–541, Nov. 2016, doi: 10.1017/jfm.2016.595.

[32] Mathworks, “Reduced Order Modelling.” Accessed: Nov. 05, 2024. [Online]. Available: https://www.mathworks.com/discovery/reduced-order-modeling.html

[33] B. Kulp, “What is a Reduced Order Model and What’s Its Product Development Role?” Accessed: Nov. 05, 2024. [Online]. Available: https://www.ansys.com/blog/what-is-a-reduced-order-model-response-surface-model

[34] N. Rodrigues Cassamo, J.-W. van Wingerden João Miguel da Costa Sousa, C. Frederico Neves Bettencourt da Silva Supervisor, J.-W. van Wingerden, and M. Afonso Dias de Ayala Botto Paulo Jorge Coelho Ramalho Oliveira, “Model Predictive Control for Wake Steering: a

Koopman Dynamic Mode Decomposition Approach Mechanical Engineering Examination Committee," 2020.

[35] J. Zhang and X. Zhao, "Machine-learning-based surrogate modeling of aerodynamic flow around distributed structures," *AIAA Journal*, vol. 59, no. 3, pp. 868–879, 2021, doi: 10.2514/1.J059877.

[36] Z. Ti, X. W. Deng, and M. Zhang, "Artificial Neural Networks based wake model for power prediction of wind farm," *Renew Energy*, vol. 172, pp. 618–631, Jul. 2021, doi: 10.1016/j.renene.2021.03.030.

[37] J. Zhang and X. Zhao, "Wind farm wake modeling based on deep convolutional conditional generative adversarial network," *Energy*, vol. 238, Jan. 2022, doi: 10.1016/j.energy.2021.121747.

[38] J. Zhang and X. Zhao, "A novel dynamic wind farm wake model based on deep learning," *Appl Energy*, vol. 277, Nov. 2020, doi: 10.1016/j.apenergy.2020.115552.

[39] S. Purohit, E. Y. K. Ng, and I. F. Syed Ahmed Kabir, "Evaluation of three potential machine learning algorithms for predicting the velocity and turbulence intensity of a wind turbine wake," *Renew Energy*, vol. 184, pp. 405–420, Jan. 2022, doi: 10.1016/j.renene.2021.11.097.

[40] C. ; Bak *et al.*, "General rights The DTU 10-MW Reference Wind Turbine). The DTU 10-MW Reference Wind Turbine. Sound/Visual production (digital)," 2013.

[41] N. Rodrigues Cassamo, J.-W. van Wingerden João Miguel da Costa Sousa, C. Frederico Neves Bettencourt da Silva Supervisor, J.-W. van Wingerden, and M. Afonso Dias de Ayala Botto Paulo Jorge Coelho Ramalho Oliveira, "Model Predictive Control for Wake Steering: a Koopman Dynamic Mode Decomposition Approach Mechanical Engineering Examination Committee," 2020.

[42] M. Bastankhah and F. Porté-Agel, "A new miniaturewind turbine for wind tunnel experiments. Part I: Design and performance," *Energies (Basel)*, vol. 10, no. 7, 2017, doi: 10.3390/en10070908.

[43] A. Eltayesh *et al.*, "Effect of wind tunnel blockage on the performance of a horizontal axis wind turbine with different blade number," *Energies (Basel)*, vol. 12, no. 10, 2019, doi: 10.3390/en12101988.

[44] A. S. M. Al-Obaidi and G. Madivaanan, "Investigation of the Blockage Correction to Improve the Accuracy of Taylor's Low-Speed Wind Tunnel," in *Journal of Physics: Conference Series*, Institute of Physics, 2022. doi: 10.1088/1742-6596/2222/1/012008.

[45] A. S. Dar, R. Majzoub, and F. Porté-Agel, “The effect of nacelle-to-rotor size on the wake of a miniature wind turbine,” in *Journal of Physics: Conference Series*, Institute of Physics, 2024. doi: 10.1088/1742-6596/2767/9/092057.

[46] PrototypeLabs, “3D printing with PLA vs. ABS: What’s the difference?,” 2024, Accessed: Oct. 10, 2024. [Online]. Available: https://www.hubs.com/knowledge-base/pla-vs-abs-whats-difference/

[47] Wevolver, “PLA Smoothing: How to Smooth 3D Prints.” Accessed: Oct. 10, 2024. [Online]. Available: https://www.wevolver.com/article/pla-smoothing

[48] Xometry, “Vapor Smoothing: An Effective Surface Finish Process in 3D Printing,” Jul. 2023, Accessed: Oct. 10, 2024. [Online]. Available: https://xometry.pro/en-eu/articles/3d-printing-vapor-smoothing/

[49] J. Whale, C. G. Anderson, R. Bareiss, and S. Wagner, “An experimental and numerical study of the vortex structure in the wake of a wind turbine,” 2000.

[50] J. Wang *et al.*, “Numerical and Experimental Study of Wake Redirection Techniques in a Boundary Layer Wind Tunnel,” in *Journal of Physics: Conference Series*, Institute of Physics Publishing, Jun. 2017. doi: 10.1088/1742-6596/854/1/012048.

[51] “ACES Systems Guide to Propeller Balancing Aviation Division FAA Approval,” 1996.

[52] A. Raeesi, S. McTavish, and A. D’Auteuil, “Aerodynamic characteristics of generic ice shells,” *Journal of Wind Engineering and Industrial Aerodynamics*, vol. 184, pp. 49–60, Jan. 2019, doi: 10.1016/j.jweia.2018.11.002.

[53] “Yaw system”, Accessed: Oct. 10, 2024. [Online]. Available: https://en.wikipedia.org/wiki/Yaw_system

[54] M. F. Howland, J. Bossuyt, L. A. Martínez-Tossas, J. Meyers, and C. Meneveau, “Wake Structure of Wind Turbines in Yaw under Uniform Inflow Conditions,” 2016.

[55] Safex, “SAFEX®-Inside fog fluid ‘Normal/Power Mix.’” Accessed: Oct. 10, 2024. [Online]. Available: https://safex.shop/de/safex-inside-nebelfluid-normal-power-mix.html

[56] BorisFx, “GoPro vs DSLR: Which One is Better for You?” Accessed: Oct. 10, 2024. [Online]. Available: https://crumplepop.com/gopro-vs-dslr-which-one-is-better-for-you/

[57] Canon, “Understanding focal length in photography.” Accessed: Oct. 10, 2024. [Online]. Available: https://www.canon-europe.com/pro/infobank/understanding-focal-length/

[58] GrabCAD, “GoPro Hero 10 Black.” Accessed: Oct. 10, 2024. [Online]. Available: https://grabcad.com/library/gopro-hero-10-black-1

[59] A. L. Y. J. F. F. Cameron Tropea, *Springer handbook of experimental fluid mechanics*. Berlin: Springer, 2007.

[60] H. Zong and F. Porté-Agel, “Experimental investigation and analytical modelling of active yaw control for wind farm power optimization,” *Renew Energy*, vol. 170, pp. 1228–1244, Jun. 2021, doi: 10.1016/j.renene.2021.02.059.

[61] K. B. Lua, T. T. Lim, and K. S. Yeo, “Aerodynamic forces and flow fields of a two-dimensional hovering wing,” *Exp Fluids*, vol. 45, no. 6, pp. 1047–1065, Dec. 2008, doi: 10.1007/s00348-008-0527-z.

[62] K. Taira *et al.*, “Modal analysis of fluid flows: An overview,” *AIAA Journal*, vol. 55, no. 12, pp. 4013–4041, 2017, doi: 10.2514/1.J056060.

[63] Z. Wu, D. Laurence, S. Utyuzhnikov, and I. Afgan, “Proper orthogonal decomposition and dynamic mode decomposition of jet in channel crossflow,” *Nuclear Engineering and Design*, vol. 344, pp. 54–68, Apr. 2019, doi: 10.1016/j.nucengdes.2019.01.015.

[64] G. De Cillis, S. Cherubini, O. Semeraro, S. Leonardi, and P. De Palma, “POD analysis of the recovery process in wind turbine wakes,” in *Journal of Physics: Conference Series*, IOP Publishing Ltd, Sep. 2020. doi: 10.1088/1742-6596/1618/6/062016.

[65] IBM, “What is supervised learning?” Accessed: Oct. 10, 2024. [Online]. Available: https://www.ibm.com/topics/supervised-learning

[66] IBM, “What is the k-nearest neighbors (KNN) algorithm?” Accessed: Oct. 10, 2024. [Online]. Available: https://www.ibm.com/topics/knn#:~:text=The%20k%2Dnearest%20neighbors%20(KNN,of%20an%20individual%20data%20point.

[67] Brilliant, “K-nearest Neighbors”, Accessed: Oct. 10, 2024. [Online]. Available: https://brilliant.org/wiki/k-nearest-neighbors/

[68] J. Holdsworth and M. Scapicchio, “What is deep learning?” Accessed: Oct. 10, 2024. [Online]. Available: https://www.ibm.com/topics/deep-learning

[69] Amzhao, “Quantum Neural Networks.” Accessed: Oct. 10, 2024. [Online]. Available: https://medium.com/mit-6-s089-intro-to-quantum-computing/quantum-neural-networks-7b5bc469d984

[70] M. Memon, “ANN vs CNN vs RNN: Neural Networks Guide.” Accessed: Oct. 10, 2024. [Online]. Available: https://levity.ai/blog/neural-networks-cnn-ann-rnn#:~:text=ANNs%20(Artificial%20Neural%20Networks)%20are,proficient%20in%20Natural%20Language%20Processing

[71] M. Uzair and N. Jamil, “Effects of Hidden Layers on the Efficiency of Neural networks,” in *Proceedings - 2020 23rd IEEE International Multi-Topic Conference, INMIC 2020*, Institute of Electrical and Electronics Engineers Inc., Nov. 2020. doi: 10.1109/INMIC50486.2020.9318195.

[72] Z. Ti, X. W. Deng, and M. Zhang, “Artificial Neural Networks based wake model for power prediction of wind farm,” *Renew Energy*, vol. 172, pp. 618–631, Jul. 2021, doi: 10.1016/j.renene.2021.03.030.

[73] Mathworks, “Neural Net Fitting.” Accessed: Oct. 10, 2024. [Online]. Available: https://www.mathworks.com/help/deeplearning/ref/neuralnetfitting-app.html

[74] G. A. Hamill and C. Kee, “Predicting axial velocity profiles within a diffusing marine propeller jet,” *Ocean Engineering*, vol. 124, pp. 104–112, Sep. 2016, doi: 10.1016/j.oceaneng.2016.07.061.

[75] A. Stuermer and M. Rakowitz, “Unsteady Simulation of a Transport Aircraft Propeller Using MEGAFLOW,” 2005. [Online]. Available: http://www.rto.nato.int/abstracts.aps.

[76] Z. Sadek, R. Scott, N. Hamilton, and R. B. Cal, “A three-dimensional, analytical wind turbine wake model: Flow acceleration, empirical correlations, and continuity,” *Renew Energy*, vol. 209, pp. 298–309, Jun. 2023, doi: 10.1016/j.renene.2023.03.129.

[77] P. A. Fleming *et al.*, “Evaluating techniques for redirecting turbine wakes using SOWFA,” *Renew Energy*, vol. 70, pp. 211–218, 2014, doi: 10.1016/j.renene.2014.02.015.

[78] M. Bastankhah and F. Porté-Agel, “A new miniaturewind turbine for wind tunnel experiments. Part II: Wake structure and flow dynamics,” *Energies (Basel)*, vol. 10, no. 7, 2017, doi: 10.3390/en10070923.

[79] Á. Jiménez, A. Crespo, and E. Migoya, “Application of a LES technique to characterize the wake deflection of a wind turbine in yaw,” *Wind Energy*, vol. 13, no. 6, pp. 559–572, Sep. 2010, doi: 10.1002/we.380.

[80] Y. Yang, L. L. M. Veldhuis, and G. Eitelberg, “Numerical analysis of propeller induced ground vortices by actuator disk model,” *J Vis (Tokyo)*, vol. 21, no. 1, pp. 117–132, Feb. 2018, doi: 10.1007/s12650-017-0444-4.

[81] N. Sedaghatizadeh, M. Arjomandi, R. Kelso, B. Cazzolato, and M. H. Ghayesh, “The effect of the boundary layer on the wake of a horizontal axis wind turbine,” *Energy*, vol. 182, pp. 1202–1221, Sep. 2019, doi: 10.1016/j.energy.2019.06.066.

[82] Z. Fei *et al.*, “Experimental study on wake interactions and performance of the turbines with different rotor-diameters in adjacent area of large-scale wind farm,” *Energy*, vol. 199, May 2020, doi: 10.1016/j.energy.2020.117416.

9 APPENDICES

9.1 Data Sheets

9.1.1 DC motor

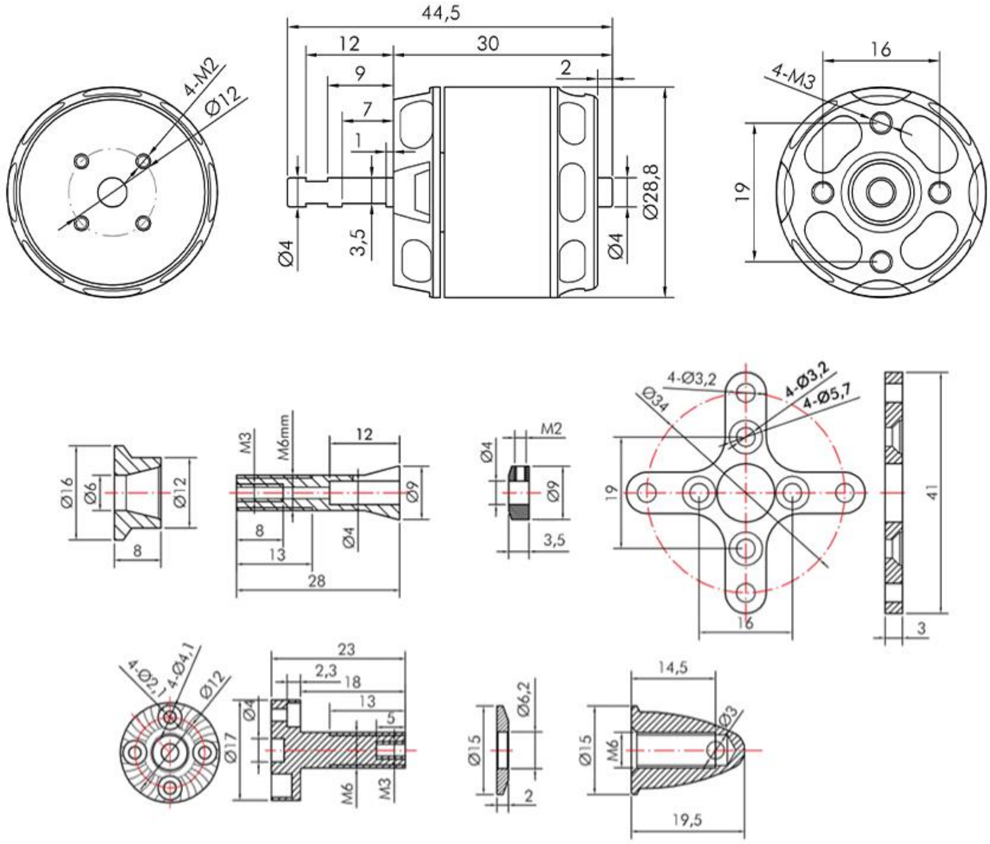

Specification			
Test Item	Long Shaft KV1150	Weight (Incl. Cable)	60g
Motor Dimensions	Φ28.4*44.5mm	Internal Resistance	75mΩ
Lead	22#AWG 100mm	Configuration	12N14P
Shaft Diameter	IN：4mm OUT：4mm	Rated Voltage(Lipo)	2-4S
Idle Current(10V)	0.85A	Peak Current(180s)	25A
Max. Power(180s)	350W	Recommendation	/
Test Item	Long Shaft KV1400	Weight (Incl. Cable)	60g
Motor Dimensions	Φ28.4*44.5mm	Internal Resistance	55mΩ
Lead	22#AWG 100mm	Configuration	12N14P
Shaft Diameter	IN：4mm OUT：4mm	Rated Voltage(Lipo)	2-4S
Idle Current(10V)	1.1A	Peak Current(180s)	30A
Max. Power(180s)	320W	Recommendation	/

9.1.3 Smoke Fluid

Safety Data Sheet

according ordinance (EG) No. 1907/2006

GÜNTHER SCHAIDT SAFEX®-CHEMIE GMBH-SCHENEFELD

Trade name : **SAFEX-INSIDE NEBELFLUID - all variations**

Revision date : 03.11.11 **Version :** 1.01

Print date:

---

01. Identification of the substance/mixture and of the company/undertaking

Trade name

SAFEX-INSIDE NEBELFLUID - all variations -

Designation of the mixture

Generating artificial fog for Theater-, TV- and Motion Picture- and Show-productions, as well as for technical and scientific applications with SAFEX®-FOG-GENERATORS.

Manufacturer

GÜNTHER SCHAIDT SAFEX®-CHEMIE GMBH

---

02. Hazards identification

Hazard designation:

This mixture is **not classified as hazardous** according to 1999/45/EC.

Additional hazard notes for man and environment:

The vaporized product bears **no** health hazards or other deleterious substance-effects; however, an overdosed fog poses the risk to cover danger spots in the surroundings (risk of falling, bumping, stumble possible). There is also the possibility of a on smooth surfaces* when the fog is over-dosed or if the none-vaporized product is spilled. (*Smooth plastic-, marble-, metallic surfaces, etc.)

Sensitive people can react to artificial fog with fright and fear and may develop psychosomatic reactions. Also asthmatics can react with fright and consequently with a substance independent asthmatic reaction.

A strong overdosed fog outdoors can create a traffic hazard.

---

03. Composition / information on ingredients

Chemical characterization

Aqueous solution of non-toxic, highly pure polyols.

Hazardous ingredients

Non, not even < 1%

Ratio: 0%

Classification : No classification and labeling required for the products.

Seite : 1 / 10

9.1.3 Strain Gauges

Gages for Composite Materials & Plastics KFRP

Patterns, Gage Resistance, Gage Factor	Models	Dimensions (mm) Grid Length	Grid Width	Base Length	Base Width	Remarks

●KFRP Series Foil Strain Gages for Composite Materials

When ordering, suffix the lead wire cable code (See table at the right) to the model number with a space in between.

E.g.
KFRP-5-120-C1-1 N15C2
for the gage with polyester-coated 2-wire copper cable 15 cm long
KFRP-5-120-D22-3 L5M3S
for the gage with a vinyl-coated flat 3-wire cable 5 m long pre-attached
If no lead wire cable code is suffixed, the gage is delivered with gage leads only (Silver-clad copper wires 25 mm long)

The KFRP series foil strain gages are self-temperature-compensation gages (SELCOM® gages) suitable for strain measurement of composite materials such as CFRP and GFRP. The special gage pattern minimizes the effect of self-heating due to gage current and the effect of reinforcement of low-elasticity materials.
To ensure accurate measurement by avoiding the self-heating effect of gage current, consider the following:

1. Select a lower bridge excitation voltage if the amplifier allows bridge voltage selection.
2. Active-dummy system
3. 350Ω strain gages

Applicable Adhesives and Operating Temperature Range after Curing

CC-33A: -196 to 120°C　CC-35: -30 to 120°C
CC-36: -30 to 100°C　EP-34B: -55 to 200°C

■Types, lengths and codes of lead wire cables pre-attached to KFRP gages

Types / Length	2polyester-coated copper wires	3polyester-coated copper wires	Vinyl-coated flat 2-wire cable		Vinyl-coated flat 3-wire cable		Middle-temperature 2-wire cable	Middle-temperature 3-wire cable	Fluoroplastic coated high/low-temp. 3-wire cable
	C1, D22		C1	D22	C1	D22	C1, D22		
15 cm	N15C2	N15C3	L15C2R	L15C2S	L15C3R	L15C3S	R15C2	R15C3	F15C3
30 cm	N30C2	N30C3	L30C2R	L30C2S	L30C3R	L30C3S	R30C2	R30C3	F30C3
1 m	N1M2	N1M3	L1M2R	L1M2S	L1M3R	L1M3S	R1M2	R1M3	F1M3
3 m			L3M2R	L3M2S	L3M3R	L3M3S	R3M2	R3M3	F3M3
5 m			L5M2R	L5M2S	L5M3R	L5M3S	R5M2	R5M3	F5M3
Oprg. temp. range	-196 to 150°C		-10 to 80°C				-100 to 150°C		-196 to 200°C
Remarks	Twisted for 50 cm or longer		L-6, L-9 for 6 m or longer		L-7, L-10 for 6 m or longer		L-11	L-12	L-3

＊For other lead wire cable lengths, contact us.

Patterns, Gage Resistance, Gage Factor	Models	Grid Length	Grid Width	Base Length	Base Width	Remarks
Uniaxial Resistance: 120 Ω Gage factor: Approx. 2.1 	KFRP-5-120-C1-1 KFRP-5-120-C1-3 KFRP-5-120-C1-6 KFRP-5-120-C1-9	5	1.4	15	5	
	KFRP-2-120-C1-1 KFRP-2-120-C1-3 KFRP-2-120-C1-6 KFRP-2-120-C1-9	2	1.2	10	5	
Uniaxial Resistance: 350 Ω Gage factor: Approx. 2.1 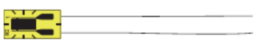	KFRP-5-350-C1-1 KFRP-5-350-C1-3 KFRP-5-350-C1-6 KFRP-5-350-C1-9	5	1.5	15	5	
	KFRP-2-350-C1-1 KFRP-2-350-C1-3 KFRP-2-350-C1-6 KFRP-2-350-C1-9	2	2.2	10	5	
Triaxial, 0°/90°/45° Resistance: 120 Ω Gage factor: Approx. 2.1 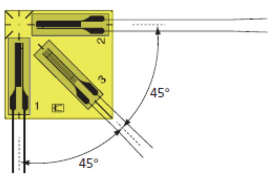	Each of 3 axis may be given a different linear expansion coefficient if requested. KFRP-5-120-D22-1 KFRP-5-120-D22-3 KFRP-5-120-D22-6 KFRP-5-120-D22-9	5	1.4	19	19	
	KFRP-2-120-D22-1 KFRP-2-120-D22-3 KFRP-2-120-D22-6 KFRP-2-120-D22-9	2	1.2	15	15	

A min. qty 10 PC.

9.2 CAD Drawings of Manufactured Components

9.2.1 Rotor

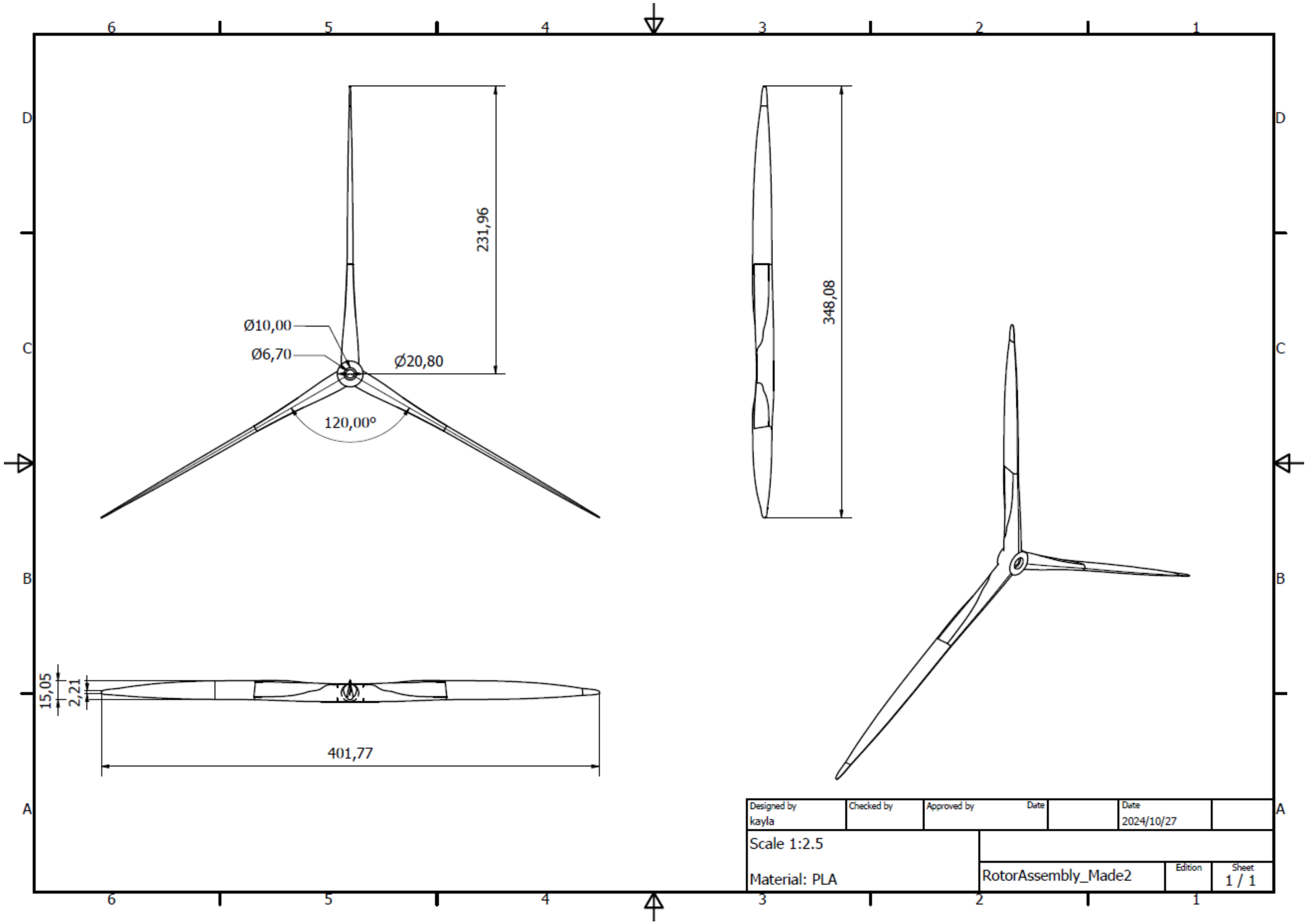

9.2.2 Tower

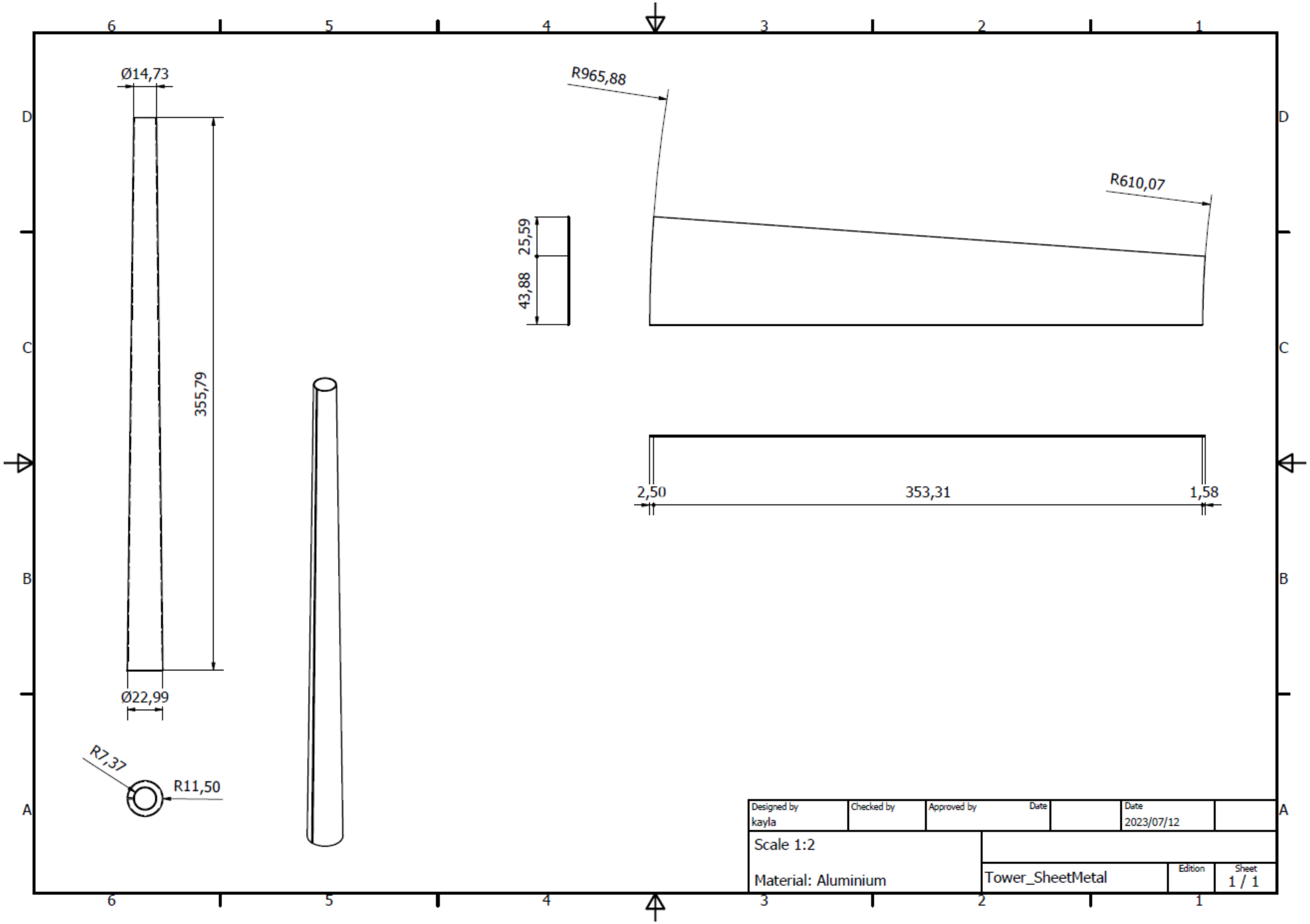

Ø14,73
355,79
Ø22,99
R7,37
R11,50
R965,88
R610,07
25,59
43,88
2,50
353,31
1,58
Designed by
kayla
Checked by
Approved by
Date
Date
2023/07/12
Scale 1:2
Material: Aluminium
Tower_SheetMetal
Edition
Sheet
1 / 1

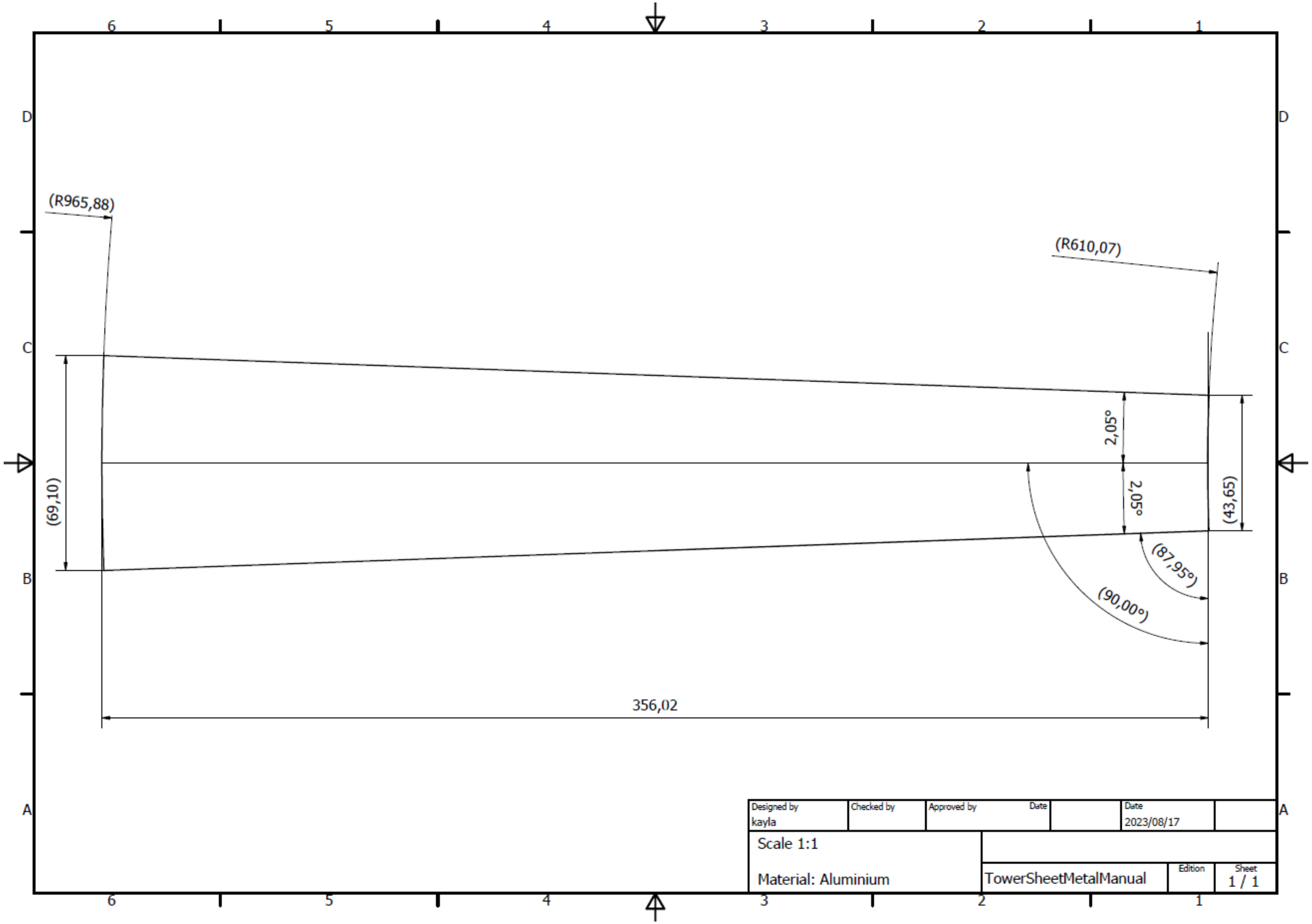

Designed by	Checked by	Approved by	Date	Date	
kayla				2023/08/17	

Scale 1:1

Material: Aluminium

TowerSheetMetalManual	Edition	Sheet
		1 / 1

9.2.3 Nacelle

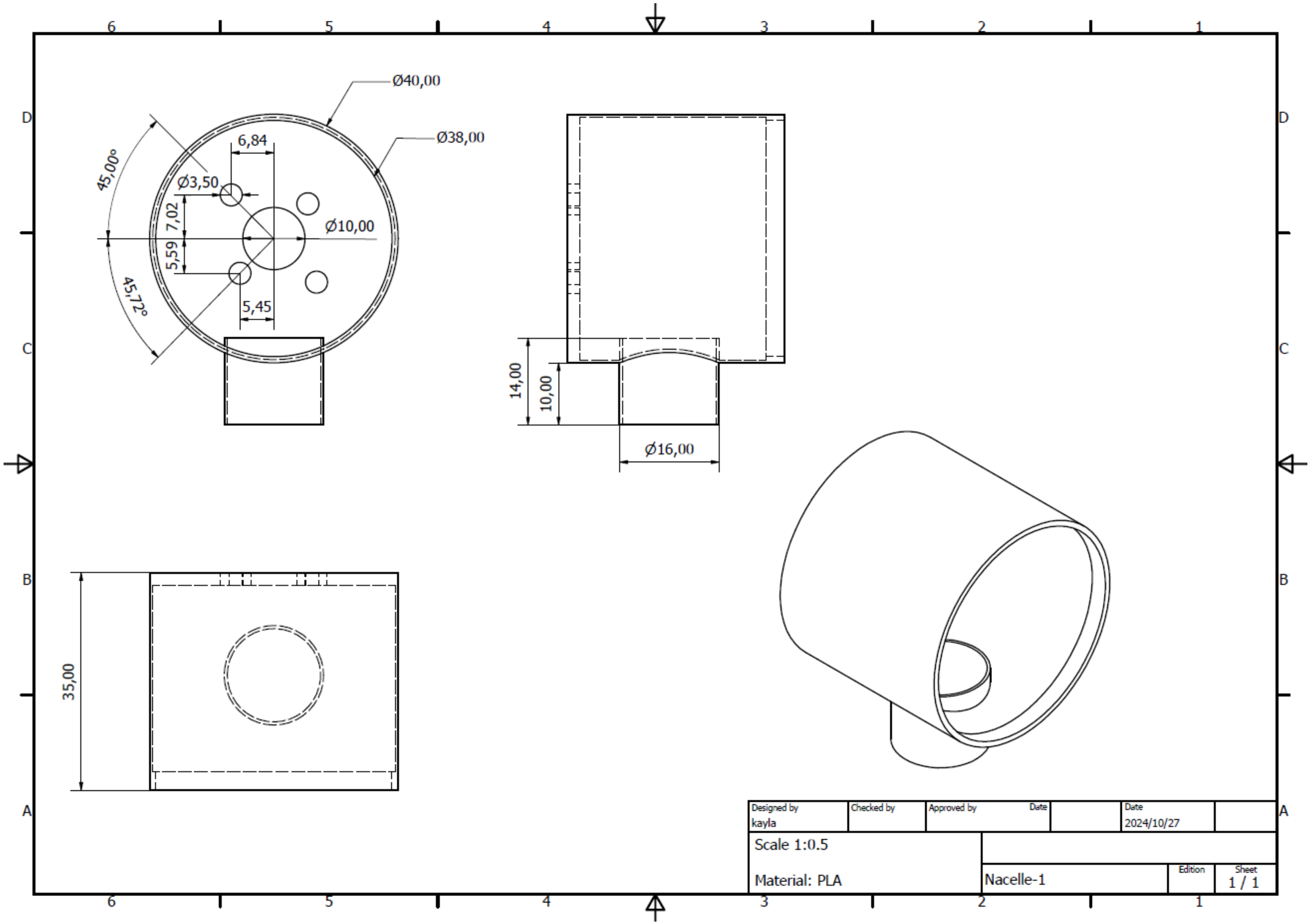

Ø40,00
Ø38,00
6,84
Ø3,50
45,00°
7,02
5,59
Ø10,00
45,72°
5,45
14,00
10,00
Ø16,00
35,00
Designed by
kayla
Checked by
Approved by
Date
Date
2024/10/27
Scale 1:0.5
Material: PLA
Nacelle-1
Edition
Sheet
1 / 1

9.2.4 Hub

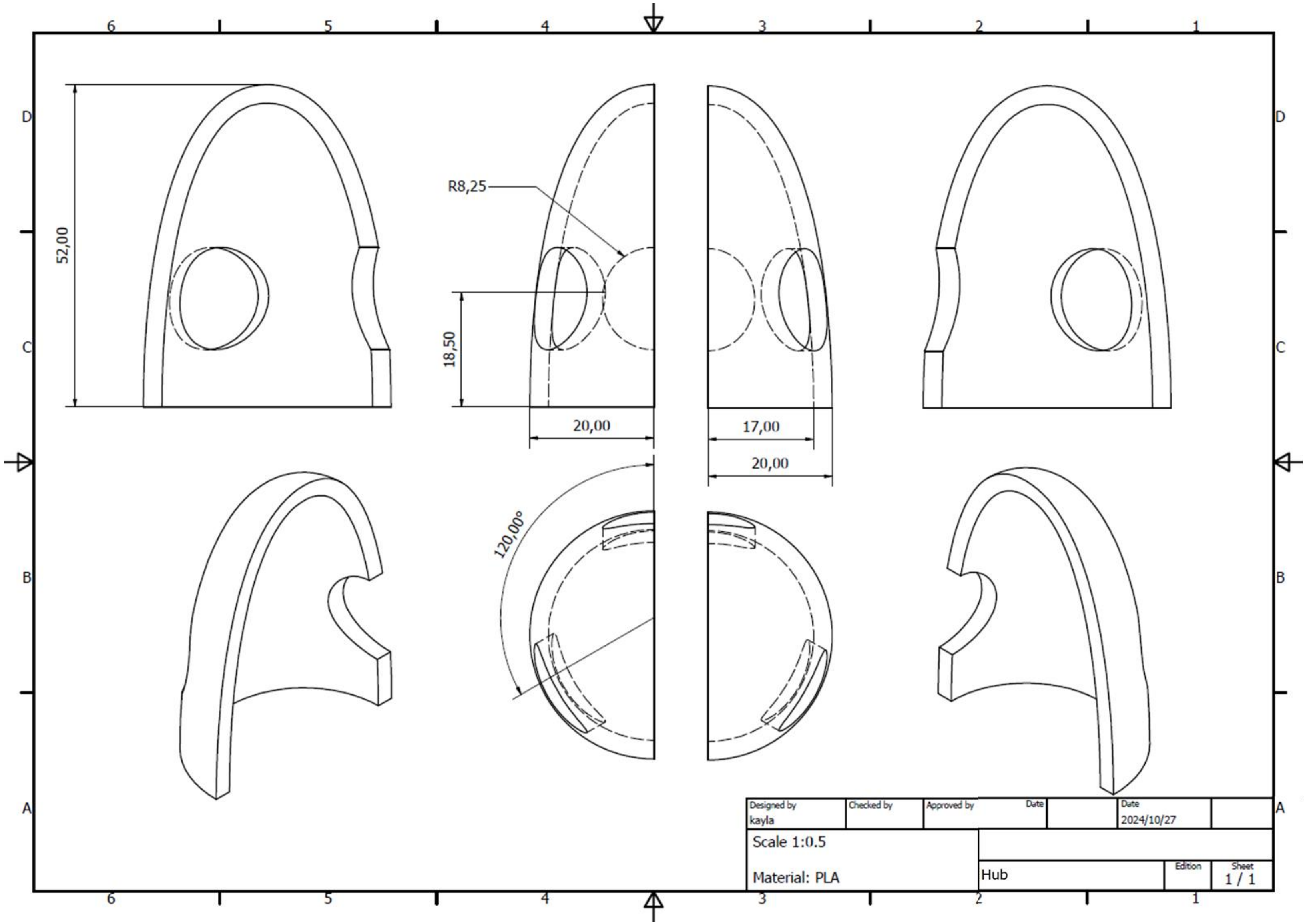

52,00
R8,25
18,50
20,00
17,00
20,00
120,00°
Designed by
kayla
Checked by
Approved by
Date
Date
2024/10/27
Scale 1:0.5
Material: PLA
Hub
Edition
Sheet
1 / 1

9.2.5 Camera Mount